eXPRESS Polymer Letters Vol.5, No.7 (2011) 569
Available online at www.expresspolymlett.com
DOI: 10.3144/expresspolymlett.2011.55

Editorial corner – a personal view
Rice husk: Turning wastes into wealth

*Z. A. Mohd Ishak**

School of Materials and Mineral Resources Engineering, Engineering Campus, Universiti Sains Malaysia, 14300 Penang, Malaysia

In recent years, due to growing environmental awareness, agro-fillers have been increasingly used as fillers in polymer composites. In general, these organic fillers promise some advantages compared to traditional inorganic fillers, including their renewable nature, low density, nonabrasive properties and reasonable strength and stiffness. This makes them competitive as reinforcement in certain composite applications. One of the potential agro-filler for polymer composites is rice husk (RH). Every year about 50–100 million tons of husk residues were produced from world rice production. The disposal of RH wastes poses a growing problem due to the low bulk-density nature of the husks. Thus the utilization of RH as filler in polymer composite applications is alternative to alleviate problems related to the disposal of the waste husks. The composition of RH is 35% cellulose, 25% hemicellulose, 20% lignin and 17% ash (mainly 94% silica, SiO_2) by weight.

The presence of SiO_2 provides at least two main advantages to RH i.e. processability and durability. RH has higher degradation and decomposition temperature (≈250ºC) compared with wood flour (≈200ºC) due to it relatively low lignin and hemicellulose contents. Therefore, the processing of RH composites can be performed up to 250ºC. The use of 'natural composites' is often questioned for outdoor application. The durability study of composites can be classified into 3 main categories i.e. weathering, moisture absorption and biodegradation. As far as moisture absorption is concerned RH should behave better than wood composites due to its SiO_2 content. The high hydroxyl group content of cellulose is the main cause of poor compatibility between hydrophilic natural fillers and hydrophobic polymers used as the matrix. The most effective and economical way to improve the fiber-matrix interfacial adhesion of RH filled polymer composites is by adding a compatibiliser/coupling agent.

In responding to the needs of developing environmentally friendly composites, considerable efforts are being undertaken to produce RH composites based on biodegradable polymer matrices such as poly(lactic acid), poly butylene succinate (PBS), etc. It would be interesting to investigate how the presence of SiO_2 in RH would affect the durability in general and the biodegradability in particular, of those polymers.

Although RH composites are finding wider acceptance to be used in various applications, researches are still ongoing to improve the overall performances of the composites. Issues such as lack of established delivery channels i.e. transportation of RH from various rice mills to the RH processing plant, processing complications due to the low density and hygroscopicity of RH are limiting the wider scope of application of RH. The development of new polymer additives and processing technology must be intensified in order produce high quality RH composite products.

Prof. Dr. Zainal Arifin Mohd Ishak
Member of International Advisory Board

*Corresponding author, e-mail: zarifin.ishak@googlemail.com

eXPRESS Polymer Letters Vol.5, No.7 (2011) 570–580
Available online at www.expresspolymlett.com
DOI: 10.3144/expresspolymlett.2011.56

Phase diagrams in blends of poly(3-hydroxybutyric acid) with various aliphatic polyesters

*Y. T. Hsieh, E. M. Woo**

Department of Chemical Engineering National Cheng Kung University Tainan, 701, Taiwan

Received 20 October 2010; accepted in revised form 6 January 2011

Abstract. Phase behavior with immiscibility, miscibility, crystalline morphology, and kinetic analysis in blends of poly(3-hydroxybutyric acid) (PHB) with aliphatic polyesters such as poly(butylene adipate) (PBA), poly(ethylene adipate) (PEA), poly(trimethylene adipate) (PTA), or poly(ethylene succinate) (PESu), respectively, were explored mainly using differential scanning calorimeter (DSC) and polarized-light optical microscopy (POM). Immiscibility phase behavior with reversible upper-critical-solution-temperature (UCST) is common in the PHB/polyester blends. The polyester/polyester blend of PHB/PTA is partially miscible with no UCST in melt and amorphous glassy states within a composition range of PTA less than 50 wt%. The miscible crystalline/crystalline blend exhibits ring-banded spherulites at T_c = 50~100°C, with inter-ring spacing dependent on T_c. All immiscible or partially miscible PHB/polyester blends, by contrast, exhibit disrupted ring-banded spherulites or discrete spherical phase domains upon cooling from UCST to crystallization. The blends of PHB with all other aliphatic polyesters, such as PESu, PEA, PBA, etc. are only partially miscible or immiscible with an upper critical solution temperature (UCST) at 180~221°C depending on blend composition. UCST with reversibility was verified.

Keywords: *biodegradable polymers, PHB, miscibility, aliphatic polyesters*

1. Introduction

Blending of biodegradable poly(3-hydroxybutyric acid) (PHB) or poly(L-lactic acid) (PLLA) with other aliphatic polyesters is one of common approaches to modify the properties of the biodegradable polyesters for various end uses. Blending of PHB or PLLA with other polyesters mostly leads to immiscible mixtures, owing to the fact that the interaction between the biodegradable polyester and other aliphatic polyesters is generally weak or insufficient for leading to a homogeneous mixture at ambient temperatures [1–3]. For example, the blend of poly(ethylene succinate) (PESu) with PLLA was claimed to be immiscible [1]. However, in a later study, it was found that the blend of PESu/PLLA exhibited an upper critical solution temperature (UCST) phase boundary at ~230–250°C [2]. In addition, Kumagai and Doi [3] reported that PHB was immiscible with poly(ethylene adipate) (PEA) (M_w = 11 000 g/mol), since the T_g of PEA was independent of the polymer composition after melt-quenched from 200 to –100°C. However, it must be noted that the phase behavior of the PHB/PEA blend (blend of two polyesters) might be temperature-dependent; i.e., phase transition from immiscibility to miscibility at UCST above 200°C could not be ruled out without further investigations. Similarly, the phase behavior of PHB/PEA (or PHB/PESu) could be temperature-dependent, which means that phase behavior of these blends might undergo changes upon heating to some higher temperatures. In addition, the phase behavior in polyester blends may be M_w-dependent as well as temperature dependent. This means that if M_w of either

*Corresponding author, e-mail: emwoo@mail.ncku.edu.tw

of two components is lowered or temperature is changed, the blends of two polyesters may undergo phase transformation with respect to temperature.

PLLA or PHB blends with other polyesters might be phase-separated systems at ambient temperature, but actually they may turn into one-phase domain when kept at above a certain temperature range (UCST) or they may become miscible if the molecular weights of either or both components are lowered. Attempts have also been made to blend PHB with PLLA [4–5], however, only partial miscibility in the PLLA/PHB blend was resulted. Preliminary results also indicated that as the molecular weight of PLLA is lowered, PHB/PLLA may become miscible [4, 6]. Phase behavior in polymer blends can be temperature dependent, as revealed in common UCST or lower critical solution temperature (LCST). UCST is normally seen in blends of polymers possessing similar chemical structures or functional groups. Polymer blends that are thermodynamically immiscible at lower temperatures but turn miscible at elevated temperatures (UCST) have been known in some well-studied classical blends of two alike polymers, such as blends of polystyrene (PS) with poly(α-methyl styrene) (PαMS) [7–13]. Most blends involving PHB and PLLA are mixtures of two polymers that interact with each other via either C=O/C=O or C=O/C–O group, which is one type of weak polar-polar interactions.

Apparently, the phase behavior in blends of two polymers that do not particularly interact strongly with each other, such as between PHB-polyesters may depend on types of functional groups as well other structural contributions of either of two polymers. Although PHB has been earlier proven to be miscible with poly(ethylene oxide) (PEO) [14–17], it is also known that PHB is not miscible with either poly(propylene oxide) (PPO) or poly(methylene oxide) (POM). Thus, PHB can be miscible with some ether-containing polymers, but not with all of them. POM, PEO, or PPO all have an ether linkage in the main chain, but they differ in main chain structures in terms of varying ratios of the methylene to ether group (–CH_2–/–O–). Such results suggest that interactions between C=O of PHB and C–O group or C=O groups in other polymers are possible, but not all such interactions lead to miscibility. Apparently, structures of the polymers containing these groups (C=O or –O–) are contributing to final outcome of phase behavior. Similarly, it could be expected that PHB might be miscible with some of the aliphatic polyesters with C=O group in the main chains as long as the structures of the polyesters jointly favor an intermolecular interaction between PHB and the polyesters. It should be noted here that blends with UCST behavior are usually evasive for exact characterization. Blends of PHB/poly(methyl methacrylate) (PMMA) have been claimed by various investigators to be miscibility [18–20], partial miscibility, or utterly immiscibility with two T_g's [16], while there is only one truth. More interestingly, as the structure of PMMA is replaced with poly(methyl acrylate) (PMA), full miscibility has been reported in PHB/PMA blend [21].

Blend of PHB with poly(1,4-butylene adipate) PBA (M_w = 14 000 g/mol) has been proven to be immiscible by enzymatic degradation observation and its immiscibility is needed to be investigated more to ensure whether the blend is partially or completely immiscible [22]. In continuing on a concurrent investigation on the phase behavior of blends of PLLA with polyesters [23], for comprehensive comparisons, this study further aimed at probing the temperature dependence of phase behavior and phase diagrams of blends systems composed of PHB with a series of aliphatic polyesters of different structures, such as PBA, PEA, poly(trimethylene adipate) (PTA), and PESu, which differ from each other by the CO/CH_2 ratio in the polyester's repeat units. In addition, effects of interactions between PHB and polyesters on the crystalline phase and morphology were analyzed.

2. Experimental

2.1. Materials and procedures

PHB was purchased from Polysciences, Inc. (USA), which has M_w of 500 000 g/mol, PDI = 1.42, T_g = –4°C, and T_m = 167°C. PBA, was obtained from Sigma-Aldrich Inc. (USA), with M_w = 12 000 g/mol, PDI = 1.30, T_g = –68°C, T_m = 54°C, T_d = 250°C. PTA was obtained from Scientific Polymer Products (SP^2), Inc. (USA), with M_w = 8900 g/mol, PDI = 1.28, T_g = –60°C, T_m = 38°C. PEA was from Sigma-Aldrich Inc. (USA), with M_w = 10 000 g/mol, PDI = 1.30, T_g = –50°C, T_m = 45°C. PESu was from SP^2 (USA), with M_w = 10 000 g/mol, PDI = 1.9, T_g = –19°C, T_m = 102°C. The molecular weights for most polyesters in this study, with one exception, are

Table 1. Structures, molecular weights, and physical properties of polyesters used in this study

Aliphatic polyesters	Structures	(CH_2/CO) ratio
Poly(ethylene succinate), PESu	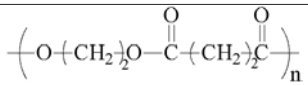	2.0
Poly(ethylene adipate), PEA	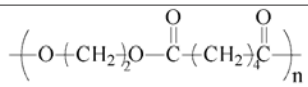	3.0
Poly(trimethylene adipate), PTA	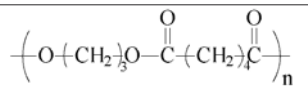	3.5
Poly(1,4-butylene adipate), PBA	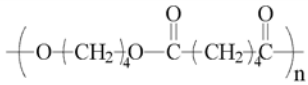	4.0

high enough to be ~10 000 g/mol. The structures of the polyesters vary in a trend represented by the average ratio of methylene per carbonyl (CH_2/CO) in main chains as shown in Table 1. Except for PESu, T_g's of these polyesters are between –50 to –70°C, which are quite far away from that of PHB (~0°C).

Blend samples of PHB/polyester were prepared using solvent-mixing, followed by film casting. PHB was purified prior to solvent-mixing. 4 wt% of total polymers in the solvent was dissolved and well stirred in flasks kept just below 40°C. Solvent in polymer mixtures during film casting was first allowed to evaporate by convection under hood for 24 h at 45°C. The blend films were further dried in vacuum at ~45°C for 72 h to drive off residual solvent.

2.2. Apparatus and procedures

Polarized-light optical microscopy (POM)

POM (Optiphot-2-POL, Nikon, Japan) equipped with a charge-coupled device (CCD) digital camera, was used for observing the phase structure of as-cast blends and for monitoring phase transition of blends upon heating. Blend samples were cast as thin films (solvent cast at controlled temperatures and vacuum drying) and placed on a microscope heating stage (Linkam THMS-600 with TP-94 temperature programmer) for OM examination. Recording of temperature dependence of phase transtions in blends was monitored at heating rate of 2°C/min from ambient to phase transition. Growth of spherulites in PHB/polyester blends was observed on CCD digital camera/video. The growth was directly recorded and analyzed via a CCD software package, which allowed the size of the spherulites in samples be conveniently and automatically measured/recorded at set intervals. The cast-films of PHB/polyester blends with the free surface (i.e. uncovered) upward were first melted on one hot stage at 190°C for 3 min, and then were rapidly transported to the microscopic heating stage pre-set at desired T_c. The purpose was to quickly bring the samples to a designated isothermal crystallization temperature, with minimum temperature lag.

Differential scanning calorimetry (DSC)

Thermal transitions of blends were characterized with a differential scanning calorimeter (DSC-7, Perkin-Elmer Corp., USA) equipped with an intracooler for quenching and cooling. Before each T_g measurements, samples were first uniformized in DSC cells (furnace and sample holders) by heating to about 190°C and quenched to sub-ambient (–60°C) before initiating the second scans at 20°C/min. DSC traces were recorded as the second scans. Prior to DSC runs, the temperature and heat of transition of the instrument were calibrated with indium or zinc standards. A continuous nitrogen flow in the DSC sample cell was maintained.

Gel permeation chromatography (GPC)

GPC (Waters, USA) system with styragel® GPC columns (styragel® HR 1, 3, and 4) was used for measuring the M_w and PDI of all samples. Calibration was performed using polystyrene standards.

3. Results and discussion

3.1. Phase and thermal behavior

Blends of PHB with polyesters were preliminarily examined for phase transition upon heating using an OM hot stage. The OM graphs for as-cast

PHB/PTA = 80/20, 50/50 at ambient were initially filled with crystals and small spherulites; however, upon heating the samples to T = 180°C (above T_m of PHB), the crystals melted and the blends turned into a homogeneous phase at T = 180°C, and they remained homogeneous upon further heating from 180 to ~250°C. These results indicate that without the solvent induced PHB/polyester crystals, the blends in the amorphous state were homogeneous. Proving evidence for homogeneity using the T_g criteria will be discussed in later sections. For the PHB/PESu and PHB/PEA blend, however, phase transition is different from the PHB/PTA blend, indicating that the different structure in PESu (from the other polyesters) influences the result of blend's phase behavior.

For details on morphology transitions, Figure 1 shows illustrative OM graphs and scheme plots for as-cast PHB/PESu blend of compositions (25/75, 50/50, 75/25) upon heating from ambient to 176°C for PHB crystal melting, then gradually a maximum 230°C (at ~2°C/min rate). The as-cast PHB/PESu blend at ambient were initially filled with crystals of small spherulites. Upon heating the samples to T = 180°C (slightly above T_m = 167°C for PHB), the crystals melted, revealing apparent two-phase domains in the PHB/PESu blend. That is, by excluding the crystals, the blend was not a homogeneous phase at T = 180°C. However, PHB/PESu blends eventually achieved a homogeneous state with no visible domains upon further heating to 220–230°C, and remained free of domains up to ~250°C or higher. Further similar experiments of heating using an OM hot stage yielded that the phase transition temperature varied with the blend compositions. For brevity, not all OM results for other blend compositions are shown here. In all, the PHB/PESu blend samples might go through a thermodynamic phase transition from separation to homogeneous phase upon heating, which is known as UCST behavior.

OM characterization on temperature dependence of phase domains in another blend, PHB/PEA, was also performed. Figure 2 shows illustrative OM graphs and scheme plots for as-cast PHB/PEA blend of compositions (25/75, 50/50, 75/25) upon heating from ambient to ~176°C for PHB crystal melting, then gradually to a maximum 230°C (at ~2°C/min rate). The PHB/PEA blend was found to go through similar phase transition like that in the PHB/PESu blend, except that the transition at which the blend turned from two phases to one phase took place at lower temperatures (~190°C).

Figure 3 summarizes the phase diagrams and UCST for PHB/PESu and PHB/PEA blends of various compositions. The 'clarity point' is defined as the temperature at which the blend samples turn from phase separation (cloudy) into homogeneity with no domains (clear), which apparently depends on the blend compositions. The maximum point is known

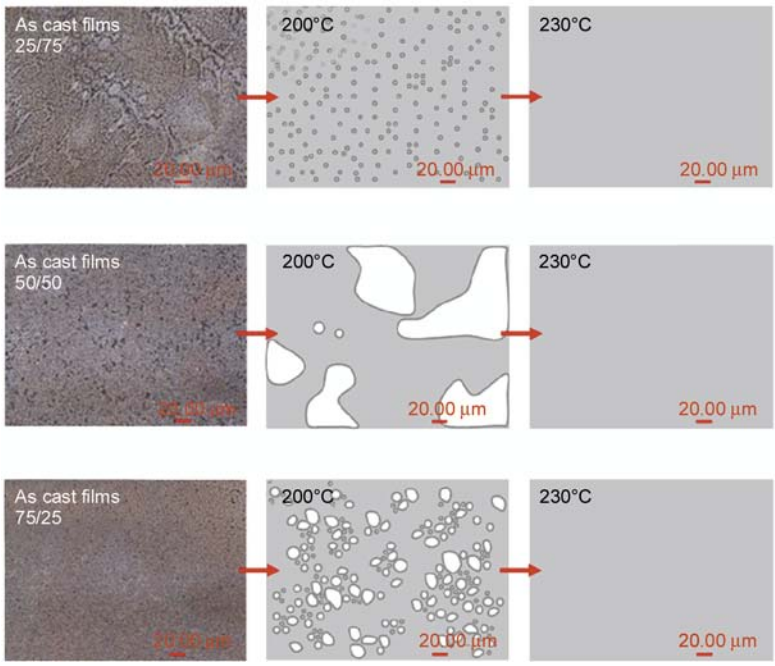

Figure 1. OM graphs and schemes for phase domains in PHB/PESu blend of three compositions (25/75, 50/50, 75/25)

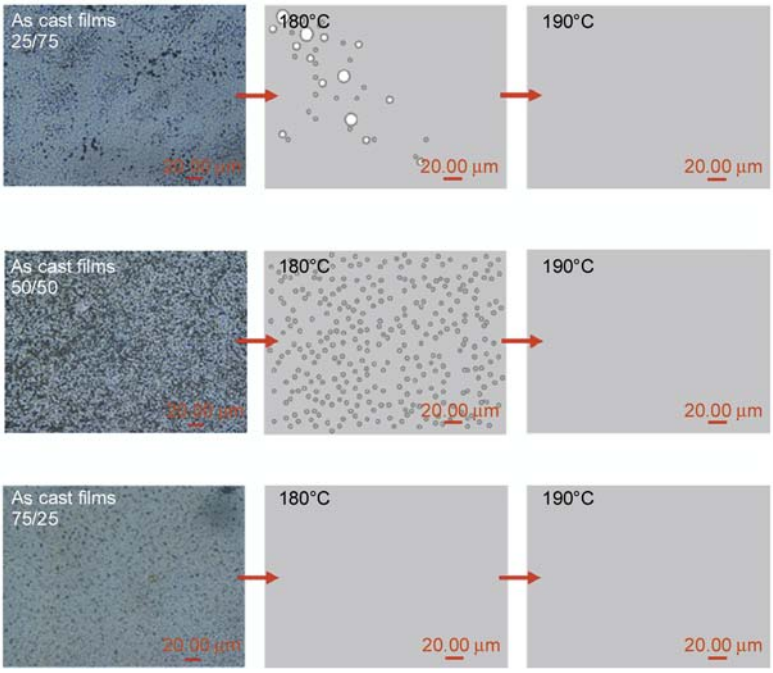

Figure 2. OM graphs and scheme plots for phase domains in PHB/PEA blend of three compositions (25/75, 50/50, 75/25)

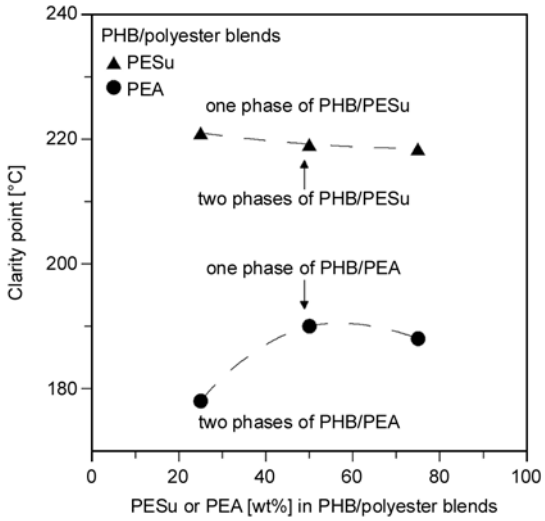

Figure 3. Phase diagrams showing UCST temperature dependence for PHB/PESu and PHB/PEA blends as a function of composition

as the UCST = 221°C, whose physical meaning is that the blends of all compositions will be one phase at or above this temperature. The asymmetry in the UCST phase curve is expected due to the difference in molecular weight distributions in these two constituents.

3.2. Immiscibility, UCST and reversibility

Rapid quenching of the blend from above UCST was expected to freeze the blends state into a quasi-miscible state. Subsequent DSC scanning on the quench-then-frozen blend samples was performed to reveal T_g behavior. Figure 4 shows DSC thermograms for PHB/PESu blend of different compositions: (a) 2nd scan after quenching from 190°C (below UCST), and (b) 2nd scan after quenching from 240°C (above UCST). The DSC traces were all 2nd scans on the samples after they were heated to either 190 or 240°C (UCST = 221°C) briefly, then rapid quenched to sub-ambient to freeze the UCST state. DSC traces in Figure 4a apparently show that the blend samples heat to 190°C then quenched are still phase separated; by comparison, all DSC traces in Figure 4b show a single composition-dependent T_g for all compositions in the UCST-quenched blends (heat to 240°C then quenched). Figure 5 shows T_g vs. composition for PHB/PESu blend (by quenching from above UCST). The T_g-composition relationship in exhibits asymmetry in the dependence of T_g with composition. The relationship indicates a homogeneous phase in the blend. However, it must be noted here that the blend was locked into a quasi-homogeneous state as the samples were just freshly quenched from above UCST. With time at temperature for chain mobility, the blend might revert back to phase separation.

Figure 6 shows DSC thermograms for PHB/PEA blend of different compositions: (a) 2nd scan after quenching from 180°C, and (b) 2nd scan after quenching from 200°C. For blends either quenched from 180 or 200°C, the 2nd DSC scans on the samples

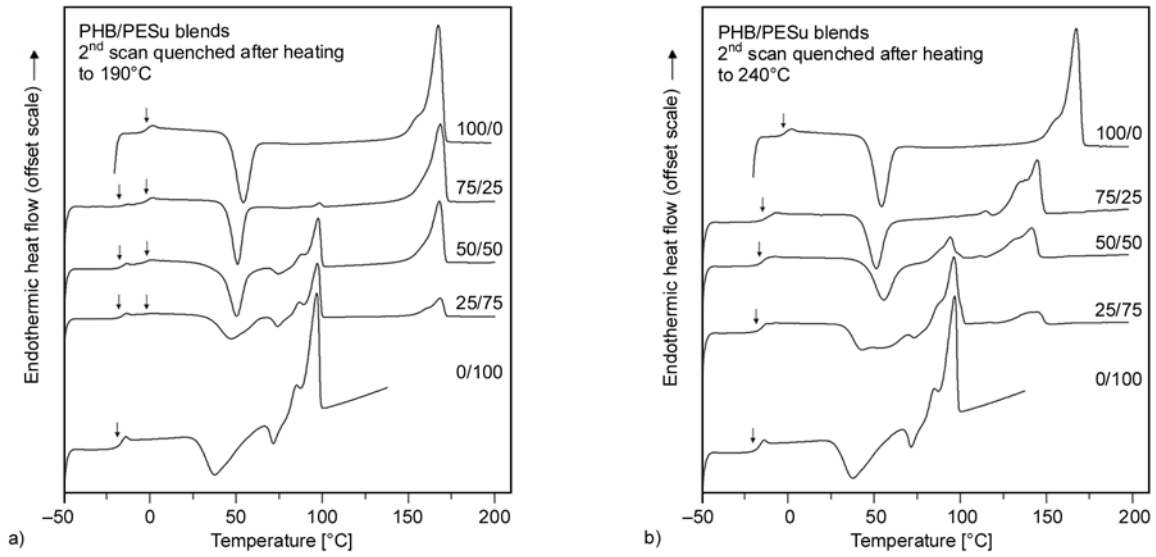

Figure 4. DSC thermograms for PHB/PESu blend of different compositions: (a) 2nd scan after quenching from 190°C (below UCST), and (b) 2nd scan after quenching from 240°C (above UCST)

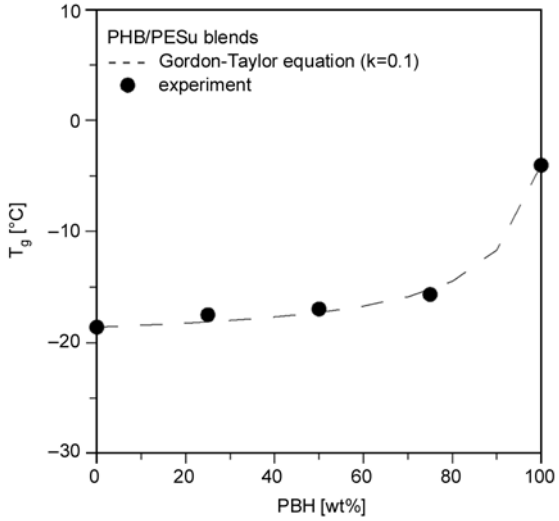

Figure 5. T_g vs. composition for PHB/PESu blend (quenched from above UCST)

revealed distinct T_g signal related to PEA, indicating immiscibility of the PHB/PEA blend immediately upon cooling back to below UCST. This DSC result indicates that the PHB/PEA blend could be reverted immediately back to immiscibility upon cooling from UCST state.

Phase reversibility from UCST back to immiscibility at ambient temperature in cooling cycles was further verified for PHB/PESu and PHB/PEA blends. First, the PHB/PESu blend sample was heated to above UCST, then cooled –2°C/min from UCST = ~240 to 180°C (above T_m but below UCST). When cooled from UCST to 130°C, the blend did not revert immediately back to phase separation. However, this might be due to chain mobility highly retarded by viscosity. Scientific rigor requires proof that the UCST is a truly thermodynamic process without chemical reactions, such as transesterification, etc. leading to phase changes upon heating. Instead, the UCST-quenched homogeneous blend was dissolved in solvent, re-cast to films, which was then characterized using OM. Apparently, the UCST in the blend could be made to be reversible when viscosity was reduced by solvent. Chemical reactions are not responsible for the phase homogeneity of blend upon heating. If any chemical reactions had been the factors for phase transition into blend homogeneity, then the UCST-quenched blend could not have been reverted back to original phase separation by solvent re-dissolving.

Figure 7 shows OM graphs showing temperature dependence of domains in solvent-recast PHB/PESu or PHB/PEA blend samples that had been heated to UCST: (a) PHB/PESu (50/50), and (b) PHB/PEA (50/50). The OM graphs show that the solvent re-cast samples of UCST-quenched PHB/PESu (50/50) blend were initially filled with phase domains and tiny crystals and small spherulites. Upon re-heating the samples to 180°C (above T_m of PHB), the PHB crystals completely melted, but the phase domains are still apparent. This indicates that the UCST-quenched blend sample was reverted back to phase separation assisted by solvent re-dissolution. The re-cast blend samples upon further heating above T_m eventually achieved again a homogeneous state with no visible domains upon further

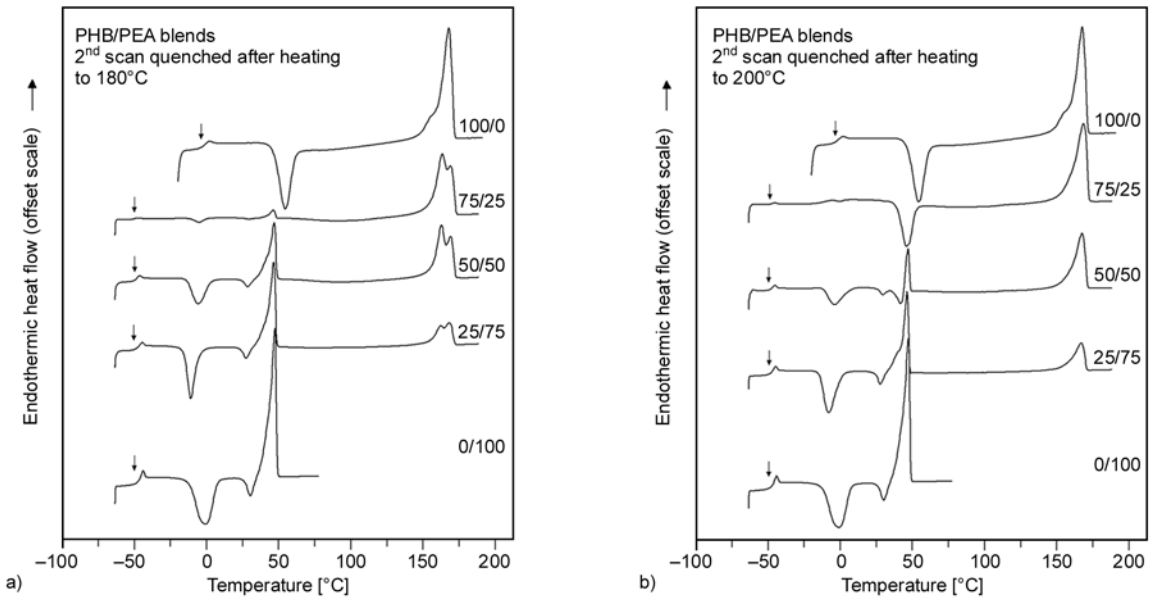

Figure 6. DSC thermograms for PHB/PEA blend of different compositions: (a) 2nd scan after quenching from 180°C, and (b) 2nd scan after quenching from 200°C

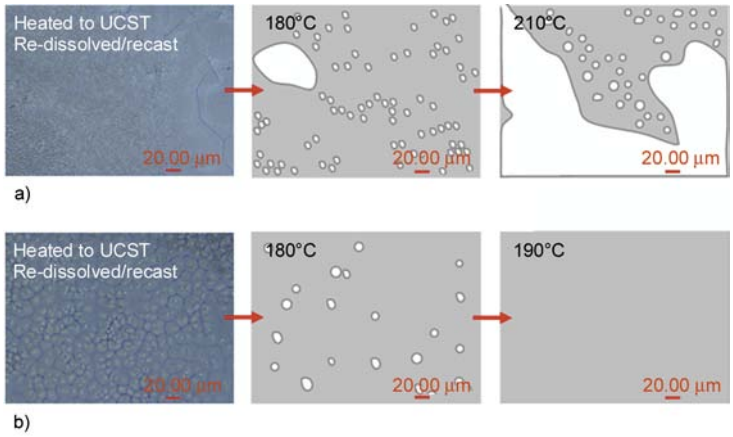

Figure 7. OM graphs showing reversible UCST temperature dependence of domains in solvent-recast PHB/polyester blends samples that had been heated to UCST: (a) PHB/PESu (50/50), and (b) PHB/PEA (50/50) blend

heating to 230°C, and remained free of domains. In this figure, only the blend composition of 50/50 is used as an example for demonstration; but same results were found for all other blend compositions of PHB/PEA and PHB/PESu.

3.3. Miscibility and crystalline morphology

Thermal analysis was performed to reveal T_g, T_c, and T_m in the PHB/polyester blends of several compositions. Figure 8 shows DSC thermograms for PHB/PTA blend of different compositions. There is only a single, composition-dependent T_g, indicating miscibility. Most miscible binary blends usually follow a relationship as described by the classically known Fox Equation (1):

$$\frac{1}{T_g} = \frac{w_1}{T_{g1}} + \frac{w_2}{T_{g2}} \tag{1}$$

Or alternatively, the T_g data can be fitted with the Gordon-Taylor Equation (2) [24]:

$$T_g = \frac{w_1 T_{g1} + k w_2 T_{g2}}{w_1 + k w_2} \tag{2}$$

The PHB/PTA blend shows a single T_g for compositions up to PTA = 50 wt%, and the T_g shift with compositions within this range. For PTA > 50 wt%, however, the T_g does not shift so much with composition, although the phase morphology of the blend with PTA > 50 wt% is indeed single-phase. The thermal evidence may still not so strong to indicate miscibility in full range, but partially miscibility up to

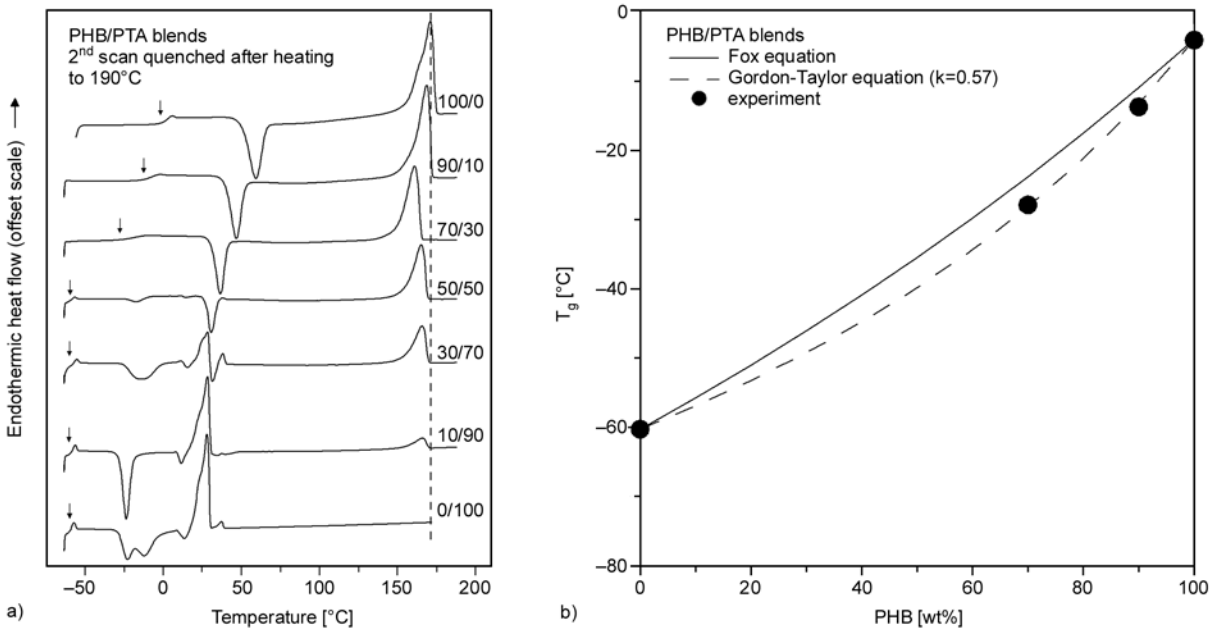

Figure 8. (a) DSC thermograms for the PHB/PTA blend of different compositions, and (b) T_g vs. composition curve

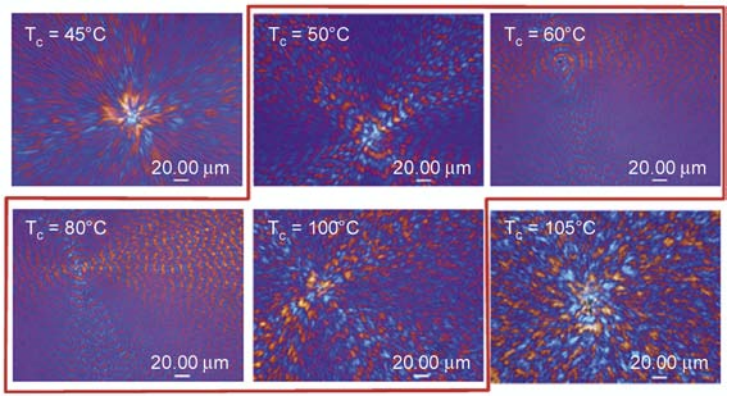

Figure 9. POM graphs showing ring-banded morphology in PHB/PTA (50/50) spherulites crystallized at various T_c as indicated

50 wt% of PTA in PHB/PTA blend is plausible. Fitting of the T_g data within the partial miscibility range with the Gordon-Taylor T_g model led to k = 0.57. The high value of the G-T k parameter suggests that the miscible PHB/PTA blend has excellent homogeneity. The T_g-vs.-composition relationship shows pretty good fitting with the Fox equation. Miscibility in the amorphous phase of a miscible blend generally influences the crystalline morphology. Figure 9 displays POM graphs showing ring-banded morphology in the miscible PHB/PTA (50/50) blend crystallized at various T_c as indicated. Note that most immiscible crystalline/crystalline polyester/polyester blends exhibit either disrupted or highly distorted ring-banded patterns in crystallized spherulites upon crystallization. Miscibility, on the other hand, tends to retain the patterns of ring bands in crystallized spherulites in blends. Between T_c = 50 to 100°C, the PHB/PTA (50/50) blend crystallizes into ring-banded spherulites with various regularity or inter-ring spacing depending on T_c.

The inter-ring spacing and growth rates were measured for the miscible PHB/PTA blend. Figure 10 shows (a) average ring spacing, and (b) spherulite growth rate as functions of T_c for PHB/PTA (50/50) blend. For the PHB/PTA blend, the crystallized spherulites are all ring-banded at T_c = 50 to 100°C; by comparison, the neat PHB crystallizes into ring-banded spherulites at a slightly narrower temperature range. Neat PHB, crystallized at 40°C or lower, exhibits ringless spherulites with distinct Maltese-cross extinction. Only when crystallized at the range of ~50–90°C, the PHB spherulites are characterized with concentric ring bands of varying inter-

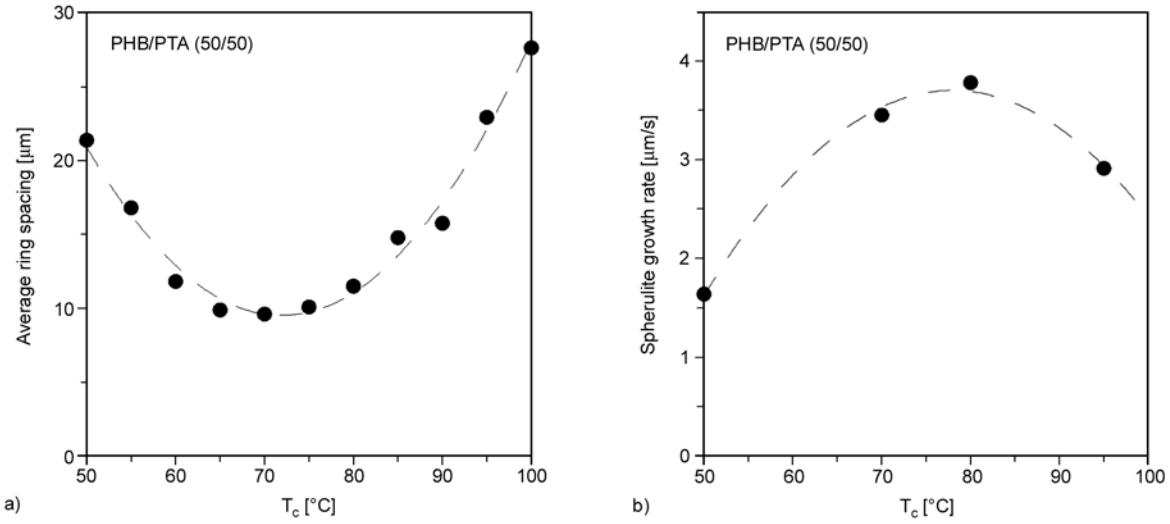

Figure 10. (a) inter-ring spacing, and (b) spherulite growth rate as a function of T_c for PHB/PTA (50/50) blend

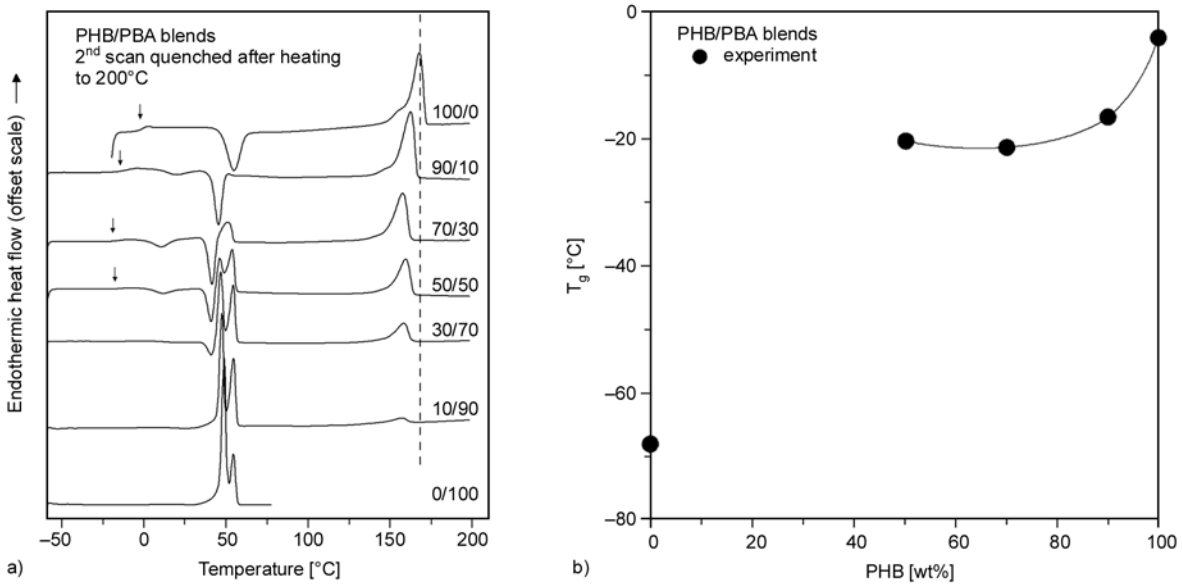

Figure 11. (a) DSC thermograms for the PHB/PBA blend of different compositions, and (b) T_g vs. composition relationship indicating a two-phase mixture

ring spacing. When crystallized at 100°C or higher, the spherulites in neat PHB become ringless again. The lower-T_g PTA component widens and lowers the T_c range of forming ring-banded spherulites. For the PHB/PTA blend, the inter-ring spacing of the ring-banded spherulites are the narrowest at T_c = 70–80°C, which corresponds to the greatest spherulite growth rate.

Figure 11 shows (a) DSC thermograms for the PHB/PBA blend of different compositions, and (b) T_g vs. composition relationship indicating a two-phase mixture for intermediate blend compositions. The DSC thermograms for the PHB/PBA blend suggest that partial miscibility exists, as indicated by blend T_g lowering by PBA wt% up to a limit. But phase separation eventually takes place in the blend compositions with PBA contents equal to or greater than 50 wt%. Note also that the apparent T_m of the blend initially shifted with increasing PBA content, but is stabilized at a nearly constant value as the PBA contents approach 50 wt% or greater.

Figure 12 shows OM micrographs of spherulites in PHB/PBA (50/50) blend crystallized at various T_c = 55–110°C, within which ring bands in spherulites of the PHB/PBA blend can be seen. The OM graphs show that phase domains are seen along with the ring banded spherulites when cooled and crystallized at T_c. Inset POM graph (right side) for PHB/

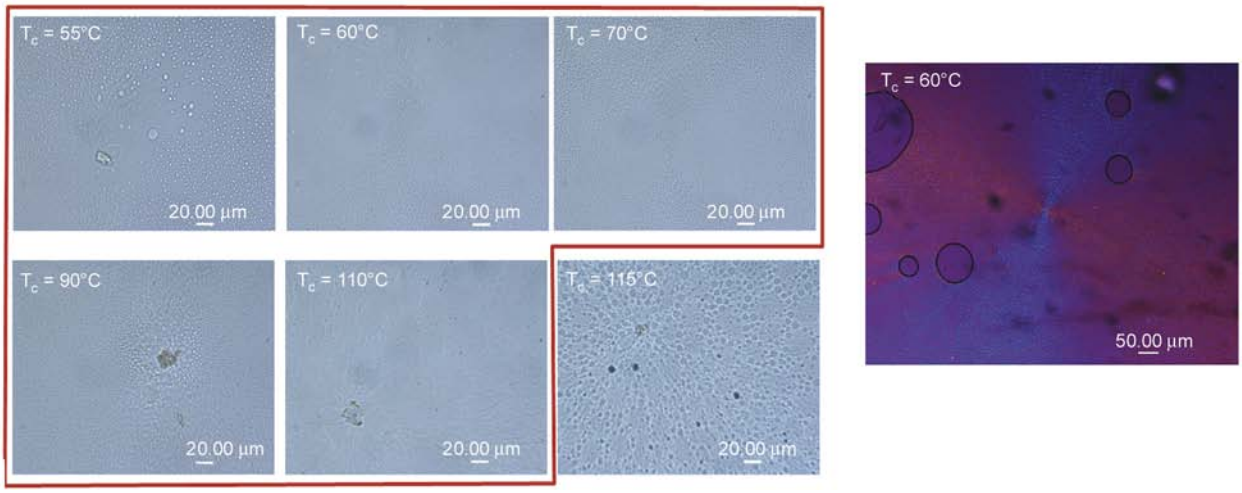

Figure 12. OM micrographs of spherulites in PHB/PBA (50/50) blend crystallized at various T_c = 55–115°C

PBA (50/50) crystallized at T_c = 60°C shows that ring-banded spherulites are obvious in POM, but phase-separation domains cannot be clearly visible using polarized light as the more distinct crystal structures cover up the less obvious phase-domain images. For this reason, the spherulite crystals and phase separation domains were monitored as functions of temperature using POM and OM respectively. Upon holding at T_c for crystallization of the blend, ring-banded PHB spherulites appeared first, then phase domains of PBA appeared after the crystals are formed. Very likely, the crystals induced phase separation in the blends. Upon heating the blend back to higher temperatures, the ring-banded spherulites first melted at T = 176°C under OM hot stage, then the domains disappeared upon heating to about 176–180°C for most blend compositions. Apparently, UCST in the PHB/PBA blend is located at 178–180°C for all compositions.

4. Conclusions

Phase behavior and miscibility in blends comprising biodegradable PHB and aliphatic polyesters were investigated. Miscibility in partial composition range (PTA contents in blend lower than 50 wt%) is seen in the blends of PHB with an aliphatic polyester, PTA. As the PHB/PTA blend shows a single-phase morphology, no UCST could be observed upon heating. The crystalline/crystalline PHB/PTA blend (50/50), within the miscible range, exhibits ring-banded spherulites at T_c = 50~100°C, with inter-ring spacing dependent on T_c. All immiscible or partially miscible PHB/polyester blends, by contrast, exhibit disrupted ring-banded spherulites or discrete spherical phase domains upon cooling from UCST to crystallization. The blends of PHB with all other aliphatic polyesters are partially miscible (with PBA) or immiscible (with PESu, or PEA) with a UCST at 180~221°C depending on blend composition. UCST with reversibility was verified. Heating to above UCST and quick quenching was proven to preserve the UCST blend into a homogeneous glass state with a single T_g upon DSC scanning, and thermodynamic reversibility of the UCST behavior in the blend was proven by solvent recasting. The chemical structures of the aliphatic polyesters apparently influence the phase behavior. Lower carbonyl density in the aliphatic polyesters leads to less likelihood for miscibility or UCST in the PHB/polyester blends.

Acknowledgements

This work has been financially supported by a basic research grant (NSC 96-2221-E-006-099-MY3) for three consecutive years from Taiwan's National Science Council (NSC), to which the authors express their gratitude.

References

[1] Lu J., Qiu Z., Yang W.: Fully biodegradable blends of poly(L-lactide) and poly(ethylene succinate): Miscibility, crystallization, and mechanical properties. Polymer, **48**, 4196–4204 (2007).
DOI: 10.1016/j.polymer.2007.05.035

[2] Woo E. M., Hsieh Y-T., Chen W-T., Kuo N-T., Wang L-Y.: Immiscibility–miscibility phase transformation in blends of poly(ethylene succinate) with poly(L-lactic acid)s of different molecular weights. Journal of Polymer Science Part B: Polymer Physics, **48**, 1135–1147 (2010).
DOI: 10.1002/polb.21999

[3] Kumagai Y., Doi Y.: Enzymatic degradation of binary blends of microbial poly(3-hydroxybutyrate) with enzymatically active polymers. Polymer Degradation and Stability, **37**, 253–256 (1992).
DOI: 10.1016/0141-3910(92)90167-4

[4] Blümm E., Owen A. J.: Miscibility, crystallization and melting of poly(3-hydroxybutyrate)/poly(L-lactide) blends. Polymer, **36**, 4077–4081 (1995).
DOI: 10.1016/0032-3861(95)90987-D

[5] Focarete M. L., Scandola M., Dobrzynski P., Kowalczuk M.: Miscibility and mechanical properties of blends of (L)-lactide copolymers with atactic poly(3-hydroxybutyrate). Macromolecules, **35**, 8472–8477 (2002).
DOI: 10.1021/ma020940z

[6] Nurkhamidah S., Woo E. M.: Cracks and ring bands of poly(3-hydroxybutyrate) on pre-crystallized poly(L-lactic acid) template. Industrial and Engimeering Chemistry Research, in press (2011).
DOI: 10.1021/ie1024547

[7] Saeki S., Cowie J. M. G., McEwen I. J.: The effect of molecular weight and casting solvent on the miscibility of polystyrene-poly(α-methyl styrene) blends. Polymer, **24**, 60–64 (1983).
DOI: 10.1016/0032-3861(83)90081-2

[8] Cowie J. M. G., McEwen I. J.: Predicted miscibility of polystyrene and poly(α-methyl styrene) and comparison with experiment. Polymer, **26**, 1662–1666 (1985).
DOI: 10.1016/0032-3861(85)90283-6

[9] Widmaier J-M., Mignard G.: Polystyrene-poly(α-methylstyrene) blends: Influence of molecular weight on miscibility. European Polymer Journal, **23**, 989–992 (1987).
DOI: 10.1016/0014-3057(87)90046-2

[10] Lin J-L., Roe R-J.: Relationship among polymer-polymer interaction energy densities and the deuterium isotope effect. Macromolecules, **20**, 2168–2173 (1987).
DOI: 10.1021/ma00175a021

[11] Schneider H. A., Dilger P.: DSC and TMS study of polystyrene/(poly(α-methylstyrene) blends. Polymer Bulletin, **21**, 265–272 (1989).
DOI: 10.1007/BF00955917

[12] Rameau A., Gallot Y., Marie P., Farnoux B.: Deuterated polystyrene-poly(α-methylstyrene) blends: Range of miscibility and determination of the interaction parameter by small angle neutron scattering. Polymer, **30**, 386–392 (1989).
DOI: 10.1016/0032-3861(89)90002-5

[13] Callaghan T. A., Paul D. R.: Interaction energies for blends of poly(methyl methacrylate), polystyrene, and poly(α-methyl styrene) by the critical molecular weight method. Macromolecules, **26**, 2439–2450 (1993).
DOI: 10.1021/ma00062a008

[14] Avella M., Martuscelli E.: Poly-d-(−)(3-hydroxybutyrate)/poly(ethylene oxide) blends: Phase diagram, thermal and crystallization behaviour. Polymer, **32**, 1731–1737 (1988).
DOI: 10.1016/0032-3861(88)90384-9

[15] Avella M., Martuscelli E., Raimo M.: The fractionated crystallization phenomenon in poly(3-hydroxybutyrate)/poly(ethylene oxide) blends. Polymer, **34**, 3234–3240 (1993).
DOI: 10.1016/0032-3861(93)90396-R

[16] Yoon J. S., Choi C. S., Maing S. J., Choi H. J., Lee H-S., Choi S. J.: Miscibility of poly-d(−)(3-hydroxybutyrate) in poly(ethylene oxide) and poly(methyl methacrylate). European Polymer Journal, **29**, 1359–1364 (1993).
DOI: 10.1016/0014-3057(93)90194-K

[17] You J-W., Chiu H-J., Don T-M.: Spherulitic morphology and crystallization kinetics of melt-miscible blends of poly(3-hydroxybutyrate) with low molecular weight poly(ethylene oxide). Polymer, **44**, 4355–4362 (2003).
DOI: 10.1016/S0032-3861(03)00348-3

[18] Canetti M., Sadocco A., Siciliano A., Seves A.: Investigation of the phase structure of poly(d(−)3-hydroxybutyrate)/atactic poly(methyl methacrylate) blends by small-angle X-ray scattering. Polymer, **35**, 2884–2887 (1994).
DOI: 10.1016/0032-3861(94)90324-7

[19] Siciliano A., Seves A., De Marco T., Cimmino C., Martusecelli E., Silvestre C.: Miscibility and thermal and crystallization behaviors of poly(D-(−)-3-hydroxybutyrate)/atactic poly(methyl methacrylate) blends. Macromolecules, **28**, 8065–8072 (1995).
DOI: 10.1021/ma00128a014

[20] Cimmino S., Iodice P., Silvestre C., Karasz F. E.: Atactic poly(methyl methacrylate) blended with poly(3-D(−)hydroxybutyrate): Miscibility and mechanical properties. Journal of Applied Polymer Science, **75**, 746–753 (2000).
DOI: 10.1002/(SICI)1097-4628(20000207)75:6<746::AID-APP3>3.0.CO;2-J

[21] An Y., Dong L., Li G., Mo Z., Feng Z.: Miscibility, crystallization kinetics, and morphology of poly(β-hydroxybutyrate) and poly(methyl acrylate) blends. Journal of Polymer Science Part B: Polymer Physics, **38**, 1860–1867 (2000).
DOI: 10.1002/1099-0488(20000715)38:14<1860::AID-POLB40>3.0.CO;2-#

[22] Kumagai Y., Doi Y.: Enzymatic degradation and morphologies of binary blends of microbial poly(3-hydroxy butyrate) with poly(ε-caprolactone), poly(1,4-butylene adipate and poly(vinyl acetate). Polymer Degradation and Stability, **36**, 241–248 (1992).
DOI: 10.1016/0141-3910(92)90062-A

[23] Hsieh Y. T., Kuo N. T., Woo E. M.: Thermal and phase behaviour of poly(L-lactic acid) interacting with other polyesters. Journal of Thermal Analysis and Calorimetry, submitted (2011).

[24] Gordon M., Taylor J. S.: Ideal copolymers and the second-order transitions of synthetic rubbers. I. Non-crystalline copolymers. Journal of Applied Chemistry, **2**, 493–500 (1952).
DOI: 10.1002/jctb.5010020901

eXPRESS Polymer Letters Vol.5, No.7 (2011) 581–590
Available online at www.expresspolymlett.com
DOI: 10.3144/expresspolymlett.2011.57

The effects of particle size and content on the thermal conductivity and mechanical properties of Al_2O_3/high density polyethylene (HDPE) composites

S. Zhang[1,2], *X. Y. Cao*[1], *Y. M. Ma*[1*], *Y. C. Ke*[1], *J. K. Zhang*[1], *F. S. Wang*[1]

[1]Beijing National Laboratory for Molecular Sciences, Laboratory of New Materials, Institute of Chemistry, Chinese Academy of Sciences, Beijing 100190, P. R. China
[2]Graduate School of Chinese Academy of Sciences, Beijing 100190, P. R. China

Received 26 October 2010; accepted in revised form 10 January 2011

Abstract. The influences of filler size and content on the properties (thermal conductivity, impact strength and tensile strength) of Al_2O_3/high density polyethylene (HDPE) composites are studied. Thermal conductivity and tensile strength of the composites increase with the decrease of particle size. The dependence of impact strength on the particle size is more complicated. The SEM micrographs of the fracture surface show that Al_2O_3 with small particle size is generally more efficient for the enhancement of the impact strength, while the 100 nm particles prone to aggregation due to their high surface energy deteriorate the impact strength. Composite filled with Al_2O_3 of 0.5 μm at content of 25 vol% show the best synthetic properties. It is suggested that the addition of nano-Al_2O_3 to HDPE would lead to good performance once suitably dispersed.

Keywords: *polymer composites, mechanical properties, thermal conductivity*

1. Introduction

Polymers with excellent electrical insulation have been extensively used as packing materials in electrical devices due to their good process ability, light weight and low cost. Nevertheless, the thermal conductivity of polymers are generally very low (i.e. 0.10–0.25 $W/m^{-1}\cdot K^{-1}$), and it has been widely recognized that the thermal conductivity of these polymers has to be enhanced to lower the energy loss and increase the stability of the devices. With the increasing demand for high density power and energy transmission of electronic devices, fabrication of insulating polymer materials with high thermal conductivity has become crucial [1–4].

High crystallization and orientation of polymer can greatly enhance the thermal conductivity along the orientation direction, but they usually have difficulties of processing [5]. Blending of polymer with inorganic fillers is an effective and convenient way to enhance the polymer thermal conductivity while maintaining the electrical insulation, such as polymer composites with boron nitride (BN) [6, 7], aluminum nitride (AlN) [2, 3], silicon nitride (Si_3N_4) [8, 9], alumina [10], silicon carbride (SiC) [11] and silica (SiO_2) etc. [12] have been investigated. In the inorganic filler/polymer composites, the thermal conductivity increases with the filler content. Very high filler loading is often used to obtain high thermal conductivity. However, it seriously alters the polymer component and can form agglomerates, which induces stress concentration and decrease of the tensile strength, modulus and ductility of the material [13], so the practical application of thermal conductive polymer composites is limited.

*Corresponding author, e-mail: maym@iccas.ac.cn

Filler size and shape are also important factors for the thermal conductivity and mechanical properties [14, 15]. Zhou *et al.* [16] used Al_2O_3 with different size to fill silicone rubber, and reported that nano-sized Al_2O_3 composite exhibited higher thermal conductivity and mechanical properties than the micro-sized one. The influence of hybrid fillers was also investigated [17, 18]. However, reports on how to enhance the thermal conductivity and mechanical properties of the polymer composites simultaneously are still quite limited.

The particle size and content in the composite determine the average interparticle distance [19, 20], which is close related to the thermal conductivity and mechanical properties. At the same particle content, smaller particle size leads to lower interparticle distance and more chances for the formation of thermal conductive 'pathway' [21–23]. The particle size and content affect the interparticle distance and the stress state of the matrix polymer surrounding the voids. When the average interparticle distance is in a suitable range, extensive plastic deformation in the matrix can be easily induced [24–26]. So the optimization of the particle size and content can be a convenient and feasible way to prepare composites with good synthetic properties.

In this paper, Al_2O_3/HDPE composites with different alumina particle sizes (diameter of 10, 4.7, 0.5 μm and 100 nm, denoted as A10, A4.7, A0.5 and A0.1) were prepared. The influence of alumina content and particle size on thermal conductivity, impact strength and tensile strength are studied. The synthetic properties of the composites are optimized and the mechanism is also discussed.

2. Experimental

2.1. Materials

The polymer used in this study was high density polyethylene (HDPE) 5000S (SinoPec Beijing Yansan Petrochemical Co. Ltd, Beijing, China). It had a density of 0.95 g/cm^3 and a melt flow index of 0.9 g/10 min (2.16 kg at 190°C). Four types of alumina particles with average diameters of 10, 4.7, 0.5 μm and 100 nm (denoted as A10, A4.7, A0.5 and A0.1 respectively, >99 wt% purity) were used as fillers. The suppliers and parameters of the alumina particles were listed in Table 1. All of the alumina particles were of α-crystalline and the thermal conductivity was about 30 W/(m·K). The alumina particles were added to the HDPE without surface pretreatment.

2.2. Sample preparation

The blends of HDPE with various alumina particles were prepared by a two-roll mill (X(S) K-160, Double Elephant Group Company, Jiangsu, China) for 20 min. The temperature of the front roll and back roll were 140 and 130°C respectively. After extrusion, the samples were cut into small pieces.

The samples for thermal conductivity and mechanical property tests were prepared by injection molding (SZ-68/400, Liuzhou Rubber and Plastic Machinery Factory, Guangxi, China) at 200°C. The samples for thermal conductivity measurement were square bars of 50 mm in length and 4 mm in thickness. Tensile and impact bars were prepared according to ASTM D638 Type I and ASTM D256.

The maximum contents of alumina A4.7 and A0.5 in the composites were 50 vol%, but those of A10 and A0.1 were 30 vol%. The reasons for the difficulties of processing for 10 and 0.1 μm particle composites are different. The surface area of the 0.1 μm alumina particles is very large. When filler content is higher than 30 vol%, it is very difficult for HDPE to wet the surface of all nano-particles, and constrained the blending. On another hand, the 10 μm particles increase the roughness of the composite surface. When the 10 μm alumina content is higher than 30 vol%, the surface of the composite becomes too rough to measure the thermal conductivity for it can't make a good contact with heat source. The compositions were represented by the

Table 1. The suppliers and data of alumina fillers

Filler code	Supplier	Surface area* [m^2/g]	Mean particle size* [μm]	Geometrical standard deviation*
A10	Shanghai Yuejiang Titanium Chemical Manufacture Co. Ltd. CHN, Shanghai, China	0.6	10.0	1.5
A4.7	Fujian Johnson Mining Co. Ltd. CHN, Xiamen, China	1.5	4.7	2.0
A0.5	Wan Jing New Material Co. Ltd. CHN, Hangzhou, China	5.0	0.5	2.8
A0.1	Wan Jing New Material Co. Ltd. CHN, Hangzhou, China	12.5	0.1	3.6

*The values were given by the suppliers

alumina volume fraction. The real composition of the composites was measured by the calcination method, and the difference between the theoretical composition and the real one is less than 2%.

2.3. Characterization

2.3.1. Thermal conductivity

The through-plane thermal conductivity was measured at 30 and 50°C with thermal conductivity analyzer (HC-110, EKO Instruments Co. Ltd, Sasazuka Shibuya-ku, Japan).

2.3.2. Impact and tensile test

The notched Izod impact strength was measured on a ceast pendulum impact strength tester CSI-137C at 23°C (Wuzhongshi Material Tester Co. Ltd, Ningxia, China), according to ASTM D256. The drop velocity was 3.5 m/s and the testing results were the average of ten parallel measurements. The tensile measurements were carried out at 23°C using an Instron 3365 universal materials testing machine (Instron Corporation, Massachusetts, America), according to ASTM D638. The average values of the mechanical properties in this study were obtained by five independent measurements.

2.3.3. Scanning electron microscope (SEM)

The as prepared composites were cryogenically fractured in liquid nitrogen. Both the cryogenically fractured and impact fractured surfaces of composites were inspected by SEM (JSM-6700F, Japan Electron Optics Laboratory Co. Ltd, Tokyo, Japan) at an acceleration voltage of 3 kV. The surfaces of the samples were coated with a conductive platinum layer before inspection.

3. Results and discussion

3.1. Dispersion of Al_2O_3 in the HDPE matrix

The dispersion of the alumina particles differs with particle content and particle size, which determines the properties of the composites [27, 28]. The composites cryogenically fractured surfaces were inspected by SEM (Figure 1 and Figure 2).

For a certain size of alumina particle, the dispersion in the composite changes with content. Their trends are similar when the particle size $\geq$0.5 μm. The composite of A4.7/HDPE is taken as a typical example to show the influence of content on the dispersion (Figure 1a–c). When the alumina content is of 5 vol% (Figure 1a), the alumina particle is dispersed in the matrix without serious aggregation. The smooth holes on the surface of the matrix should be the spaces occupied by the alumina particles. The average interparticle distance is about several microns and the alumina particles are mostly separated without contacting each other. When the alumina content increases to 15 vol% (Figure 1b), the average interparticle distance gets smaller, and some agglomerates are formed. When the alumina content increases to 30 vol% (Figure 1c), the average interparticle distance gets even smaller and the amount of agglomerates increased, resulting in the formation of the local alumina network. Of course, inter polymer layers are existed among the particles. The red lines were added to the SEM pictures to indicate the local Al_2O_3 network. The size of the local networks increases as the filler content increasing.

The dispersion of the particles differs with particle size when the content is the same. Figure 1(c–f) show the SEM micrographs of the composites with particle size of 4.7, 10 and 0.5 μm respectively at 30 vol% alumina content. The average interparticle distance reduces with the decrease of particle size, and smaller particle size affords more connected alumina particles. Alumina particles in A10/HDPE (30 vol%) are mostly dispersed separately (Figure 1d), while connected alumina particles can be found for A4.7/HDPE at the same content. In A0.5/HDPE (30 vol%) composite, more connected alumina particles are formed.

The dispersion of alumina particles in A0.1/HDPE is somehow quite different from others that the dispersed and aggregated particles are coexisted (Figure 2a). In most area, 100 nm particles dispersed uniformly, but in some parts the particles aggregated up to several micro-meters due to the large specific surface area and high surface energy. The enlarged SEM pictures of the two parts are shown in Figure 2b and Figure 2c. Figure 1c, e, f and Figure 2b show that the number of the local alumina networks increase as the decreasing of the particle size.

3.2. Thermal conductivity of the composite

Figure 3a shows the thermal conductivity curves with alumina volume content.

Thermal conductivities of all composites increase with filler content, and the trends are similar. The

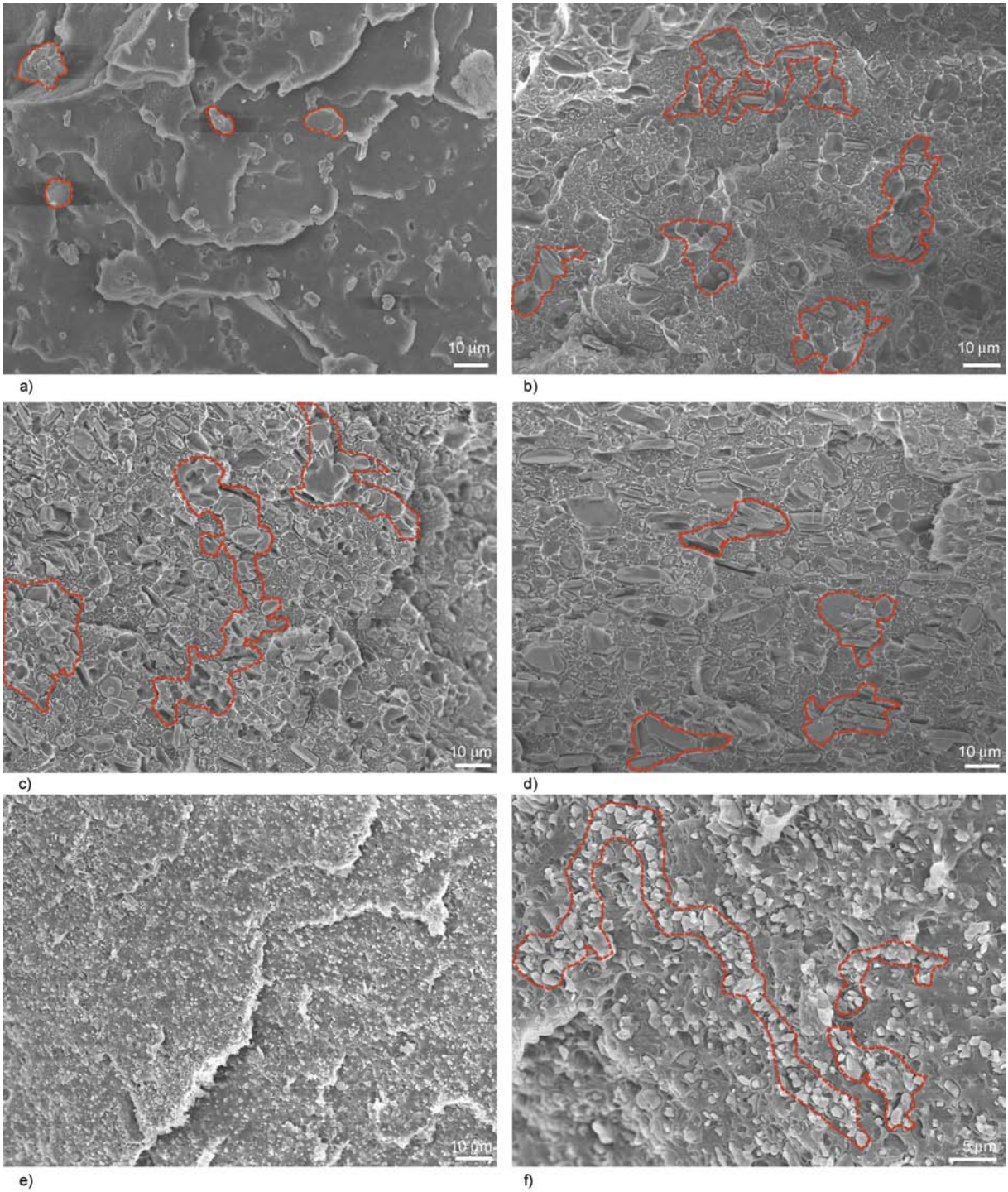

Figure 1. SEM micrographs of the cryogenically fractured surfaces of Al_2O_3/HDPE composites: (a) A4.7/HDPE (5 vol%); (b) A4.7/HDPE (15 vol%); (c) A4.7/HDPE (30 vol%); (d) A10/HDPE (30 vol%); (e) A0.5/HDPE (30 vol%); (f) A0.5/HDPE (30 vol%) in high magnification. The percentages refer to the alumina volume fraction in the composites. The red lines are added to emphasize the local network of the samples.

curves can be modeled into three stages (Figure 3b). The thermal conductivity increases more rapidly in second stage than in the first and third stages. The turning point from stage 1 to stage 2 appears at lower alumina content for composites with the smaller particle size. Different from others, the increase of the thermal conductivity of the A10/HDPE only shows the character of the first stage up to the alumina content of 30 vol%.

The isolated particles have little effect on the enhancement of the thermal conductivity until the particle form continuous pathway through the mate-

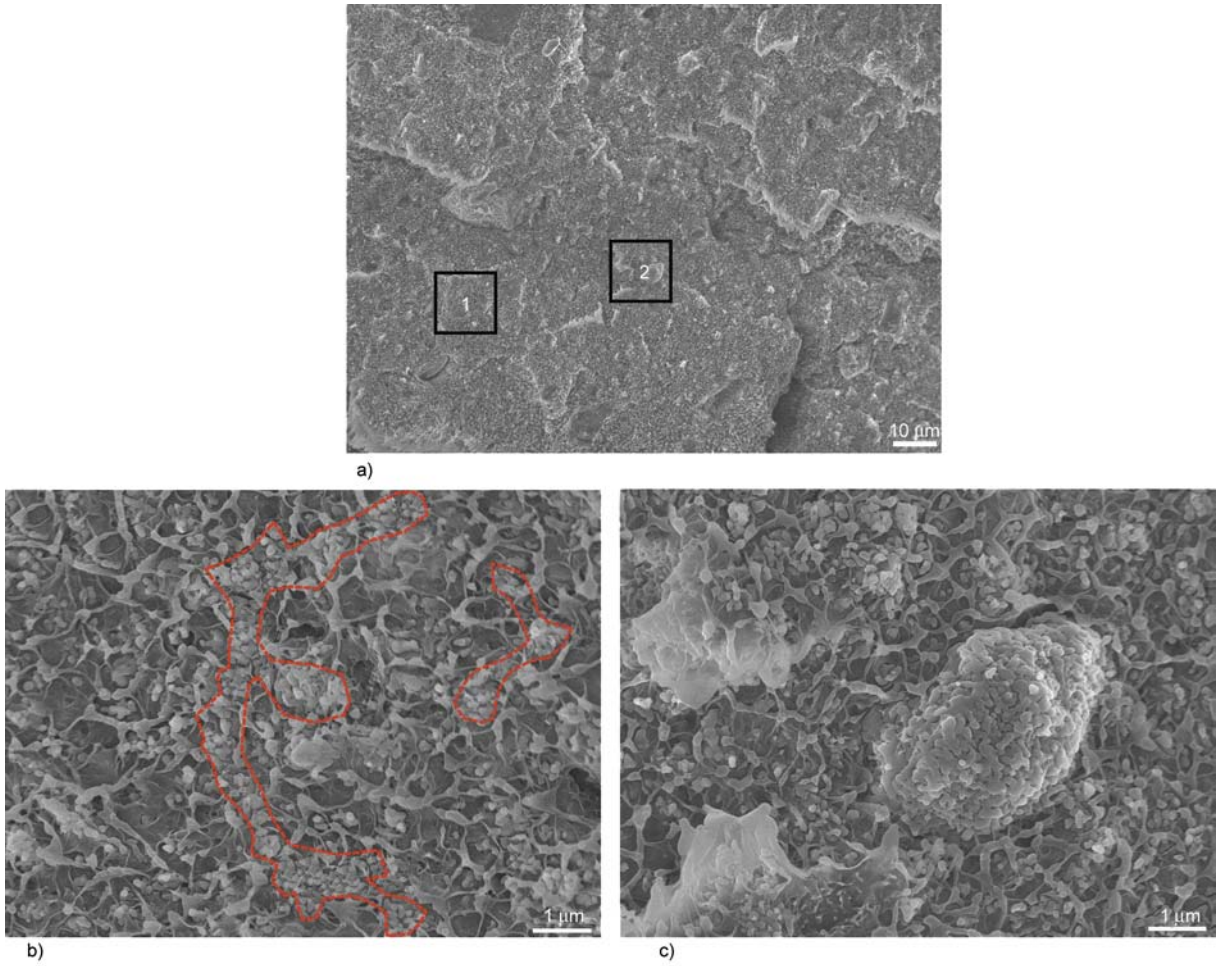

Figure 2. (a) SEM micrographs of the cryogenically fractured surface of A0.1/HDPE (30 vol%); (b) manified image of part (1) in (a); (c) manified image of part (2) in (a). The percent is referred to the alumina volume fraction in the composites. The red lines are added to emphasize the local network of the samples.

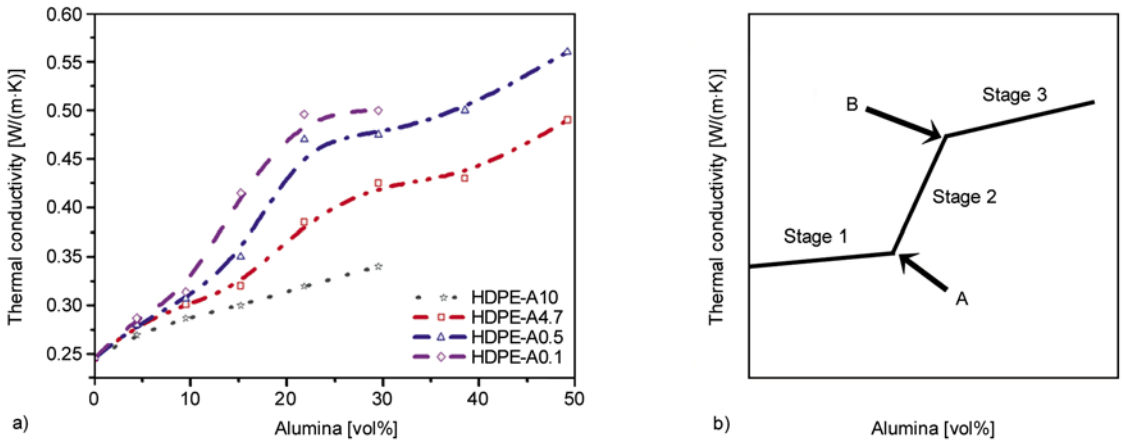

Figure 3. (a) Dependence of thermal conductivity with volume percentage for different particle size in alumina/HDPE composite; (b) Schematic illustration for the three stages of thermal conductivity variation with alumina volume fraction

rial, which can lead to the abrupt increase of the thermal conductivity. The first stage should correspond to the composites, in which most alumina dispersed separately, so the thermal conductivity increases slowly with content. The abrupt increase of conductivity of the second stage indicates the formation of the continuous pathway [29, 30]. The continuous alumina pathway is a network in 3D and the SEM picture is in 2D. Although the abrupt increase of the thermal conductivity indicates the

formation of the alumina pathway, the continuous pathway can't be observed in the SEM pictures [31].

In the second stage, the increase of alumina content increases the number of the alumina pathways, so the rapid increase of the thermal conductivity was continued. After that, further increase of the alumina content has little effect on the increase of the pathway [32], so the increase rate of thermal conductivity slows down, which starts the third stage.

With a given particle content, the smaller the particle size, the higher the composite's thermal conductivity would be. The values of thermal conductivity (K_s) with different particle size at alumina content 30 vol% comply with the following order: K0.1 (0.49 W/(m·K)) > K0.5 (0.47 W/(m·K)) > K4.7 (0.42 W/(m·K)) > K10 (0.37 W/(m·K)). K0.1 and K0.5 at alumina content 30 vol% is about two times of that of HDPE (K_{HDPE} = 0.249 W/(m·K)).

3.3. Mechanical properties of the composite

3.3.1 Impact strength

The variations of impact strength of composite with alumina volume content are shown in Figure 4. The toughening efficiencies of the alumina particles are dramatically different. The Al_2O_3/HDPE compos-

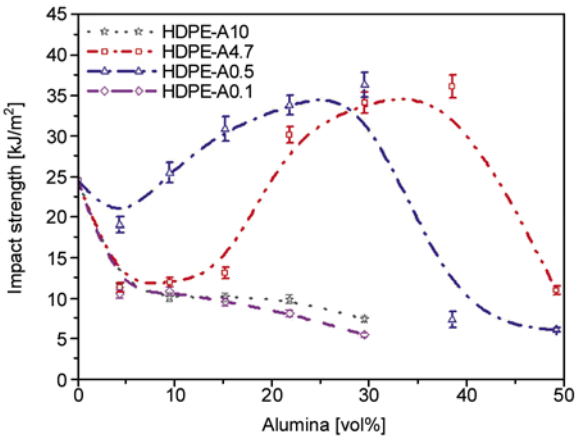

Figure 4. Variations of the composite impact strength with alumina volume fraction

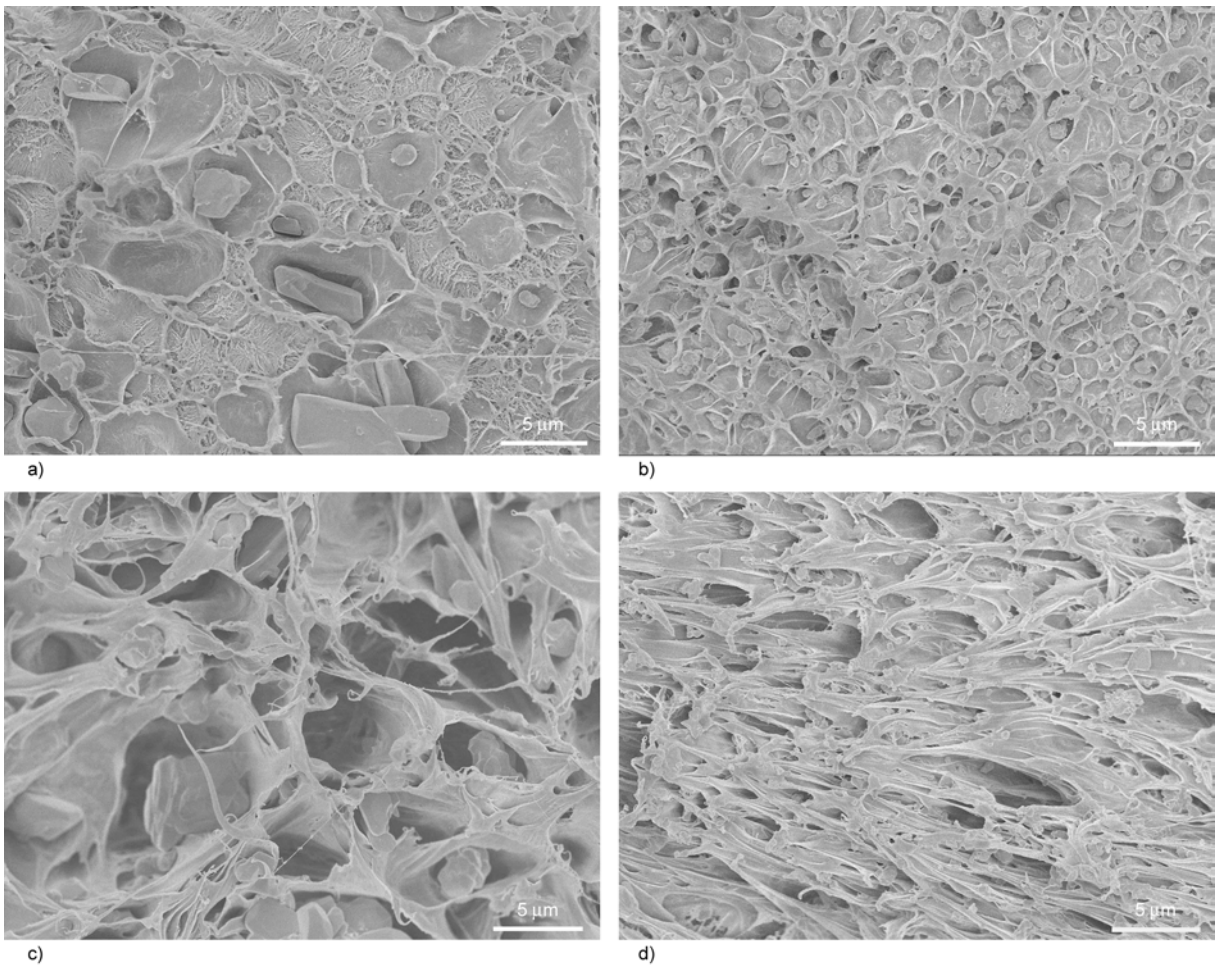

Figure 5. SEM micrographs of the fracture surfaces of Izod samples: (a) A4.7/HDPE (5 vol%); (b) A0.5/HDPE (5 vol%); (c) A4.7/HDPE (30 vol%); (d) A0.5/HDPE (30 vol%); The impact direction was from right to the left. The percents refer as the alumina volume fraction in the composites.

ites can not be toughened by A10 and A0.1 with the content up to 30 vol%. The composites can be toughened by A4.7 and A0.5 when the contents are in the range around 10–30 vol%. The maximum impact strength of A0.5/HDPE is about 36 kJ/m^2, which is 1.44 times of that of the pure HDPE.

There are several mechanisms for toughening of polymer. For the inorganic particles toughening polymer, at least three factors are necessary: inherent ductility of the matrix, weak interphase supporting the filler/matrix debonding and suitable interparticle distance. The stress concentration first leads to debonding of the filler particles and voids formation. The particle content affects the interparticle distance and the stress state of the matrix polymer surrounding the voids [19, 20].

At low alumina content, the interparticle distance is long and the interparticle matrix ligament lies in plane strain state which is hard to yield, as a result the impact strength cannot be improved. When the alumina content increases and the interparticle distance reach a suitable range, the interparticle matrix ligament lies in plane press state, which can be plastic yield easily and the impact strength can be improved. But when the alumina content is too high, the interparticle distance becomes too small and even leads to large size agglomerates, which provide convenient triggers for brittle behavior.

The morphologies of the fracture surfaces of A4.7/HDPE and A0.5/HDPE after impact test are shown in Figure 5. When the alumina content is 5 vol%, the surfaces are generally even and smooth. The plastic yield increases with the increase of filler content or the decrease of particle size as shown in Figure 5c–d. The increase of particle content decreases the average interparticle distance of the matrix and results in the apparently plastic yield, which leads to high impact strength of the composites. Compared to that of A4.7, A0.5 is more efficient in toughening the composite. As shown in Figure 5d, stable fibril structure was formed in the A0.5/HDPE (30 vol%) sample at the particle–polymer interface.

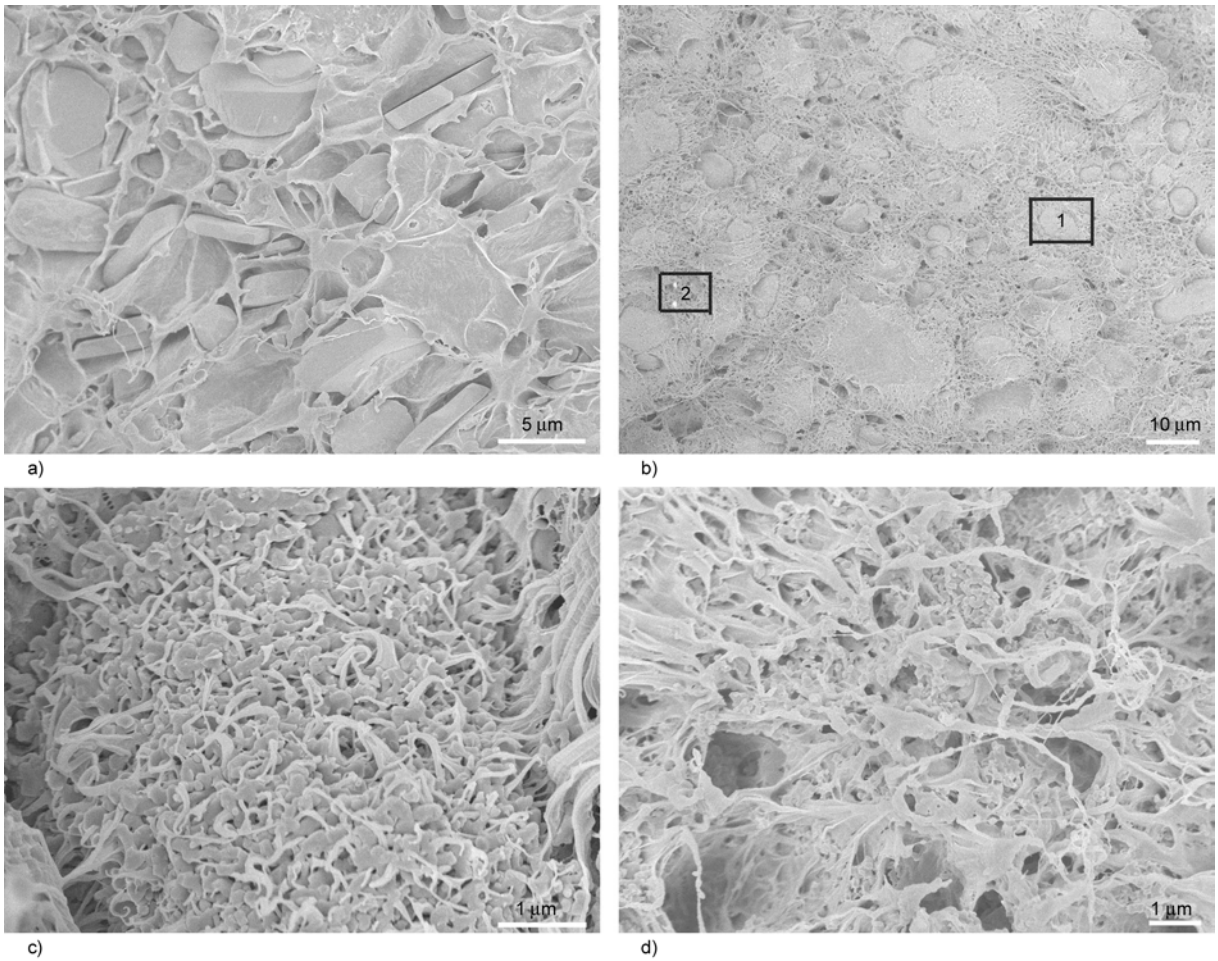

Figure 6. SEM micrographs of the fracture surfaces of Izod samples: (a) A10/HDPE (30 vol%); (b) A0.1/HDPE (30 vol%); (c) magnified image of part (1) in (b); (d) magnified image of part (2) in (b). The percents refer as the alumina volume fraction in the composites.

The SEM micrographs of Figure 6 reveal that the A10, A0.1/HDPE are brittle fractured. Most parts of the fracture surfaces of A10/HDPE are even and smooth, and only a small part of the HDPE at interfaces is microductile. It indicates that because of its size, A10 particles serve as the initiation sites for the brittle fracture of the composite [33].

A0.1 does not toughen the composite efficiently because of the aggregation shown in Figure 6b and Figure 6c. In this case, when the amount of aggregated clusters (Figure 6b, part (1)) is large enough, the fracture mode would be a brittle fracture. Nevertheless, in the Figure 6b, part (2) area without large alumina clusters, the HDPE matrix forms fibrils structure possessing plastic deformation as shown in Figure 6d. The result suggests that if the nano-alumina particles can be uniformly dispersed in matrix they could be used as effective toughening agent.

3.3.2 Tensile strength

The tensile strength of composites increases with the decrease of the alumina particle size (Figure 7). When the A0.1 content is 30 vol%, the tensile strength can be enhanced to 1.12 times of the pure HDPE.

Compared to the thermal conductivity and impact strength, tensile strength is more dependent on the filler-matrix interaction. Strong interaction benefits the tensile stress transfer from matrix to filler, thus reinforces the composite. The interfacial action increases with the decrease of the particle size.

In A0.1/HDPE, the results of the impact and tensile strength seem controversial because the agglomerates play different roles in these loading processes. The agglomerates can bring strong interaction between the matrix and fillers, because some of the matrix is wrapped into it (Figure 6c), which doesn't favor the debonding. Furthermore, the agglomerates provide defects that can develop quickly and trigger brittle fracture. For tensile strength, the interfacial action is favored for the stress transfer from the matrix to the alumina particles, so the tensile strength can be enhanced.

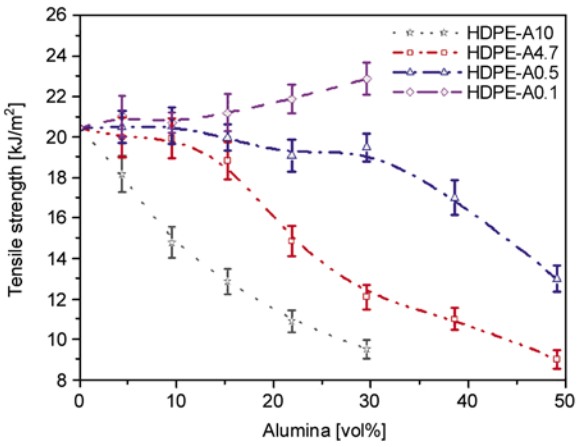

Figure 7. Variations of the composite tensile strength with alumina volume fraction

4. Conclusions

In this study, the thermal conductivity and mechanical properties (impact strength and tensile strength) of 4 types of Al_2O_3/HDPE composites with alumina filler size from 10 μm to 100 nm were investigated. The alumina particle with smaller particle size can form thermal conductive alumina pathway more easily and has higher toughening efficiency for A10, A4.7 and A0.5. However, nano alumina particles can form aggregation and destroy the toughness as that of A0.1/HDPE in this study. In the tensile process, the size of voids decreases with the alumina particle size, thus alumina with smaller particle size can bring higher tensile strength. A0.5/HDPE at alumina content of 25 vol% owns the best integrated thermal conductivity and mechanical properties (impact strength and tensile strength). Its thermal conductivity is nearly two times of the pure HDPE, and the impact strength and tensile strength is 1.44 times and 95% of the pure HDPE respectively. This study would provide practical and theoretical supports for thermal conductive polymer composites with good synthetic properties.

Acknowledgements

The authors gratefully acknowledge financial support by the National High Technology Research and Development Program ('863' Program) of China (2009 AA064005).

References

[1] Zhou W. Y., Qi S. H., Tu C. C., Zhao H. Z.: Novel heat-conductive composite silicone rubber. Journal of Applied Polymer Science, **104**, 2478–2483 (2007). DOI: 10.1002/app.25479

[2] Yu S. Z., Hing P., Hu X.: Thermal conductivity of polystyrene-aluminum nitride composite. Composites Part A: Applied Science and Manufacturing, **33**, 289–292 (2002). DOI: 10.1016/S1359-835X(01)00107-5

[3] Lee G-W., Park M., Kim J., Lee J. I., Yoon H. G.: Enhanced thermal conductivity of polymer composites filled with hybrid filler. Composites part A: Applied Science and Manufacturing, **37**, 727–734 (2006). DOI: 10.1016/j.compositesa.2005.07.006

[4] Weidenfeller B., Höfer M., Schilling F. R.: Thermal conductivity, thermal diffusivity, and specific heat capacity of particle filled polypropylene. Composites Part A: Applied Science and Manufacturing, **35**, 423–429 (2004). DOI: 10.1016/j.compositesa.2003.11.005

[5] Choy C. L., Luk W. H., Chen F. C.: Thermal conductivity of highly oriented polyethylene. Polymer, **19**, 155–162 (1978). DOI: 10.1016/0032-3861(78)90032-0

[6] Bujard P.: Thermal conductivity of boron nitride filled epoxy resins: Temperature dependence and influence of sample preparation. in 'Proceedings of the I-THERM, Los Angeles, USA' 41–49 (1988).

[7] Zhou W. Y., Qi S. H., An Q. L., Zhao H. Z., Liu N. L.: Thermal conductivity of boron nitride reinforced polyethylene composites. Materials Research Bulletin, **42**, 1863–1873 (2007). DOI: 10.1016/j.materresbull.2006.11.047

[8] He H., Fu R., Shen Y., Han Y. C., Song X. F.: Preparation and properties of Si_3N_4/PS composites used for electronic packaging. Composites Science and Technology, **67**, 2493–2499 (2007). DOI: 10.1016/j.compscitech.2006.12.014

[9] Riley F. L.: Silicon nitride and related materials. Journal of the American Ceramic Society, **83**, 245–265 (2000). DOI: 10.1111/j.1151-2916.2000.tb01182.x

[10] Bujard P., Kuhnlein G., Ino S., Shiobara T.: Thermal conductivity of molding compounds for plastic packaging. IEEE Transactions on Components, Packaging and Manufacturing Technology Part A, **17**, 527–532 (1994). DOI: 10.1109/ECTC.1994.367636

[11] Procter P., Solc J.: Improved thermal conductivity in microelectronic encapsulants. IEEE Transactions on Components, Hybrids, and Manufacturing Technology, **14**, 835–842 (1991). DOI: 10.1109/ECTC.1991.163976

[12] Gonon P., Sylvestre A., Teysseyre J., Prior C.: Dielectric properties of epoxy/silica composites used for microlectronic packaging, and their dependence on post-curing. Journal of Materials Science-Materials in Electronics, **12**, 81–86 (2001). DOI: 10.1023/A:1011241818209

[13] Xu Y., Chung D. D. L., Mroz C.: Thermally conducting aluminum nitride polymer-matrix composites. Composites Part A: Applied Science and Manufacturing, **32**, 1749–1757 (2001). DOI: 10.1016/S1359-835X(01)00023-9

[14] Lu X., Xu G.: Thermally conductive polymer composites for electronic packaging. Journal of Applied Polymer Science, **65**, 2733–2738 (1997). DOI: 10.1002/(SICI)1097-4628(19970926)65:13<2733::AID-APP15>3.0.CO;2-Y

[15] Boudenne A., Ibos L., Fois M., Majesté J. C., Gehin E.: Electrical and thermal behavior of polypropylene filled with copper particles. Composites Part A: Applied Science and Manufacturing, **36**, 1545–1554 (2005). DOI: 10.1016/j.compositesa.2005.02.005

[16] Zhou W. Y., Qi S. H., Tu C. C., Zhao H. Z., Wang C. F., Kou J. L.: Effect of the particle size of Al_2O_3 on the properties of filled heat-conductive silicone rubber. Journal of Applied Polymer Science, **104**, 1312–1318 (2007). DOI: 10.1002/app.25789

[17] King J. A., Keith J. M., Glenn O. L., Miskioglu I., Cole A. J., McLaughlin S. R., Pagel R. M.: Synergistic effects of carbon fillers on tensile and flexural properties in liquid-crystal polymer based resins. Journal of Applied Polymer Science, **108**, 1657–1666 (2008). DOI: 10.1002/app.27752

[18] Zhou W. Y., Wang C. F., Ai T., Wu K., Zhao F. J., Gu H. Z.: A novel fiber-reinforced polyethylene composite with added silicon nitride particles for enhanced thermal conductivity. Composites Part A: Applied Science and Manufacturing, **40**, 830–836 (2009). DOI: 10.1016/j.compositesa.2009.04.005

[19] Wu S. H.: A generalized criterion for rubber toughening: The critical matrix ligament thickness. Journal of Applied Polymer Science, **35**, 549–561 (1988). DOI: 10.1002/app.1988.070350220

[20] Bartczak Z., Argon A. S., Cohen R. E., Weinberg M.: Toughness mechanism in semi-crystalline polymer blends: II. High-density polyethylene toughened with calcium carbonate filler particles. Polymer, **40**, 2347–2365 (1999). DOI: 10.1016/S0032-3861(98)00444-3

[21] Voet A.: Temperature effect of electrical resistivity of carbon black filled polymers. Rubber Chemistry and Technology, **54**, 42–50 (1981).

[22] Foulger S. H.: Electrical properties of composites in the vicinity of the percolation threshold. Journal of Applied Polymer Science, **72**, 1573–1582 (1999). DOI: 10.1002/(SICI)1097-4628(19990620)72:12<1573::AID-APP10>3.0.CO;2-6

[23] Ling W., Gu A. J., Liang G. Z., Yuan L.: New composites with high thermal conductivity and low dielectric constant for microelectronic packaging. Polymer Composites, **31**, 307–313 (2010). DOI: 10.1002/pc.20805

[24] Kim G-M., Michler G. H.: Micromechanical deformation processes in toughened and particle-filled semicrystalline polymers: Part 1. Characterization of deformation processes in dependence on phase morphology. Polymer, **39**, 5689–5697 (1998). DOI: 10.1016/S0032-3861(98)00089-5

[25] Kim G-M., Michler G. H.: Micromechanical deformation processes in toughened and particle filled semicrystalline polymers: Part 2. Model representation for micromechanical deformation processes. Polymer, **39**, 5699–5703 (1998).
DOI: 10.1016/S0032-3861(98)00169-4

[26] Wu S. H.: Phase structure and adhesion in polymer blends: A criterion for rubber toughening. Polymer, **26**, 1855–1863 (1985).
DOI: 10.1016/0032-3861(85)90015-1

[27] Khumalo V. M., Karger-Kocsis J., Thoman R.: Polyethylene/synthetic boehmite alumina nanocomposites: Structure, thermal and rheological properties. Express Polymer Letters, **5**, 264–274 (2010).
DOI: 10.3144/expresspolymlett.2010.34

[28] Khumalo V. M., Karger-Kocsis J., Thoman R.: Polyethylene/synthetic boehmite alumina nanocomposites: Structure, mechanical, and perforation impact properties. Journal of Materials Science, **46**, 422–428 (2011).
DOI: 10.1007/s10853-010-4882-9

[29] Karásek L., Sumita M.: Characterization of dispersion state of filler and polymer-filler interactions in rubber-carbon black composites. Journal of Materials Science, **31**, 281–289 (1996).
DOI: 10.1007/BF01139141

[30] El-Tantawy F.: New double negative and positive temperature coefficients of conductive EPDM rubber TiC ceramic composites. European Polymer Journal, **38**, 567–577 (2002).
DOI: 10.1016/S0014-3057(01)00208-7

[31] Ng H. Y., Lu X. H., Lau S. K.: Thermal conductivity of boron nitride-filled thermoplastics: Effect of filler characteristics and composite processing conditions. Polymer Composites, **26**, 778–790 (2005).
DOI: 10.1002/pc.20151

[32] Nielsen L. E.: Polymeric composite systems with two continuous phases. Journal of Applied Polymer Science, **21**, 1579–1584 (1977).
DOI: 10.1002/app.1977.070210613

[33] Zuiderduin W. C. J., Westzaan C., Huétink J., Gaymans R. J.: Toughening of polypropylene with calcium carbonate particles. Polymer, **44**, 261–275 (2003).
DOI: 10.1016/S0032-3861(02)00769-3

[34] Marshall G. P.: Design for toughness in polymers. Part. 1: Fracture mechanics. Plastics and Rubber Processing and Applications, **2**, 169–182 (1982).

eXPRESS Polymer Letters Vol.5, No.7 (2011) 591–603
Available online at www.expresspolymlett.com
DOI: 10.3144/expresspolymlett.2011.58

Enhancement of mechanical properties of poly(vinyl chloride) with polymethyl methacrylate-grafted halloysite nanotube

C. Liu[1], Y. F. Luo[1], Z. X. Jia[1], B. C. Zhong[1], S. Q. Li[2], B. C. Guo[1], D. M. Jia[1]*

[1]College of Materials Sci. and Eng., South China University of Technology, Guangzhou 510640, PR China
[2]XinJiang Tianye Group Co., Ltd., Xinjiang, Shihezi 832014, PR China

Received 13 November 2010; accepted in revised form 10 January 2011

Abstract. Halloysite nanotubes(HNTs) grafted with Polymethyl methacrylate(PMMA) were synthesized via radical polymerization. The properties of PMMA-grafted HNTs were characterized by transmission electron microscopy (TEM), fourier transform infrared spectroscopy (FTIR), thermogravimetric analysis (TGA) and X-ray photoelectron spectroscopy (XPS). The results showed that PMMA grafted to the surfaces of HNTs successfully. Then, PVC/PMMA-grafted HNTs nanocomposites were prepared by melt compounding. The morphology, mechanical properties and thermal properties of the nanocomposites were investigated. PMMA-grafted HNTs can effectively improve the toughness, strength and modulus of PVC. The glass transition and thermal decomposition temperatures of PVC phase in PVC/PMMA-grafted HNTs nanocomposites are shifted toward slightly higher temperatures. The grafted HNTs were uniformly dispersed in PVC matrix as revealed by TEM photos. The fracture surfaces of the nanocomposites exhibited plastic deformation feature indicating ductile fracture behaviors. The improvement of toughness of PVC by PMMA-grafted HNTs was attributed to the improved interfacial bonding by grafting and the toughening mechanism was explained according to the cavitation mechanism.

Keywords: *nanocomposites, halloysite nanotubes, poly(vinyl chloride), surface modification, polymethyl methacrylate*

1. Introduction

Poly(vinyl chloride) (PVC) is an important commercial thermoplastic, which is widely used in industrial fields due to its good properties and low-cost. However, its brittleness, low thermal stability and poor processability limit its application. Incorporation of nanopaticles into PVC to form nanocomposite is an effective method for improving the mechanical and thermal properties of PVC. For example, the addition of organic montmorillonite (MMT) within 0.5–3 wt% content can enhance the mechanical properties and improve the processing stability of the PVC/MMT nanocomposites [1]. Calcium carbonate ($CaCO_3$) nanoparticles stiffen and toughen PVC simultaneously in PVC/$CaCO_3$ nanocomposites which were synthesized by in situ polymerization [2]. Wang *et al.* [3] prepared PVC composites with poly caprolactone (PCL) modified multiwall carbon nanotube (MWNT) and found that MWNT-PCL can increase the Young's modulus, tensile strength and roughness of PVC.

Due to the strong interactions among the nanoparticles, uniformly dispersion of them in polymers is hard to achieve. Numerous methods have been employed to improve the dispersion of nanoparticles in polymer matrix. Surface modification of the nanoparticle via grafting is one of the most common methods for increasing the compatibility

*Corresponding author, e-mail: zxjia@scut.edu.cn

between nanoparicles and polymers. The interfacial bonding between the nanoparticles and the matrix can be enhanced by improved miscibility and entanglement of the grafting polymers with the matrix macromolecules. The modified nanoparticles can be uniformly dispersed in polymer matrix. Xie *et al*. [4] treated the nano-sized antimony trioxide (Sb_2O_3) particles by *in-situ* methyl methacrylate (MMA)/ Sb_2O_3 polymerization and then prepared PVC/Sb_2O_3 nanocomposites. They found that modified Sb_2O_3 could effectively reinforce and toughen PVC due to the improved interfacial bonding. Nanosilica and talc can also be grafted by PMMA for the purposed of toughening PVC [5, 6].

Halloysite nanotubes (HNTs) are a type of natural aluminoslicate nanotube and can be used as nanofiller for polymers, such as polypropylene [7, 8], epoxy resin[9-11], polyethylene [12], polyamide [13, 14] and rubber [15–17]. Due to their unique structure, HNTs show promising reinforcing effect for polymers. For example, the strength and modulus of polymers can be significantly improved by HNTs. HNTs can also enhance the thermal stability of polymers. Recently, Mondragon *et al*. [18] found that HNTs could increase the elongation of PVC indicating their toughening effect for PVC. In virtue of the poor compatibility between HNTs and PVC, surface treatment of HNTs before adding them to PVC is necessary.

Recently, the modification of HNTs has attracted great attention of scientists [19, 20]. In this study, HNTs grafted with polymethyl methacrylate (PMMA), a polar polymer which has been proved with excellent compatibility with PVC, have been prepared. Then the grafted HNTs were compounded with PVC for preparing PVC/PMMA-grafted HNTs nanocomposites. The surface properties of HNTs before and after grafting were characterized. The morphology, mechanical properties and thermal properties of the nanocomposites have been investigated in detail. It is expected that the improved interfacial bonding by grafting may significantly enhance the mechanical properties of the nanocomposites.

2. Experimental

2.1. Materials

Halloysite nanotubes (HNTs), collected from Hubei Province, China, were purified according to the reported method [11]. PVC (SG-5) with an average polymerization degree between 981 and 1135 was a powder product offered by Wuhai Chemical Co., Ltd, China. Rare earth complex heat stabilizer (WWP-C) was supplied by Guangdong Winner Functional Materials Co. Ltd., China. Di(2-ethylhexyl) phthalate (DOP), chemically pure grade, was supplied by Tianjing Damao Chemical Reagent Factory, China. Methyl methacrylate (MMA), chemically pure grade, was produced by Tianjin Damao Chemical Reagent Factory, China. MMA was distilled under reduced pressure before being used to remove the inhibitor. 3-(Trimethoxysilyl)-propyl methacrylate (MPS), chemically pure grade, was produced by Nanjing Shuguang Chemical group Co., Ltd. Sodium dodecyl sulfate (SDS), analytical reagent, was produced by Tianjin Qilun tech Co., Ltd. Potassium persulfate (KPS) analytical reagent, was produced by Tianjin Fuchen Chemical Reagent Factory, China. Deionized water was applied for all polymerization and treatment processes.

2.2. Preparation of PMMA-grafted HNTs

HNTs were firstly modified by MPS coupling agent. The required volumes of MPS were added into the toluene dispersions containing HNTs at 110ºC under stirring and agitate for 10 h. After drying at 50°C under vacuum for 24 h, the MPS-functionalized HNTs were extracted by a Soxhlet extractor for 12 h with toluene. The product was finally dried at 50°C under vacuum condition for 24 h. The amount of MPS grafted on HNTs surfaces was evaluated by thermal gravimetric analysis (TGA).

The polymerization of MMA in the presence of MPS-functionalized HNTs was carried out in a four necked flask equipped with a reflux condenser, a stirrer, a thermometer and nitrogen inlet. First, the functionalized HNTs were dispersed in water containing SDS ultrasonically, and then heated under constant stirring with protection of nitrogen flow. When the temperature reached around 80°C, the aqueous solution of initiator KPS was added. After 10 min, a continuous dosage of 10 wt% MMA (based on HNTs) was added and reacted at 80°C for 3 hour. The polymerization products were extracted with chloroform for 24 h in a Soxhlet apparatus to remove the ungrafted polymer after emulsion breakage and purification process. The obtained PMMA-grafted HNTs were dried at 50°C to a constant weight under vacuum.

2.3. Preparation of PVC/PMMA-grafted HNTs nanocomposites

The PVC nanocomposites were formulated with 5 phr heat stabilizer and 5 phr of DOP, as well as various contents of PMMA-grafted HNTs. The ingredients were first mixed in a high-speed rotating mixer and then plasticized by a two-roll mill at 175°C for 8 min. The compounds were then compression molded to plates at 175°C for 5 min with a 5 min preheating period. Specimens of suitable dimensions for mechanical testing were cut from the compression molded plates.

2.4. Characterization

Fourier Transform Infrared Spectroscopy (FTIR)

A Bruker Vector 33 FTIR spectrometer (Germany) was used for FTIR analysis. The infrared spectra were recorded in absorbance units in the 4000–400 cm^{-1} range. FTIR spectra were measured in KBr pellets containing 1% finely ground samples.

X-ray Photoelectron Spectroscopy (XPS)

XPS analyses were performed using a Kratos Axis Ultra (DLD) (England) with an aluminum (mono) K_α source (1486.6 eV).

Thermogravimetric Analysis (TGA)

TGA was conducted under nitrogen atmosphere with Netzsch TG 209 F1(Germany) at a heating rate of 10°C/min from 30°C to 700°C.

The grafting percentage onto the surface of HNTs was calculated from the TGA analysis by the Equation (1):

$$\text{Percentage of grafting}\,[\%] = \frac{\text{Polymer grafted}\,[g]}{\text{HNTs used}\,[g]} \cdot 100 \quad (1)$$

Mechanical properties

Zwick/Roell Z010 and Zwick pendulum 5113 testing machines (Germany) were used to perform the tensile, flexural and impact testing according to ISO 527:1993, ISO 178:1993 and ISO 180:1993, respectively.

Scanning Electron Microscopy (SEM)

The fracture surfaces of impact samples were coated with a thin layer of gold before any observations. The fracture surface was then examined by Nova Nano SEM 430 machine (FEI, Netherlands). The voltage of the electron beam used for SEM observation was 10 kV.

Transmission Electron Microscope (TEM)

The morphologies of HNTs and nanocomposites were characterized with a Philip Tecnai 12 TEM (Eindhoven, Netherlands). The TEM samples of the nanocomposites were cut into thin pieces of about 120 nm in thickness with an ultramicrotome (EMUC6, Leica, Germany) before observation.

Dynamic Mechanical Analysis (DMA)

DMA was conducted with a EPLEXOR dynamic mechanical analyzer (Gabo Qualimeter Testanlagen GmbH; Ahlden, Germany) at an oscillation frequency of 1.0 Hz. The temperature range was from 30 to 150°C with a heating rate of 3°C/min.

Differential Scanning Calorimetry (DSC)

The glass transition temperature (T_g) was evaluated by using DSC method with a NETZSCH Instruments DSC 204 F1 (Germany), operated in nitrogen at a rate of 10 C /min.

3. Results and discussion

3.1. Properties of PMMA-grafted HNTs

As shown in TEM images (Figures 1a and b), the HNTs used in this study exhibit mainly tubular shapes with an outer diameter of 20~50 nm. The hollow lumen of the HNTs is clearly visible in Figure 1b. TEM images of PMMA-grafted HNTs are shown in Figures 1c and d. It can be seen that the surface of the PMMA-grafted HNTs is rougher than that of pristine HNTs. Some irregular precipitate is found on the outer surface of the PMMA-grafted HNTs. A part of hollow lumen of HNTs is filled after grafting. This indicates that a layer of PMMA is wrapped on the outer-surface and inner-surface of HNTs.

Figure 2 shows FTIR spectra of the pristine HNTs, MPS-functionalized HNTs and PMMA-grafted HNTs. Compared to the spectrum of HNTs, the most significant feature of MPS-HNTs is the presence of characteristic band at 2950, 1720 and 1640 cm^{-1} which is ascribed to the C–H stretching vibration, C=O symmetric stretching vibration, and –C=C vibration of MPS respectively. This indicates that the MPS grafts on the surface of HNTs successfully. For the spectrum of PMMA-grafted HNTs, the peak around 1732 cm^{-1} is ascribed to the C=O vibration of PMMA. As the samples have been extracted, the physically absorbed MPS and PMMA have been removed. Therefore, PMMA are covalently bonded on the surfaces of HNTs through graft

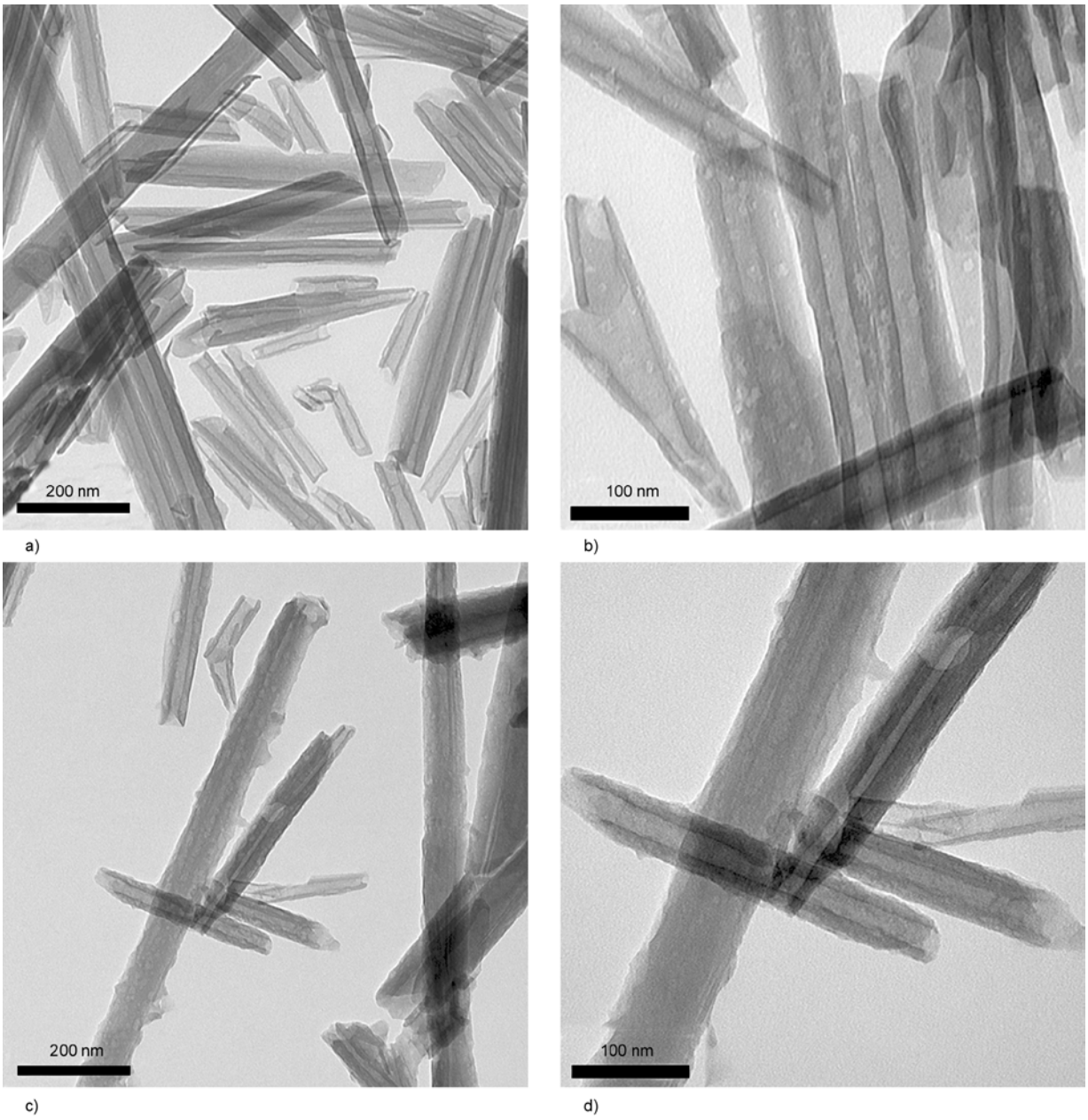

Figure 1. TEM photographs of HNTs and PMMA-grafted HNTs. (a) and (b) HNTs; (c) and (d) PMMA-grafted HNTs

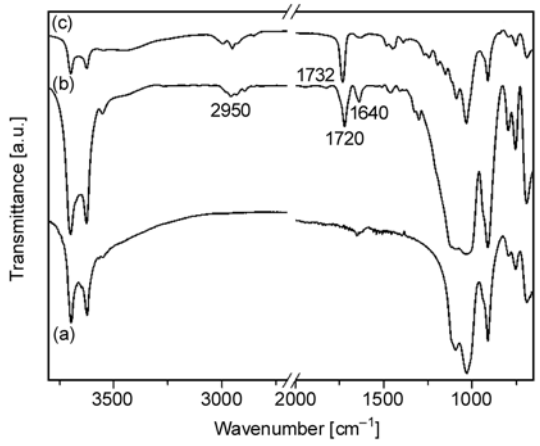

Figure 2. FT-IR spectra of HNTs and modified HNTs. (a) HNTs; (b) MPS-modified HNTs (c) PMMA-grafted HNTs

polymerization. The content of PMMA bonded on the HNTs particles is 5.45 wt %, as calculated from TGA.

Surface element analysis of XPS survey can give the detailed variations of element information on the particles surface qualitatively. The low-resolution XPS survey spectra of the HNTs and PMMA-grafted HNTs are shown in Figure 3. As illustrated in Figure 3a, XPS survey spectrum of HNTs shows the oxygen peak at 531 eV, carbon peak at 284 eV, silicon peak at 102 eV and aluminum peak at 73 eV [21]. Table 1 summarizes the characteristic XPS data. It can be seen that the detected relative con-

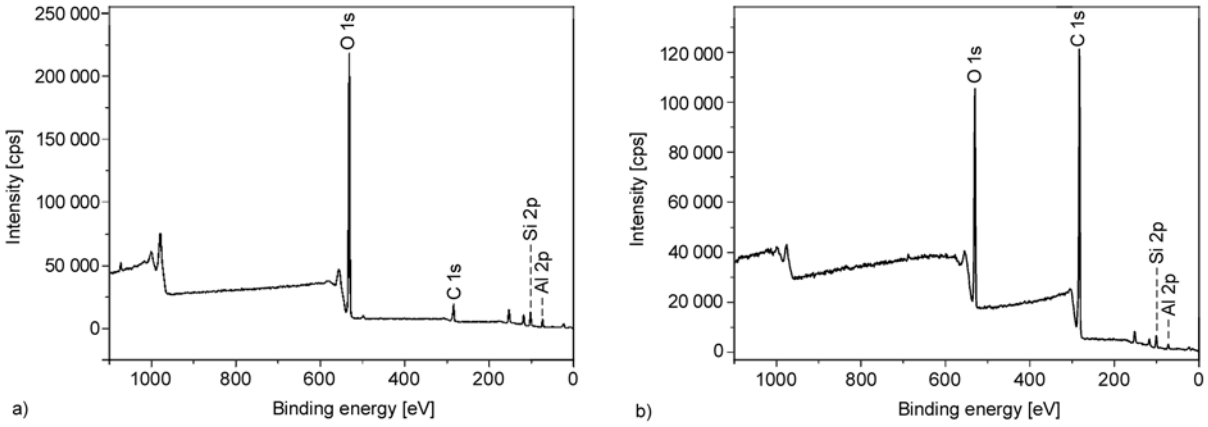

Figure 3. XPS spectra of HNTs (a) and PMMA-grafted HNTs (b)

Table 1. XPS atomic content [%] for the HNTs and PMMA-grafted HNTs

Atom	HNTs	PMMA-grafted HNTs
C	15.30	63.82
O	54.33	22.07
Al	13.72	5.78
Si	16.66	8.34

centration of carbon of PMMA-grafted HNTs is remarkably increased compared with that of HNTs. The relative concentrations of oxygen, aluminum and silicon are decreased. The result can be explained by the fact that grafting of PMMA introduces abundant carbon atoms onto the surfaces of HNTs. This result is consistent with the previous reported of silane modified HNTs [22]. The above XPS results also verify the successful modification of HNTs.

3.2. Morphology of PVC/PMMA-grafted HNTs nanocomposites

Dispersion of the fillers is one of the most critical issues in determining the mechanical properties of nanocomposites [23]. The agglomerated fillers in the polymer matrix may act as the stress-concentration points, leading to deteriorated properties [24]. The dispersion of the PMMA-grafted HNTs in the matrix was evaluated using TEM (Figure 4). For the nanocomposites with 1 phr PMMA-grafted HNTs (Figures 4a and b), a good dispersion is achieved. HNTs dissociate into isolated nanotubes, and no visible particle agglomerates are observed, indicating good compatibility between the grafted HNTs and PVC. Only a small amount of agglomerates are found in the nanocomposite with 5 phr PMMA-grafted HNTs (Figures 4c and d).

The morphology of the fracture surfaces for PVC and PVC/PMMA-grafted HNTs nanocomposites were determined by SEM. It can be seen that the fractured surface of the PVC (Figure 5a) is relatively smooth, showing brittle failure characteristics. In contrast, the fractured surfaces of the nanocomposite (Figures 5b, c and d) are uneven and consist of a large number of squamous structures, exhibiting plastic deformation characteristics. The overall size of the plastic deformation zone is related to the fracture toughness [25, 26]. The SEM results indicate that the nanocomposites have higher toughness than pristine PVC.

3.3. Dynamic mechanical properties of PVC/PMMA-grafted HNTs nanocomposites

Dynamic mechanical analysis can be used to evaluate material stiffness at various temperatures. It is particularly useful in the characterization of materials used in applications above room temperature [27]. The variation of the storage modulus (E') with temperature for PVC and PVC/PMMA-grafted HNTs nanocomposites are shown in Figure 6. The storage moduli of all of the PVC/PMMA-grafted HNTs nanocomposites are higher than those of PVC below the glass transition temperature (T_g). However, when the nanoparticle content is 5 phr, the storage modulus is progressively reduced with increasing temperature. It is known that the relative values of storage modulus of particulate-filled polymer composites are related to the stiffness and influenced by the effective interfacial interaction between the inorganic particles and polymer chains [5, 28, 29]. In general, the stronger effective interfa-

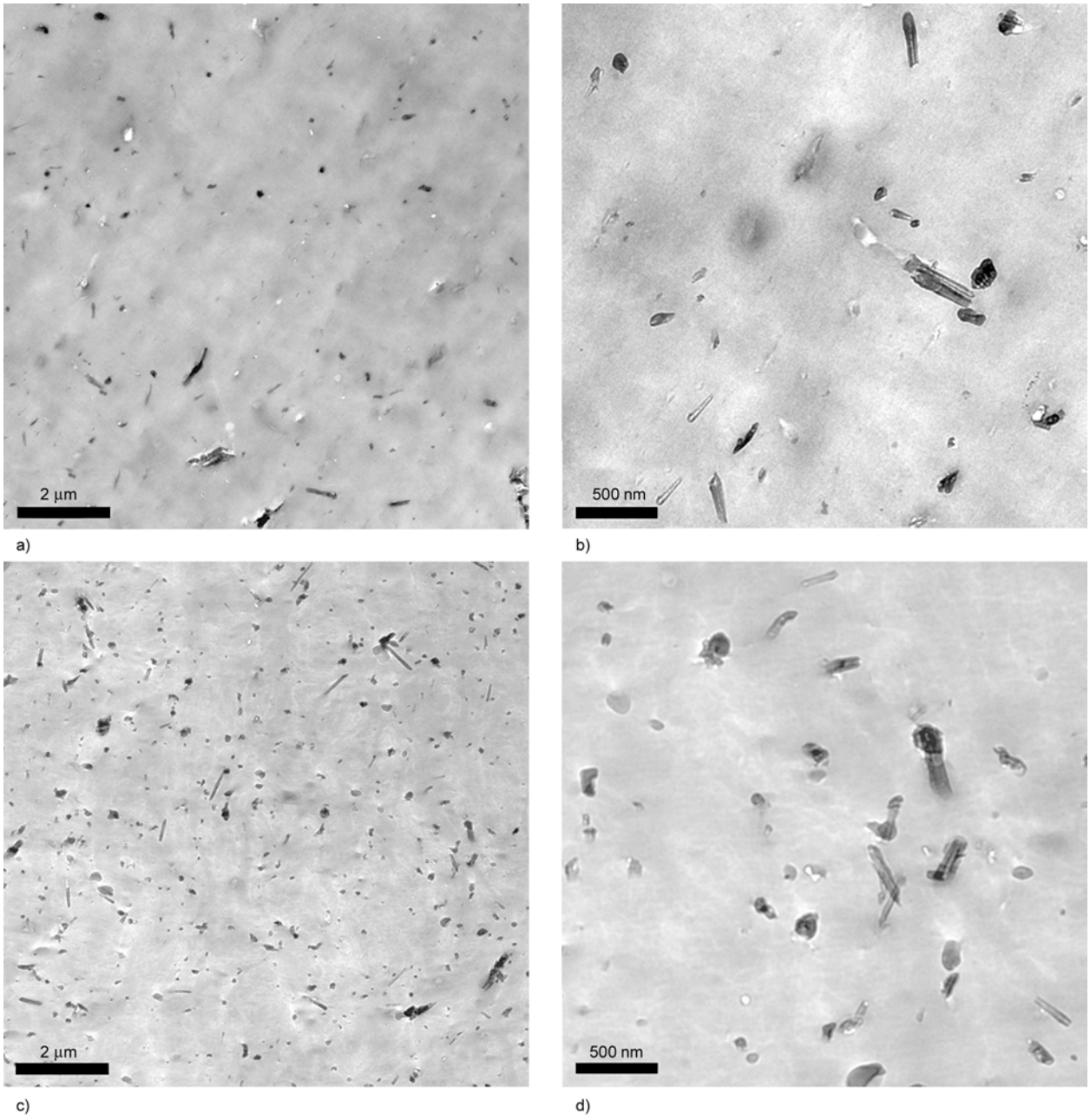

Figure 4. TEM photographs of PVC/PMMA-grafted HNTs nanocomposites. (a) and (b) PVC/PMMA-grafted HNTs (100/1); (c) and (d) PVC/PMMA-grafted HNTs (100/5)

cial interaction between the matrix and the fillers is, the higher value of storage modulus of composites is [30]. The result indicates that PMMA-grafted HNTs can increase the stiffness of PVC. This is attributed to the following facts that there is strong effective interfacial interaction between the PVC matrix and PMMA-grafted HNTs while the well-dispersed PMMA-grafted HNTs reduce mobility of PVC chains. When the nanoparticle content is 5 phr, agglomeration of PMMA-grafted HNTs weakens the interaction between PVC chains and nanoparticles so that the storage modulus decreases a little.

3.4. Thermal properties of PVC/PMMA-grafted HNTs nanocomposites

The influence of PMMA-grafted HNTs on the mobility of the PVC chains was further investigated by the DSC method for comparing the glass transition temperature (T_g). The glass transition temperatures (T_g) of the PVC phases in pristine PVC and PVC/PMMA-grafted HNTs nanocomposites are listed in Table 2. The T_g of PVC in nanocomposites tends to shift slightly towards to higher temperature than that of pristine PVC, indicating the change in

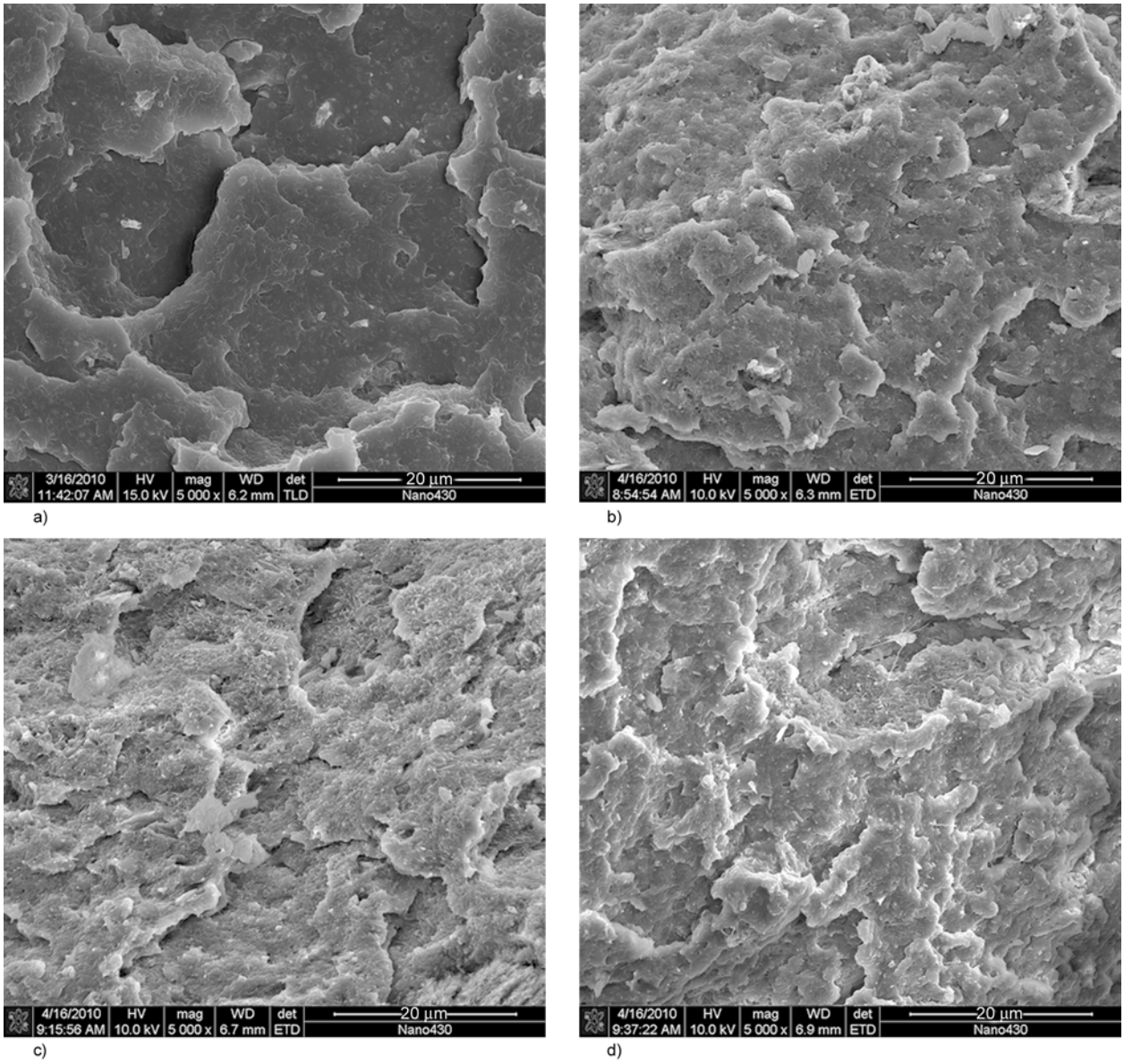

Figure 5. SEM micrographs of the impact fracture surfaces of PVC and PVC/PMMA-grafted HNTs nanpcomposites. (a) PVC; (b) PVC/PMMA-grafted HNTs (100/1); (c) PVC/PMMA-grafted HNTs (100/3); (d) PVC/PMMA-grafted HNTs (100/5)

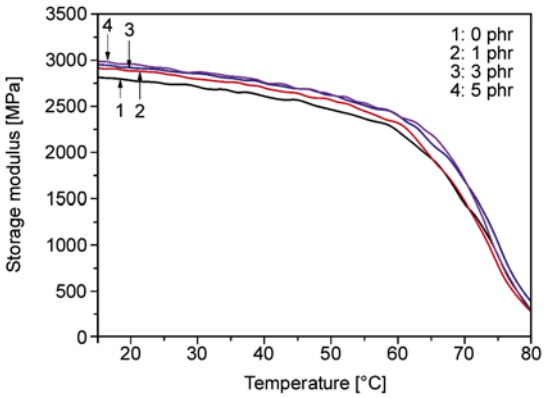

Figure 6. Storage modulus (E') versus temperature for PVC and PVC/ PMMA-grafted HNTs nanpcomposites

Table 2. DSC and TGA results of PVC and PVC/PMMA-grafted HNTs nanocomposites

Sample	T_g [°C]	$T_{5\%}$ [°C]	$T_{50\%}$ [°C]	T_{max} [°C]
Pristine PVC	66	234	290	263
PVC/PMMA-grafted HNTs (100/1)	71	236	291	265
PVC/PMMA-grafted HNTs (100/3)	72	239	295	267
PVC/PMMA-grafted HNTs (100/5)	73	237	295	266

the polymer thermodynamics. The T_g of PVC increases to 73 from 66°C by adding 5 phr of PMMA-grafted HNTs. This behavior is similar to what is observed in PVC/Sb_2O_3 nanocomposites [4]. The PMMA shell on particles increases the

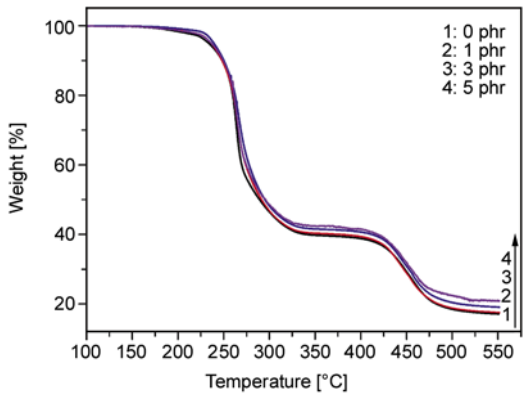

Figure 7. TGA curves of PVC and PVC/PMMA-grafted HNTs nanocomposites in nitrogen

interaction between the particles and PVC matrix and the particles restrain the thermal motion of PVC molecular chains, these lead to the enhancement of thermal stability of PVC.

The thermogravimetric (TG) curves of PVC and PVC/PMMA-grafted HNTs nanocomposites are presented in Figure 7. The first degradation stage which is observed in the temperature range of 250–400°C is assigned to the progressive dehydrochlorination of PVC and the formation of conjugated polyene structure [31]. The temperatures of onset decomposition (the 5% weight loss temperature, $T_{5\%}$), 50% weight loss ($T_{50\%}$), and fastest degradation (T_{max}, which is defined as the peak on the derivation of the TG curve) are summarized in Table 2. It can be seen that the $T_{5\%}$, $T_{50\%}$ and T_{max} of PVC/PMMA-grafted HNTs nanocomposites are slightly higher than that of pristine PVC. The well dispersed HNTs restrict the long-range-chain mobility of PVC and they can act as a barrier to hinder the permeability of volatile degradation products out of the material. These lead to the increase of the thermal stability of PVC. It seems that different nanoparticles have varied effect on the thermal stability of PVC. For example, the addition of $CaCO_3$ can also lead to the slightly increased thermal stability of PVC, which is consistent with the present result [2]. But for the PVC/MMT nanocomposites prepared by in-situ polymerization, the onset decomposition temperatures of the PVC decreased by MMT, while the most rapid decomposition temperatures are enhanced [32]. From TGA result, it can be concluded that PVC/PMMA-grafted nanocomposites have good thermal stability.

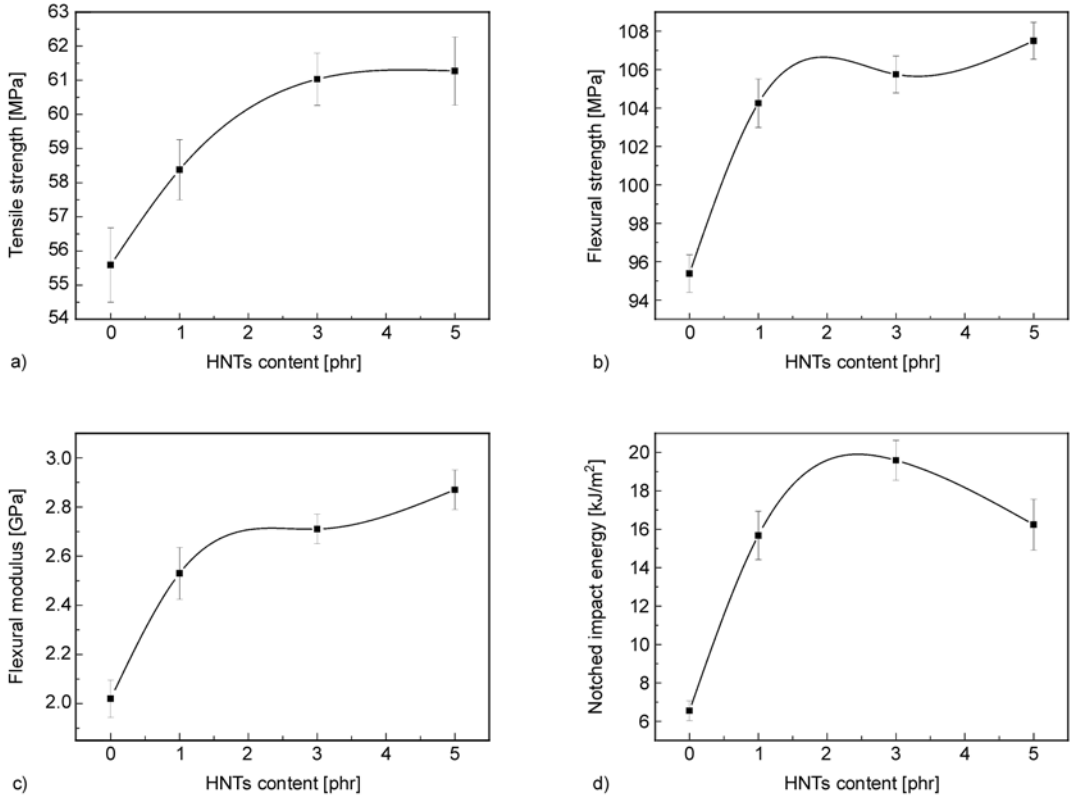

Figure 8. Effects of PMMA-grafted HNTs content on the mechanical properties of PVC/PMMA-grafted HNTs nanocomposites. (a) Tensile strength; (b) flexural strength; (c) flexural modulus; (d) Izod impact strength

3.5. Mechanical properties of PVC/PMMA-grafted HNTs nanocomposites

The mechanical properties of PVC/PMMA-grafted HNTs nanocomposites at different contents of PMMA-grafted HNTs are shown in Figure 8. The tensile strength, flexural strength and flexural modulus of PVC/PMMA-grafted HNTs nanocomposites are remarkably increased with increasing PMMA-grafted HNTs content (Figures 8a, b and c). Comparing with unfilled PVC, the tensile strength, flexural strength and flexural modulus of nanocomposites filled with 5 phr PMMA-grafted HNTs increases by 10, 12.7 and 42% respectively. The notched Izod impact strength of PVC/PMMA-grafted HNTs nanocomposites firstly increased with the loading of HNTs (Figures 8d). When the content of PMMA-grafted HNTs is 3 phr, the notched Izod impact strength of the nanocomposites is maximum, nearly double of that of pristine PVC. As the PMMA-grafted HNTs are increased to 5 phr, the notched Izod impact strength of the nanocomposites is a little decreased. This can be attributed to the agglomeration of HNTs. The mechanical properties results indicate that PVC can be reinforced and toughened by PMMA-grafted HNTs simultaneously.

3.6. Toughening mechanism

To investigate the toughening mechanism, the fracture surfaces of the nanpcomposites filled with 3 phr

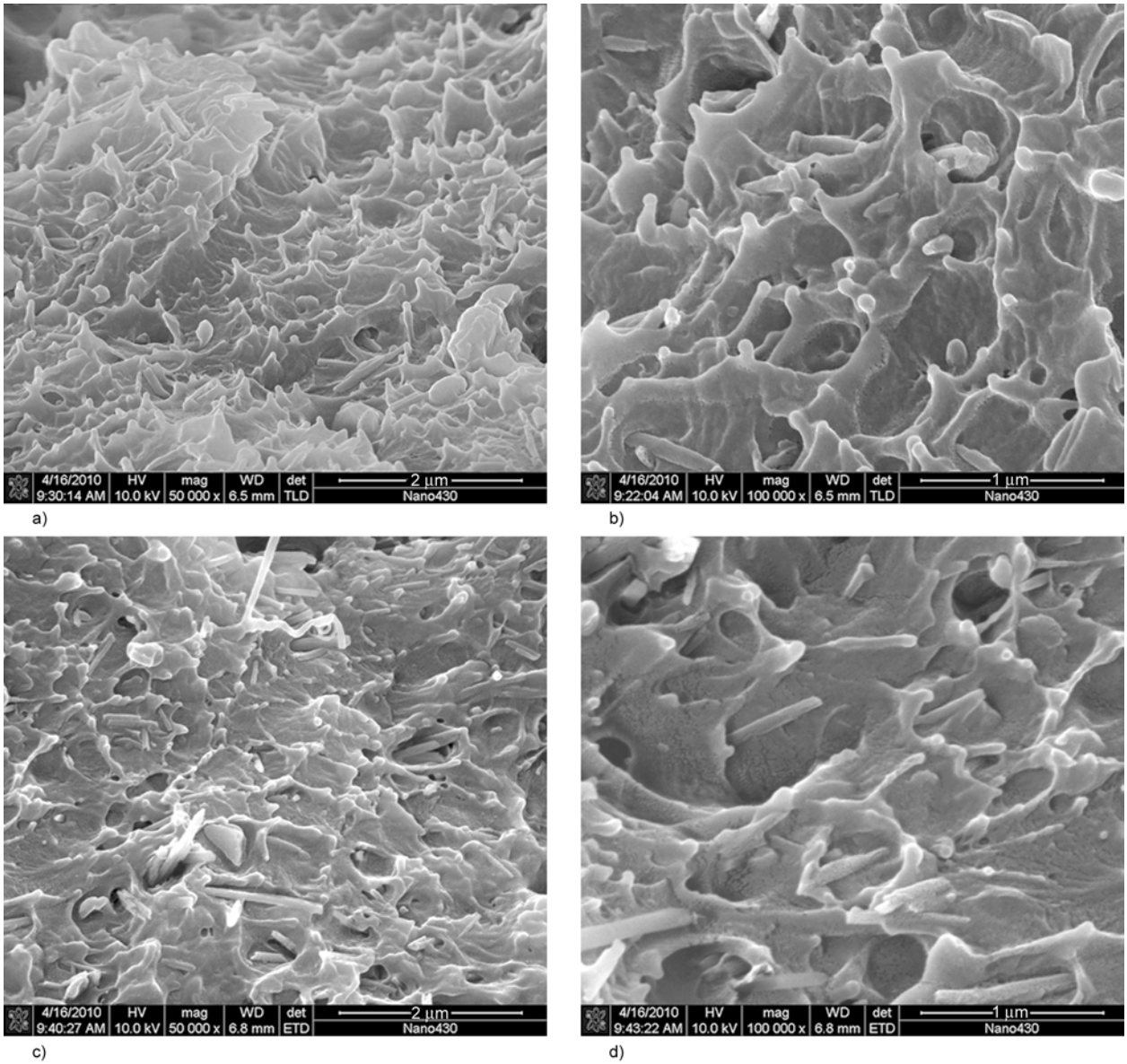

Figure 9. SEM micrographs of the impact fracture surfaces of PVC/PMMA-grafted HNTs nanpcomposites. (a) and (b) PVC/PMMA-grafted HNTs (100/3); (c) and (d) PVC/PMMA-grafted HNTs (100/5)

(Figures 9a and b) and 5 phr (Figures 9c and d) PMMA-grafted HNTs were examined using a high resolution SEM. As revealed in Figure 9, the debonding and pull-out of HNTs nanoparticles are clearly shown in the fracture surface, and the PVC matrix is severely drawn around the nanoparticles. According to the cavitation mechanism [33], the particles debond prior to the yield strain of the matrix polymer, lead to the debonding at the nanoparticle-polymer interface, then the matrix is highly deformed and drawn around the particles, which dissipates impact energy and toughens the nanocomposites. The PMMA-grafted HNTs have good compatibility with PVC matrix and disperse homogeneous in the PVC matrix. Therefore, stress can be transferred to the stronger inorganic phase when the PVC matrix is subjected to applied force, so reinforcing and toughening effects can be observed at very low PMMA-grafted HNTs content. Comparing Figure 9b with Figure 9d, it can be seen that the PMMA-grafted HNTs arrange more regularly and disperse more homogeneously in Figure 9b. While in Figure 9d, some HNTs arrange disorderly and some agglomeration can be observed. The agglomeration of HNTs weakens the interaction between PVC chains and HNTs. This is the reason why the toughness of the nanocomposite containing 5 phr PMMA-grafted HNTs slightly decreases comparing with that of the nanocomposites with 3 phr PMMA-grafted HNTs.

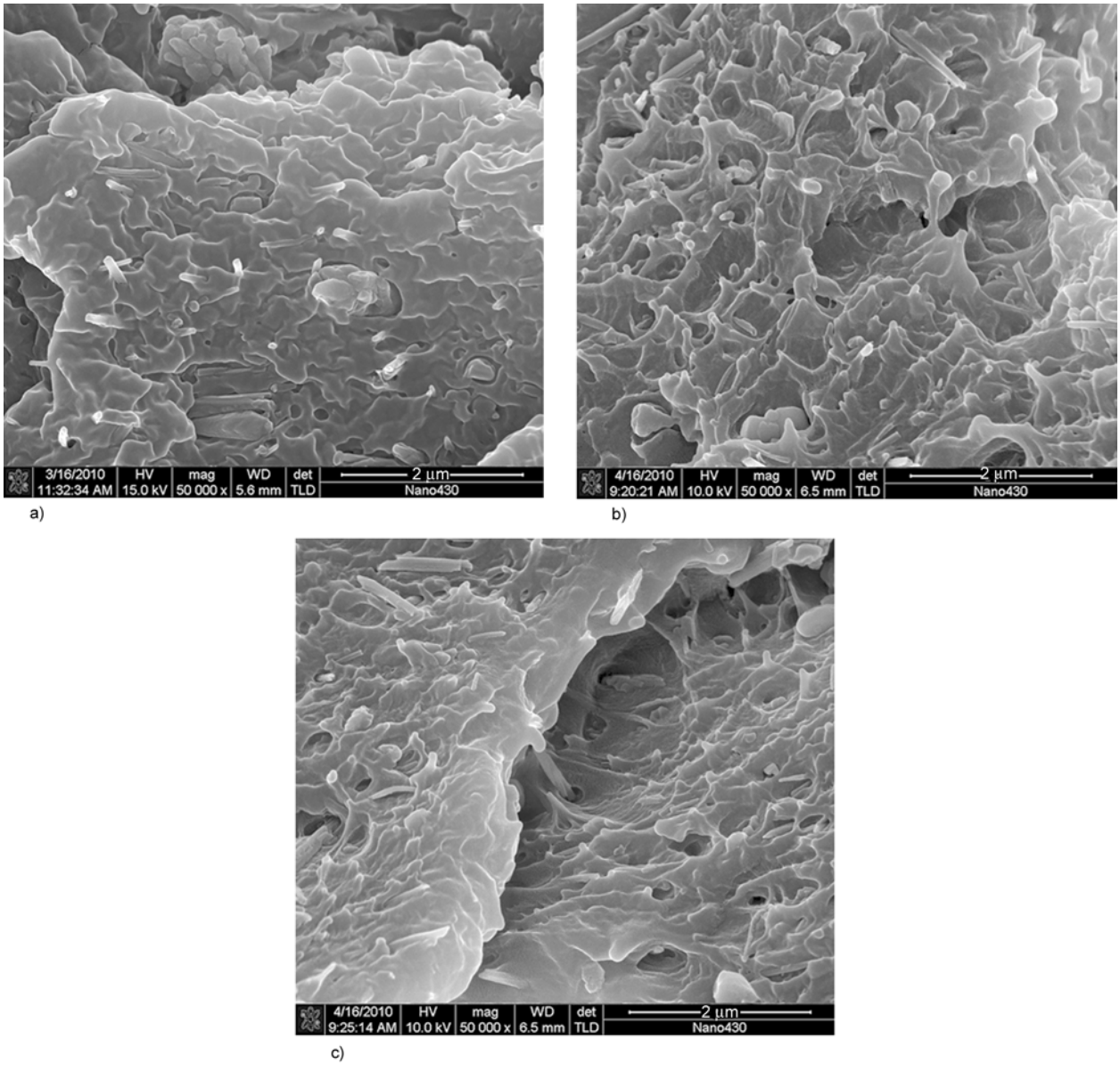

Figure 10. SEM micrographs of the impact fracture surfaces of PVC/HNTs and PVC/PMMA-grafted HNTs nanpcomposites. (a) PVC/HNTs (100/3); (b) and (c) PVC/PMMA-grafted HNTs (100/3)

To investigate the effect of PMMA shell covered on the surface of particles, the fracture surfaces of PVC/HNTs nanpcomposites and PVC/PMMA-grafted HNTs nanpcomposites with 3 phr particles loading were compared using a high resolution SEM (Figure 10a for the PVC/HNTs nanpcomposites and Figures 10b and c for the PVC/PMMA-grafted HNTs nanpcomposites). For Figure 10b, the rough fracture surface, the uniform dispersion of PMMA-grafted HNTs and high plastic deformation around the PMMA-grafted HNTs are observed. While for Figure 10a, the fracture surface is not so rough and the deformation is not as severe as that of Figure 10b. This is because PMMA is miscible with PVC thermodynamically [34], the solubility parameter of PMMA is 9.4 $(J/cm^3)^{1/2}$ similar to that of PVC which is 9.5 $(J/cm^3)^{1/2}$. So PMMA shell covered on the surface of HNTs particle increases the interaction of the HNTs with PVC matrix. Besides, the surface energy of HNTs is decreased after surface grafting. The dispersion of HNTs is improved, and the agglomeration is reduced. The good interfacial bonding makes the load transfer from the matrix to the rigid inorganic phase effectively. The nanoparticles-polymer interfaces are debonded and consume impact energy. In Figure 10c the crack can be observed, besides, the surfaces of the crack are uneven and the HNTs bridge the gap. This is similar to the observation about epoxy/HNT nanocomposite [10]. Because of the strong interfacial bonding between PMMA-grafted HNTs and PVC, the cracks can be stabilized by the nanotube bridging and stopped developing into large and harmful cracks. When the crackopening force exceeded their fracture strength the HNTs would be broken, which consumed the impact energy. Therefore, the PVC/PMMA-grafted nanocomposites exhibit high toughness.

4. Conclusions

PMMA-grafted HNTs synthesized by grafting methyl methacrylate on the surfaces of HNTs. The FTIR, TG, TEM, and XPS results confirmed the successful covalently modification of HNTs by PMMA. PVC/PMMA-grafted HNTs nanocomposites have been prepared by melt compounding. The PMMA-grafted HNTs could improve the toughness, strength, modulus of PVC nanocomposites simultaneously. TEM and SEM observations revealed that the PMMA-grafted HNTs uniformly dispersed in the PVC matrix. The fracture surfaces of the nanocomposites exhibited plastic deformation feature indicating ductile fracture behaviors. The improvement of toughness of PVC by PMMA-grafted HNTs was attributed to the improved interfacial bonding by grafting and the toughening mechanism was explained according to the cavitation mechanism.

Acknowledgements

The authors would like to acknowledge the XinJiang Tianye Group Co., Ltd.

References

[1] Wan C. Y., Qiao X. Y., Zhang Y., Zhang Y. X.: Effect of different clay treatment on morphology and mechanical properties of PVC-clay nanocomposites. Polymer Testing, **22**, 453–461 (2003). DOI: 10.1016/s0142-9418(02)00126-5

[2] Xie X-L., Liu Q-X., Li R. K-Y., Zhou X-P., Zhang Q-X., Yu Z-Z., Mai Y-W.: Rheological and mechanical properties of PVC/$CaCO_3$ nanocomposites prepared by in situ polymerization. Polymer, **45**, 6665–6673 (2004). DOI: 10.1016/j.polymer.2004.07.045

[3] Wang G. J., Wang L. J., Mei Z., Chang Z. M.: Reinforcement and toughening of poly(vinyl chloride) with poly(caprolactone) grafted carbon nanotubes. Composites Part A: Applied Science and Manufacturing, **40**, 1476–1481 (2009). DOI: 10.1016/j.compositesa.2009.05.011

[4] Xie X-L., Li R. K-Y., Liu Q-X., Mai Y-W.: Structure-property relationships of in-situ PMMA modified nano-sized antimony trioxide filled poly(vinyl chloride) nanocomposites. Polymer, **45**, 2793–2802 (2004). DOI: 10.1016/j.polymer.2004.02.028

[5] Zhu A. P., Cai A. Y., Zhang J., Jia H. W., Wang J. Q.: PMMA-grafted-silica/PVC nanocomposites: Mechanical performance and barrier properties. Journal of Applied Polymer Science, **108**, 2189–2196 (2008). DOI: 10.1002/app.27863

[6] Xie X. L., Li B. G., Pan Z. R., Li R. K. Y., Tjong S. C.: Effect of talc/MMA *in situ* polymerization on mechanical properties of PVC-matrix composites. Journal of Applied Polymer Science, **80**, 2105–2112 (2001). DOI: 10.1002/app.1310

[7] Du M. L., Guo B. C., Jia D. M.: Thermal stability and flame retardant effects of halloysite nanotubes on poly(propylene). European Polymer Journal, **42**, 1362–1369 (2006). DOI: 10.1016/j.eurpolymj.2005.12.006

[8] Liu M. X., Guo B. C., Du M. L., Chen F., Jia D. M.: Halloysite nanotubes as a novel β-nucleating agent for isotactic polypropylene. Polymer, **50**, 3022–3030 (2009).
DOI: 10.1016/j.polymer.2009.04.052

[9] Deng S. Q., Zhang J. N., Ye L., Wu J. S.: Toughening epoxies with halloysite nanotubes. Polymer, **49**, 5119–5127 (2008).
DOI: 10.1016/j.polymer.2008.09.027

[10] Ye Y. P., Chen H. B., Wu J. S., Ye L.: High impact strength epoxy nanocomposites with natural nanotubes. Polymer, **48**, 6426–6433 (2007).
DOI: 10.1016/j.polymer.2007.08.035

[11] Liu M. X., Guo B. C., Du M. L., Cai X. J., Jia D. M.: Properties of halloysite nanotube–epoxy resin hybrids and the interfacial reactions in the systems. Nanotechnology, **18**, 455703/1–455703/9 (2007).
DOI: 10.1088/0957-4484/18/45/455703

[12] Jia Z. X., Luo Y. F., Guo B. C., Yang B. T., Du M. L.: Reinforcing and flame-retardant effects of halloysite nanotubes on LLDPE. Polymer-Plastics Technology and Engineering, **48**, 607–613 (2009).
DOI: 10.1080/03602550902824440

[13] Guo B. C., Zou Q. L., Lei Y. D., Jia D. M.: Structure and performance of polyamide 6/halloysite nanotubes nanocomposites. Polymer Journal, **41**, 835–842 (2009).
DOI: 10.1295/polymj.PJ2009110

[14] Guo B. C., Zou Q. L., Lei Y. D., Du M. L., Liu M. X., Jia D. M.: Crystallization behavior of polyamide 6/halloysite nanotubes nanocomposites. Thermochimica Acta, **484**, 48–56 (2009).
DOI: 10.1016/j.tca.2008.12.003

[15] Rooj S., Das A., Thakur V., Mahaling R. N., Bhowmick A. K., Heinrich G.: Preparation and properties of natural nanocomposites based on natural rubber and naturally occurring halloysite nanotubes. Materials and Design, **31**, 2151–2156 (2010).
DOI: 10.1016/j.matdes.2009.11.009

[16] Du M. L., Guo B. C., Lei Y. D., Liu M. X., Jia D. M.: Carboxylated butadiene–styrene rubber/halloysite nanotube nanocomposites: Interfacial interaction and performance. Polymer, **49**, 4871–4876 (2008).
DOI: 10.1016/j.polymer.2008.08.042

[17] Pasbakhsh P., Ismail H., Fauzi M. N. A., Abu Bakar A.: Influence of maleic anhydride grafted ethylene propylene diene monomer (MAH-g-EPDM) on the properties of EPDM nanocomposites reinforced by halloysite nanotubes. Polymer Testing, **28**, 548–559 (2009).
DOI: 10.1016/j.polymertesting.2009.04.004

[18] Mondragón M., Roblero-Linares Y. S., Sánchez-Espindola M. E., Zendejas-Leal B. E.: Rigid poly(vinyl chloride)/halloysite nanocomposites. in 'Nanotech conference and expo 2009, Technical proceedings – Nanotechnology 2009: Life Sciences, medicine, diagnostics, bio materials and composites. Boca Raton, USA, 482–484 (2009).

[19] Zhang Y. W., Jiang J. Q., Liang Q. H., Zhang B.: Modification of halloysite nanotubes with poly(styrene–butyl acrylate–acrylic acid) via *in situ* soap-free graft polymerization. Journal of Applied Polymer Science, **117**, 3054–3059 (2010).
DOI: 10.1002/app.32087

[20] Wan C. Y., Li M., Bai X., Zhang Y.: Synthesis and characterization of photoluminescent Eu(III) coordination halloysite nanotube-based nanohybrids. Journal of Physical Chemistry C, **113**, 16238–16246 (2009).
DOI: 10.1021/jp9051648

[21] Moulder J. F., Stickle W. F., Sobol P. E., Bomben K. D.: Handbook of X ray photoelectron spectroscopy. Perkin-Elmer Corporation, Minnesota (1992).

[22] Liu M. X., Guo B. C., Du M. L., Lei Y. D., Jia D. M.: Natural inorganic nanotubes reinforced epoxy resin nanocomposites. Journal of Polymer Research, **15**, 205–212 (2008).
DOI: 10.1007/s10965-007-9160-4

[23] Meng X. Y., Wang Z., Tang T.: Controlling dispersed state and exfoliation process of clay in polymer matrix. Materials Science and Technology, **22**, 780–786 (2006).
DOI: 10.1179/174328406x101238

[24] Manchado M. A. L., Valentini L., Biagiotti J., Kenny J. M.: Thermal and mechanical properties of single-walled carbon nanotubes–polypropylene composites prepared by melt processing. Carbon, **43**, 1499–1505 (2005).
DOI: 10.1016/j.carbon.2005.01.031

[25] Yang C. J., Gong C. Q., Peng T. Y., Deng K. J., Zan L.: High photocatalytic degradation activity of the polyvinyl chloride (PVC)–vitamin C (VC)–TiO_2 nano-composite film. Journal of Hazardous Materials, **178**, 152–156 (2010).
DOI: 10.1016/j.jhazmat.2010.01.056

[26] Gojny F. H., Wichmann M. H. G., Fiedler B., Schulte K.: Influence of different carbon nanotubes on the mechanical properties of epoxy matrix composites – A comparative study. Composites Science and Technology, **65**, 2300–2313 (2005).
DOI: 10.1016/j.compscitech.2005.04.021

[27] Awad W. H., Beyer G., Benderly D., Ijdo W. L., Songtipya P., Jimenez-Gasco M. D., Manias E., Wilkie C. A.: Material properties of nanoclay PVC composites. Polymer, **50**, 1857–1867 (2009).
DOI: 10.1016/j.polymer.2009.02.007

[28] Sheng S. S., Ling Z., Zhong L. C., Ming C. H., Ling Z. Q.: Effect of properties of $CaCO_3$ nanoparticles on interface and properties of poly (vinyl chloride) composites (in Chinese). Journal of Chemical Industry and Engineering, **56**, 2233–2239 (2005).

[29] Peng S. W., Wang X. Y., Dong L. S.: Special interaction between poly (propylene carbonate) and corn starch. Polymer Composites, **26**, 37–41 (2005).
DOI: 10.1002/pc.20070

[30] Jancar J.: Influence of filler particle shape on elastic moduli of PP/$CaCO_3$ and PP/$Mg(OH)_2$ composites, Part 1 'Zero' interfacial adhesion. Journal of Materials Science, **24**, 3947–3955 (1989).
DOI: 10.1007/BF01168958

[31] Wan C. Y., Tian G. H., Cui N., Zhang Y. X., Zhang Y.: Processing thermal stability and degradation kinetics of poly(vinyl chloride)/montmorillonite composites. Journal of Applied Polymer Science, **92**, 1521–1526 (2004).
DOI: 10.1002/app.20086

[32] Gong F. L., Feng M., Zhao C. G., Zhang S. M., Yang M. S.: Thermal properties of poly(vinyl chloride)/montmorillonite nanocomposites. Polymer Degradation and Stability, **84**, 289–294 (2004).
DOI: 10.1016/j.polymdegradstab.2003.11.003

[33] Zuiderduin W. C. J., Westzaan C., Huetink J., Gaymans R. J.: Toughening of polypropylene with calcium carbonate particles. Polymer, **44**, 261–275 (2003).
DOI: 10.1016/S0032-3861(02)00769-3

[34] Olabisi O., Robeson L. M., Shaw M. T.: Polymer–polymer miscibility. Academic Press, New York (1979).

eXPRESS Polymer Letters Vol.5, No.7 (2011) 604–619
Available online at www.expresspolymlett.com
DOI: 10.3144/expresspolymlett.2011.59

Polyol mediated nano size zinc oxide and nanocomposites with poly(methyl methacrylate)

A. Anžlovar[1*], *K. Kogej*[2], *Z. Crnjak Orel*[1], *M. Žigon*[1]

[1]National Institute of Chemistry, Hajdrihova 19, SI-1000, Ljubljana, Slovenia
[2]University of Ljubljana, Faculty of Chemistry and Chemical Technology, Aškerčeva 5, Ljubljana, Slovenia

Received 19 October 2010; accepted in revised form 17 January 2011

Abstract. Organophilic nano ZnO particles have been synthesized in various diols (ethylene glycol – EG, 1,2 propane diol – PD, 1,4 butane diol – BD and tetra(ethylene glycol) – TEG) in the presence of *p*-toluenesulfonic acid, p-TsOH, as an end capping agent. The addition of p-TsOH reduces the ZnO particle size and increases its crystallite size. With increasing diol main chain length the ZnO particle size increases (EG (32 nm) < PD (33 nm) < BD (72 nm) < TEG (86 nm)). Using the as-synthesized and unmodified ZnO nanocomposites with poly(methyl methacrylate), PMMA, matrix have been prepared by the in-situ bulk polymerization of methyl methacrylate, MMA. The addition of surface modifiers is avoided which is an advantage for the application since they can influence other properties of the material. ZnO particles, especially those with smaller particle sizes (EG – 32 nm, PD – 33 nm) showed enhanced effect on the thermal stability of PMMA, ultraviolet, UV, absorption and transparency for visible light. Transparent materials with high UV absorption and with enhanced resistance to sunlight were obtained by optimizing the nanocomposite preparation procedure using ZnO particles of about 30 nm size in concentrations between 0.05 and 0.1 wt%. The reported nanocomposite preparation procedure is compatible with the industrial process of PMMA sheet production.

Keywords: *nanocomposites, ZnO nanoparticles, PMMA, UV absorption, processing technologies*

1. Introduction

Zinc (II) oxide, ZnO, is conventionally used as a catalyst [1] and initiator in various chemical reactions [2], gas sensor material [3, 4], UV absorber and pigment in cosmetics [5] and paints [6, 7]. It is widely used in various electronic applications such as material for varistors etc. [8, 9]. Recently it has been intensively studied as a promising material for optoelectronic devices such as light emitting diodes (LED) and flat display screens [10, 11]. ZnO is considered as an interesting material for solar applications due to its unique combination of optical and semiconducting properties [12]. ZnO has an optical band gap in the UV region and this makes it an extremely efficient UV absorber [13]. It is also an environmentally friendly material, at least in the micrometer particle size range.

ZnO can be synthesized by various synthetic paths in various shapes and particle sizes [14–16]. Advanced applications require nanoparticles with narrow particle size distribution and defined particle shape. Therefore, the research activities on nanoscale ZnO synthesis and characterization have increased significantly in the last few years. Various synthetic approaches have been reported in the literature, including hydrothermal [17–19] and solvothermal methods [20–22], microemulsion [23], sol-gel method [24], and thermal decomposition of precursors [25, 26]. These chemical processes are efficient methods for preparation of nanoparticles and may

*Corresponding author, e-mail: alojz.anzlovar@ki.si

be scaled up to produce large quantities of material [27, 28].

The polyol method is one of the solvothermal methods of ZnO synthesis involving the hydrolysis of ZnO precursors in various diols (polyols). Diols are solvents with medium polarity, dielectric constants are between 20 and 40, and they have high boiling temperatures. They can dissolve many zinc compounds and they act as solvents, reducing, as well as stabilizing agents and prevent particle growth [29–31]. Synthesis of inorganic particles in organic media is attractive because it produces particles with an organophilic surface originating from an organic medium or its degradation products. Such particles need no additional surface modification for polymer nanocomposite applications.

Poly(methyl methacrylate) is a thermoplastic material with outstanding optical properties and favorable mechanical as well as processing properties. Due to its favorable properties it can replace inorganic glass in many applications [32]. It is known that a combination of organic polymer matrices and inorganic particles offers materials with enhanced mechanical, thermal, electrical, magnetic, optical and many other specific properties. By reducing the size of filler particles to the nanometer range, their specific surface area as well as the interface area in composites is substantially increased and, consequently, their impact on composite properties is either enhanced or the same impact is achieved at lower concentrations of the filler. By combining the nano ZnO and PMMA matrix, transparent materials with high UV absorption can be prepared, providing that homogeneous particle distribution in the polymer matrix is achieved. For that reason the particle surface needs to be hydrophobically modified. In most cases various organic ligands are used for modification, such as: alkyl silanes, oligomeric silicones, alkyl phosphonic or fatty acids as well as various statistical and block copolymers [33–37]. By in-situ bulk polymerization of MMA in the presence of ZnO nanoparticles, transparent ZnO/PMMA nanocomposites with a high concentration of ZnO have already been prepared [38–43].

The aim of our work was first to synthesize nano ZnO with organophilic surface and narrow particle size distribution by the polyol method in various diols. *p*-Toluenesulfonic acid as an end capping agent was used at high concentrations, giving ZnO particles with average sizes between 20 and 100 nm in gram quantities. Second, we tested the as-synthesized nano ZnO for preparation of homogeneous and transparent ZnO/PMMA nanocomposites with high UV absorption and with improved thermal stability.

2. Experimental section

2.1. Materials

Ethylene glycol (Merck, p.a.,); 1,2 propane diol (for synthesis, Merck,Germany); 1,4 butane diol (99%, Sigma-Aldrich, St. Louis, USA); Tetra(ethylene glycol) (99%, Sigma-Aldrich, St. Louis, USA); Zinc (II) acetate monohydrate $Zn(Ac)_2$ (99%, ACS reagent, Sigma-Aldrich, St. Louis, USA); *p*-Toluenesulfonic acid monohydrate – p-TsOH (98.5%, ACS reagent, Sigma-Aldrich, St. Louis, USA); Methyl methacrylate (99%, Sigma-Aldrich, St. Louis, USA); *1,1-Azobis*(1-cyclohexanecarbonitrile) – AICN (98%, Sigma-Aldrich, St. Louis, USA); ethanol (96%, technical, Ke-Fo, Slovenia).

2.2. Synthesis of ZnO nanoparticles

Zinc (II) acetate (1.0 M), p-TsOH (0.1 M) and deionised water (2 mol/1 mol Zn) were mixed with 60 ml of EG, PD, BD or TEG and sonicated for 10 min. The mixture was transferred into a 250 ml glass reactor equipped with a mixer, condenser and digital thermometer. The temperature and color changes of the reaction medium were monitored over time. The temperature was raised over about 30 min to 170°C and kept constant for 30 min with constant stirring. Between 70 and 90°C, $Zn(Ac)_2$ dissolved in the glycol and the solution became transparent. After 10 minutes at 170°C the solution became white, and after 60 minutes of reaction a white suspension of ZnO was obtained. The suspension was left overnight and centrifuged at 8000 rpm for 20 min to separate the particles from the supernatant. Subsequently, the ZnO was washed twice with ethanol followed by forced separation of ZnO particles in a centrifuge (8000 rpm, 20 min). The obtained ZnO powder was left to air dry. Synthesis of ZnO without p-TsOH was done at $Zn(Ac)_2$ concentration of 0.1 M.

2.3. Synthesis of ZnO/PMMA nanocomposites

Nanocomposites of synthesized ZnO particles and PMMA matrix were prepared by the radical chain

polymerization of MMA in bulk in three variations: radical polymerization between glass plates starting directly from the ZnO dispersion in monomer – MMA (*Procedure A*); polymerization between glass plates starting from the previously prepared dispersion of ZnO in prepolymer (*Procedure B*); polymerization between two glass plates starting from ZnO prepolymer dispersion polymerized during constant sonication (*Procedure C*). The nanocomposite plate thickness using procedure A was 1.5 mm, while procedures B and C gave nanocomposite plates with a thickness of 3.5 mm. Procedures B and C were applied to reduce the shrinking of PMMA during polymerization and also to reduce the size or break up of the agglomerates of nano ZnO particles in the PMMA prepolymer.

Procedure A. An initiator AICN (0.0163 mol.%) was first dissolved in MMA. Various amounts of ZnO powder, synthesized in diols (0.01, 0.1 and 1.0 wt%), were suspended in this solution by mixing and sonication. The solution was sonicated for 20 min and was then transferred into the glass plate mold and sonicated for an additional 5 min. The glass mold was put into the water bath and MMA was polymerized for 20 hours at 75°C. After 20 hours, the molds were taken from the bath, and PMMA sheets with a thickness of 1.5 mm were separated from the glass plate molds.

Procedure B. An initiator AICN (0.0163 mol.%) was first dissolved in MMA. Various amounts of ZnO powder, synthesized in diols (0.01, 0.1 and 1.0 wt%), were suspended in this solution by mixing and sonication. The solution was sonicated for 20 min and was then transferred into the glass reactor equipped with mixer, reflux condenser and thermometer. The dispersion was heated at 80°C for 2 hours during constant mixing to partially polymerize the MMA. After 2 hours the prepolymer was cooled down; 20% of the new initiator dissolved in 5 ml of MMA was added and sonicated again for 20 min. This prepolymer was transferred to a glass mold which was put into the water bath, and MMA was polymerized for 20 hours at 75°C. After 20 hours, the molds were taken from the bath and PMMA sheets with a thickness of 3.5 mm were separated from the glass plate molds.

Procedure C. Procedure C differed from procedure B only in that the reactor was constantly sonicated during synthesis of the prepolymer.

2.4. Characterization methods

The chemical composition of the intermediates and obtained particles was studied by Fourier transform infrared spectroscopy, FTIR using an FTIR spectrometer Spectrum One (Perkin Elmer, Beaconsfield, Great Britain) in the spectral range between 400 and 4000 cm^{-1} with a spectral resolution of 4 cm^{-1} in transmittance mode using the KBr pellets technique.

The morphology and size of the synthesized particles were studied by scanning electron microscopy – SEM. SEM micrographs of gold sputtered samples were taken on a Zeiss Supra 35 VP field emission electron microscope (Ziess, Oberkocken, Germany) at an acceleration voltage of 3.37 or 5.0 kV using mixed in-lens and secondary electrons detectors at a ratio of 0.75/0.25 and a working distance between 3–6 mm. For SEM microscopy, ZnO powders were placed on conductive film and sputtered with Au. The ZnO particle distribution in ZnO/PMMA nanocomposite materials was studied by the scanning transmission electron microscopy – STEM of ultramicrotomed sections of the nanocomposites. STEM micrographs were taken on a Zeiss Supra 35 VP at an acceleration voltage of 20.0 kV and working distance of 4.5–5 mm using a STEM electron detector. For STEM and HR TEM microscopy, ZnO particles were dispersed in an organic solvent (e.g. ethanol) by sonication and a drop of dispersion was transferred to a Cu grid and dried. ZnO/PMMA nanocomposites were sectioned on the ultramicrotome Leica Ultracut (Leica, Vienna, Austria) to a thickness between 80 and 250 nm. Particle size distribution of ZnO particles was obtained from STEM micrographs by image analysis using the Image Tool software.

The sizes of ZnO nanoparticles and their aggregates in MMA were measured by dynamic light scattering using the 3D-DLS-SLS spectrometer (LS Instruments, Fribourg, Switzerland) equipped with 20 mV He-Ne laser (Uniphase JDL 1145 P) operating at 632.8 nm. Scattering was measured at an angle of 90°. Samples in the scattering cells were immersed in a large diameter bath thermostated at 20°C, and ten measurements of 60 s were recorded for each sample and averaged afterwards. In a DLS experiment the translational diffusion coefficient D is determined while the hydrodynamic radius R_h is calculated from D using Stokes-Einstein equation

[44]. The viscosity of the solvent (MMA) needed for this calculation was η = 0.6 cP at 20°C.

The molecular weight distribution of the PMMA matrix was determined by size exclusion chromatography, SEC, on a modular system composed of an isocratic pump – Hewlett Packard 1100 Series (Hewlett Packard, Germany), an AM polymer GPC gel linear (1000–5 000 000 g/mol) column (AM polymer, USA), and a precolumn (AM polymer GPC gel, linear), while a differential refractometer – Hewlett Packard Agilent 1160 series (Hewlett Packard, Germany) was used as a detector. The solvent was tetrahydrofuran (THF) with a flow rate of 1 ml/min, injection volume 50 µl and a detector temperature 25°C. PMMA standards were used for calibration. PMMA specimens were dissolved in THF (conc. = 2 mg/ml) and filtered using Millipore – Millex PTFE LCR filters (Millipore, USA) with a pore diameter of 0.45 µm.

Crystalline fractions of the synthesized powders were characterized by wide angle X-ray diffraction (XRD) on an XPert Pro diffractometer (PANalytical, Netherlands) with a Cu anode as the X-ray source. X-ray diffractograms were measured at 25°C in the 2Θ range from 2 to 90° with a step of 0.04° and step time of 1 s. Crystallite sizes were calculated using the Scherrer formula, and an Si wafer was used to determine the experimental broadening.

Thermal properties of ZnO/PMMA nanocomposites were studied on a Netzsch STA 409 instrument (Netzsch, Selb, Germany). DTG curves were measured in the temperature range between 50–600°C with a heating rate of 1°C/min and an air flux of 100 ml/min. The sample quantity was close to 50 mg.

UV-VIS spectra of ZnO/PMMA nanocomposites were measured on an Agilent 8453 UV-VIS spectrometer (Agilent Technologies, Waldbronn, Germany) in the spectral range between 290 and 380 nm. 1.6 mm thick sheets of ZnO/PMMA nanocomposites were cut to the width of a quartz cuvette.

Resistance to sun light was measured according to the ISO 4892-12 standard by exposing the specimen to a xenon light in an Atlas Sun Test CPS$^+$ chamber (Atlas, Altenham, Germany) for 720 hours. The color change, ΔE, was measured by Datacolor CR-10 color reader (Minolta, Japan).

^{13}C nuclear magnetic resonance spectra, NMR of PMMA matrices were recorded on a Varian Unity Inova 30 MHz spectrometer (Varian, Palo Alto, California, USA) under the following quantitative conditions: pulse 90°, delay 2.0 s, acquisition time 2.0 s, and temperature 25°C. DMSO-d6 was added in an insert and the spectra were referenced to its resonance at 39.5 ppm.

3. Results and discussion

3.1. Synthesis of nano ZnO

Synthesis of ZnO was performed in various diols (BD, TEG, EG and PD) with the addition of p-TsOH, which, according to the literature, acts as a catalyst [14]. Yields of the reaction were between 25 and 35%. Nano ZnO powders were characterized by SEM, STEM, XRD and FTIR. The SEM and HRTEM micrographs show ZnO nanoparticles, synthesized in various diols with p-TsOH (Figure 1a–d). Particles are predominantly crystallites with sizes between 30 and 100 nm as estimated from SEM micrographs (Table 1). By the image analysis of STEM micrographs average particle sizes were calculated and are summarized in Table 1 as average Ferret diameters. The average Ferret particle diameter of ZnO, synthesized in various diols, decreases from 86.2 nm (TEG) and 71.7 nm (BD), to 33.3 nm (PD) and 32.1 nm (EG). When particle size is presented as a function of the diols' structure, a correlation between the chain length between two OH groups of the diol and the average size of the ZnO particles was observed. Diols with a shorter chain length produce ZnO with a smaller average

Table 1. Crystallite sizes and average Ferret particle diameters of ZnO particles synthesized in various diols as well as average Ferret particle diameters of ZnO in nanocomposites

Sample designation	Particle size – SEM [nm]	Crystallite sizes [nm]	Ferret diameter – ZnO [nm]	Ferret diameter – nanocomposite [nm]
TEG no p-TsOH	300–400	17.5	340.0±56	–
TEG	50–100	114.2	86.2±27	135.9±46
BD	50–150	75.8	71.7±20	122.3±41
PD	30–50	38.1	33.3±12	104.0±31
EG	20–40	32.6	32.1±13	108.4±33

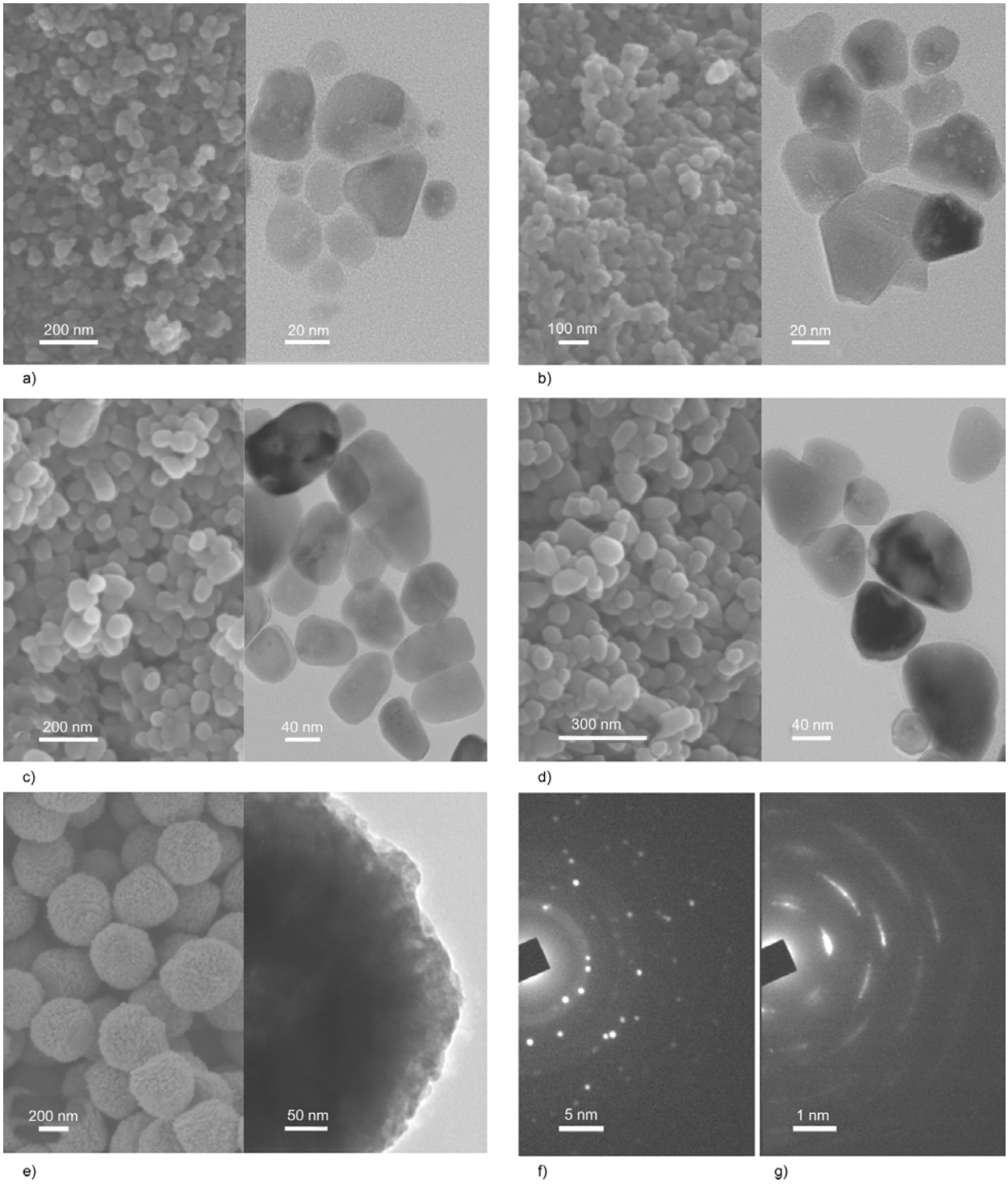

Figure 1. SEM and HRTEM micrographs of nano ZnO particles, synthesized with p-TsOH in various diols: a) EG, b) PD, c) BD, d) TEG, e) TEG without p-TsOH, f) electron diffraction pattern of nano ZnO – 32 nm (EG) and g) electron diffraction pattern of ZnO – 340 nm (TEG without p-TsOH)

particle size and *vice versa*. Similar observations were also reported by Jézéquel *et al.* [29]. The electron diffraction patterns of all the nano ZnO (Figure 1a–d) are similar and a representative pattern is shown in Figure 1f indicating that this ZnO is polycrystalline.

XRD diffractograms of all the ZnO powders synthesized in the presence of p-TsOH show characteristic diffraction peaks of crystalline ZnO with hexagonal zincite structure (PDF 00-036-1451) at 2Θ values: 31.8; 34.5; 36.2; 47.6; 56.6; 62.9; 66.4; 67.9; 69.1; 72.6; 76.9° [45]. Since all the diffrac-

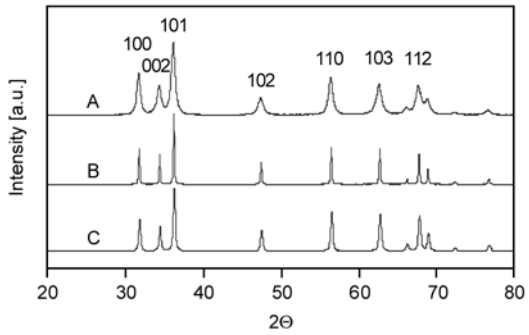

Figure 2. X-ray diffractograms of submicrometer and nano ZnO, synthesized by the polyol procedure in: A) TEG without p-TsOH, B) TEG with p-TsOH, C) PD with p-TsOH

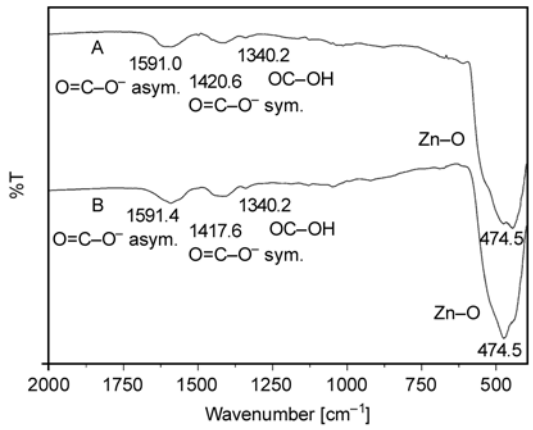

Figure 3. FTIR spectra of nano ZnO powders, synthesized by the polyol procedure with p-TsOH in: A) TEG, B) PD

tograms are almost identical, only two samples are shown (Figure 2). Very narrow diffraction peaks indicate relatively large crystallite sizes, and crystallite sizes – calculated by the Scherrer equation [46] (Table 1), agree well with particle sizes from SEM micrographs, indicating that ZnO particles, synthesized in the presence of p-TsOH, are highly crystalline.

When ZnO was prepared in TEG without p-TsOH by the same procedure as described above (Figure 1e), particles of submicrometer size were obtained. They have an irregular spherical shape and narrow particle size distribution. The particle size is estimated from SEM micrographs to be between 300 and 400 nm. Synthesis of ZnO by the polyol method in other diols (BD, EG, PD) without p-TsOH did not give ZnO of a particulate shape. The XRD diffractogram of ZnO, synthesized in TEG with no p-TsOH (Figure 2 A), shows relatively wide characteristic ZnO diffraction maxima indicating small crystallite sizes (17.5 nm, Table 1). Comparing the particle size and crystallite size of these particles, it is evident that they are actually agglomerates of nanocrystallites as is confirmed by SEM and HR TEM micrographs (Figure 1e). The electron diffraction pattern of this sample (Figure 1g) shows that this ZnO is polycrystalline. Crystallites are most probably organized in plates, which can be observed also on SEM micrograph (Figure 1e), with axes rotated for a few ° one to another.

Comparison of average Ferret diameters and crystallite sizes of ZnO, synthesized in TEG with and without the addition of p-TsOH (Table 1), leads to the conclusion that added p-TsOH prevents the agglomeration of nanocrystallites, thus substantially reducing the ZnO particle size (Figure 1d and e).

FTIR spectra of all ZnO powders, synthesized with and without p-TsOH, show dominant characteristic ZnO absorption bands between 420 and 480 cm^{-1}, which correspond to two transverse optical stretching modes of ZnO [47]. Since all the FTIR spectra are practically identical only two of them are shown (Figure 3). Additional absorption bands of organic species at 1590, 1415 and 1340 cm^{-1} were observed in all the samples. They may originate from the tetra nuclear oxo zinc acetate cluster ($Zn_4O(CH_3COO)_6$) [48, 49] and are an indication of an organophilic particle surface. $Zn_4O(CH_3COO)_6$ species were identified by ^{13}C NMR spectroscopy by Berkesi *et al*. [50]. The ^{13}C NMR spectrum of TEG solution after 20 min of reaction (Figure 4b) shows a strong carbonyl peak of acetylated TEG at 171.2 and 20.4 ppm, indicating that a part of acetate groups from $Zn(Ac)_2$ are involved in the esterification reaction. The resulting ZnO forms a complex with three molecules of $Zn(Ac)_2$, generating a $Zn_4O(CH_3COO)_6$ cluster. In the ^{13}C NMR spectrum of the TEG solution after 20 min of reaction (Figure 4b) there are signals at 23.0 and 180.1 ppm, which differ from the signals of Zn(Ac) in TEG (22.4 and 178 ppm – Figure 4a). $Zn(Ac)_2$ and $Zn_4O(CH_3COO)_6$ are similar molecules with respect to CH_3 groups of acetate and therefore their signals in NMR spectra can not greatly differ. Nevertheless, the shift of carbonyl signal to the lower field by 2.1 ppm is favorable to the $Zn_4O(CH_3COO)_6$ cluster. It is reported that the $Zn_4O(CH_3COO)_6$ cluster can grow to larger clusters, such as $Zn_{10}O_4(CH_3COO)_{12}$ and $Zn_{34}O_{16}(CH_3COO)_{24}$

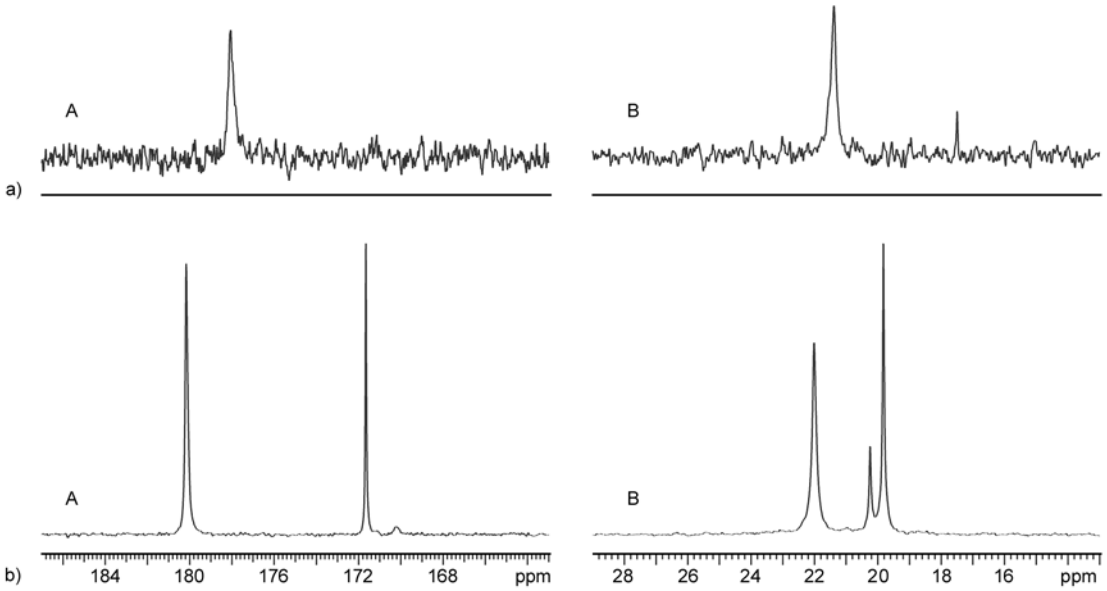

Figure 4. ^{13}C NMR spectra of: a) $Zn(Ac)_2$ solution in TEG and b) reaction intermediates of $Zn(Ac)_2$ hydrolysis in TEG after 20 min of reaction with p-TsOH: A) carbonyl region, B) aliphatic carbon region

[51] and so on, which are precursors for the formation of ZnO particles containing a $Zn(CH_3COO)_2$ layer on the surface. Based on ^{13}C NMR results, we propose the following reaction scheme (Equations (1) and (2)) of Zn acetate hydrolysis in diols [52]:

$$4Zn(CH_3COO)_2 + H_2O + HO–R–HO \leftrightarrow Zn_4O(CH_3COO)_6 + CH_3COO–R–OOCH_3 + 2H_2O \quad (1)$$

$$Zn_4O(CH_3COO)_6 \rightarrow 3Zn(CH_3COO)_2 + ZnO \quad (2)$$

3.2. Synthesis of nanocomposites

Nanocomposites of unmodified as-synthesized ZnO particles and PMMA matrix were prepared by the free radical polymerization of MMA in bulk between two glass plates. For the preparation of homogeneous ZnO/PMMA nanocomposites the dispersion stability of nanoparticles in the MMA monomer and the degree of their aggregation are of key importance. The dispersion stability of the nano ZnO was studied by dynamic light scattering by monitoring the hydrodynamic radius – R_h of ZnO nanoparticles in the MMA monomer. Results, summarized in Table 2, show higher values of R_h at higher ZnO concentration as was expected, however, R_h is practically independent of time. Comparison of R_h values after 10 and 25 min shows a slight increase in size while at longer times (45 min) R_h remains constant or even slightly decreases, meaning that nano ZnO dispersions in MMA are stable for at least 45 min. R_h values are larger as compared to average Ferret diameters of neat ZnO particles (Table 1), indicating that agglomerates consist of around four to eight individual particles. R_h of ZnO particles, synthesized in BD, at a concentration of 0.1wt% could not be measured due to intense multiple scattering as a consequence of intense particle aggregation. The stability of ZnO nanoparticles in MMA can be ascribed to strong interaction between the ZnO sur-

Table 2. Hydrodynamic radii of ZnO particles in MMA dispersion in dependence on the concentration and time

Sample designation	ZnO [wt%]	R_h [nm]		
		Time (10 min)	Time (25 min)	Time (45 min)
ZnO (TEG)/PMMA	0.01	138	153	139
ZnO (TEG)/PMMA	0.1	138	188	171
ZnO(BD)/PMMA	0.01	107	98	103
ZnO (BD)/PMMA	0.1	–	–	–
ZnO (EG)/PMMA	0.01	83	81	84
ZnO (EG)/PMMA	0.1	124	95	135
ZnO (PD)/PMMA	0.01	67	78	77
ZnO (PD)/PMMA	0.1	113	149	132

face and the carbonyl group of MMA [53]. Molar mass averages of PMMA were measured by SEC in dependence of the polymerization time. At 45 minutes of polymerization, molar mass averages of PMMA reach values above 100 000 g/mol and due to the high viscosity of the medium, ZnO particles remain trapped in the polymer, and their sedimentation is prevented despite their seven times higher density compared to MMA.

Nanocomposites were first prepared by simply dispersing nano ZnO in MMA using sonication and by transferring the resulting dispersion into a glass mould which was put into a water bath at 75°C (Procedure A). STEM micrographs in Figure 5 show the distribution of ZnO in PMMA/ZnO nanocomposites. ZnO particles, synthesized in BD (Figure 5a) and those synthesized in TEG (Figure 5b) form larger agglomerates, while ZnO, synthesized in PD or EG, formed small, extended agglomerates which are homogeneously distributed in the PMMA matrix (Figure 5c and d). The lower number of particles or agglomerates in Figure 5a and b can be explained that larger ZnO particles form larger agglomerates which can partly undergo sedimentation. Ferret diameters calculated by the Image Analysis of ZnO particles in TEM micrographs of nanocomposites are shown in Table 1 in comparison with Ferret diameters of neat ZnO particles. It can be seen that average Ferret diameters of ZnO in nanocomposites are larger than those of neat ZnO particles, which means that in nanocomposites ZnO is slightly agglomerated (Table 1). It forms aggregates of four to eight individual ZnO particles. The agglomeration process is more intense for smaller particles because they provide a larger specific surface area, and thus the higher van der Waals force that causes more intense ZnO aggregation.

Many inorganic nanoparticles enhance the thermal stability of PMMA, when MMA is polymerized in their presence [54]. The addition of nano ZnO also thermally stabilizes the PMMA matrix [37, 54, 55]. The DTG curve of pure PMMA (Figure 6) shows

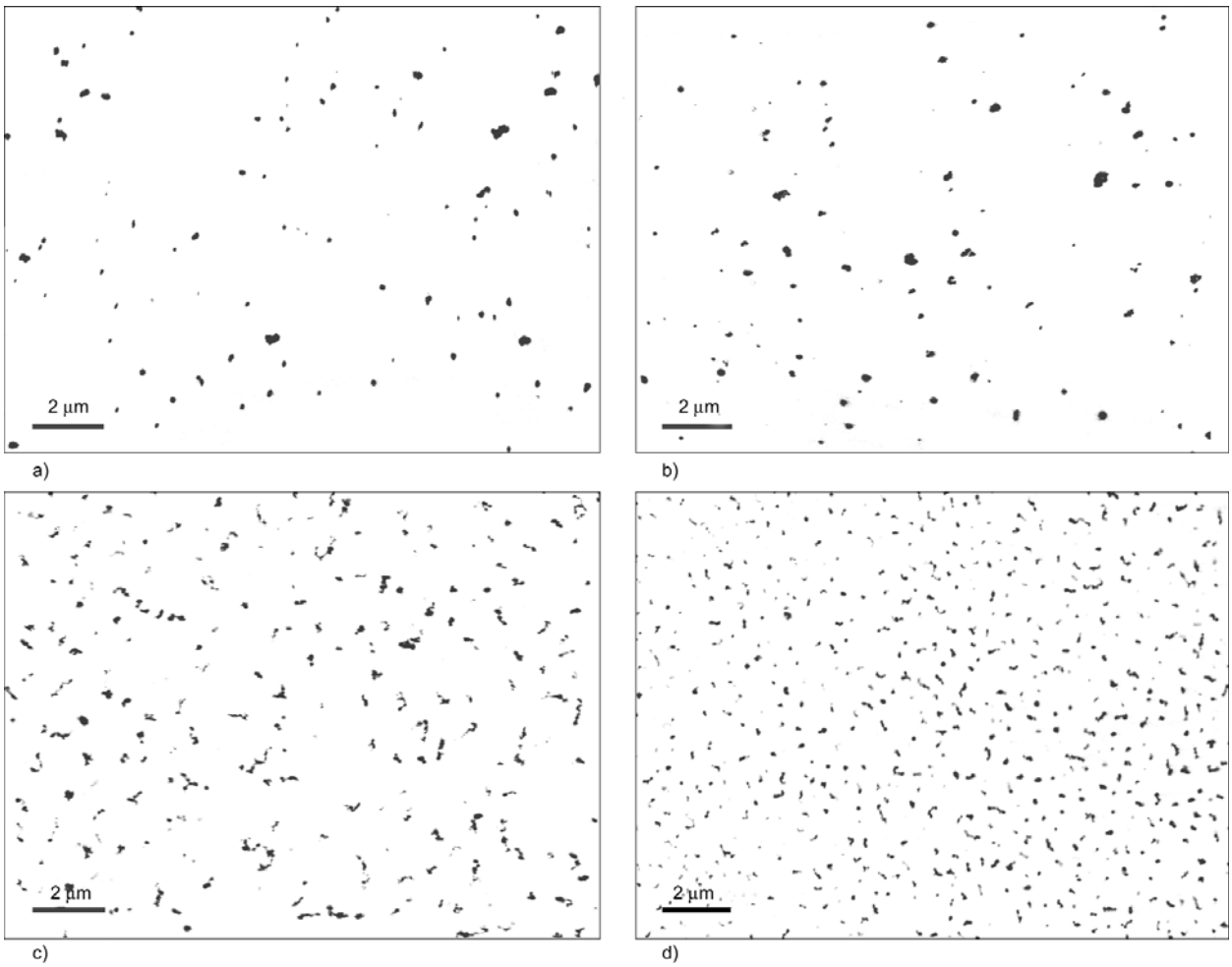

Figure 5. TEM micrographs of nanocomposites PMMA/ZnO – ZnO synthesized in various diols (nano ZnO concentration = 1 wt%): a) BD, b) TEG, c) EG, d) PD

three degradation peaks at 270, 330 and 370°C, which can be explained by the degradation of pure PMMA studied in nitrogen atmosphere [56]. When the temperature is increased from room temperature to 600°C [56], there are three steps: the first one is degradation of head to head linkages between 140 and 180°C, the second one is scission of vinylidene double bonds between 200 and 300°C, and the last step is random scission of the PMMA chain between 300 and 380°C. Our measurements were done in air, and it is known that oxygen stabilizes radicals below 300°C (i.e. shifts degradation peaks to higher temperatures). Therefore degradation peaks in air are in the narrower temperature region, but for the assignment of degradation peaks the results obtained in N_2 are still useful. DTG curves of ZnO/PMMA nanocomposites (Figure 6a and b) show much less intense peaks of vinylidene double bond degradation between 200 and 300°C and a stronger peak of random scission of the PMMA chain above 300°C compared to pure PMMA. It is evident that thermal stabilization is in correlation with the particle size: ZnO with particle size below 50 nm (Figure 6a C and D) shows more intense thermal stabilization compared to ZnO with particle size above 50 nm (Figure 6a A and B) and shifts of 5 and 20% weight loss decomposition temperatures, observed in TGA curves (Table 3), support this conclusion. This can be attributed to the higher specific surface of ZnO with smaller average particle size causing stronger interaction with the PMMA matrix. The degradation peak of vinylidene double bonds reduces significantly with the increase of nano ZnO content (Figure 6b), indicating that their concentration may be reduced. Actually, it is reported in the literature that nano ZnO significantly reduces the vinylidene double bond concentration in PMMA [54, 57]. DTG curves of samples with various concentrations of ZnO show that 1 wt% of ZnO is necessary to significantly change the degradation mechanism and to shift the degradation of PMMA towards higher temperatures (Figure 6b). Many authors report that relatively low filler loading (1%) causes considerable temperature stabilization. Such low filler loadings can be explained by the large specific surface area of the ZnO nanofiller and by the lower concentration of vinylidene double bonds.

The most interesting property of ZnO from the viewpoint of its application in polymers is its extremely efficient absorption in the UV region because of its wide direct band gap of 3.37 eV [58]. The addition of nano ZnO results in substantial UV

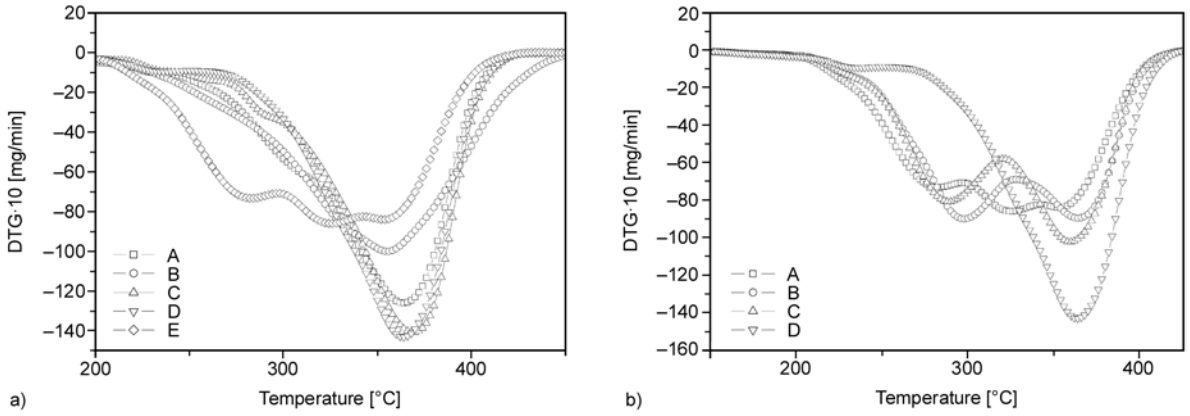

Figure 6. DTG curves of ZnO/PMMA nanocomposites: a) as a function of ZnO particle size (1 wt% ZnO) A) 86 nm, B) 72 nm, C) 32 nm, D) 33 nm, E) PMMA; b) as a function of ZnO concentration (ZnO – 33 nm): A) PMMA, B) 0.01 wt%, C) 0.1 wt % ZnO, D) 1.0 wt% ZnO

Table 3. Decomposition temperatures (T_d – 5% weight loss and T_d – 20% weight loss) in dependence on ZnO particle size (concentration of nano ZnO = 1 wt%)

Sample designation	Particle size [nm]	T_d – 5% weight loss [°C]	T_d – 20% weight loss [°C]
PMMA	–	243	276
ZnO (TEG)/PMMA	86	246	284
ZnO (BD)/PMMA	72	254	298
ZnO (EG)/PMMA	32	264	316
ZnO (PD)/PMMA	33	274	322

Table 4. UV transmittance of ZnO/PMMA nanocomposites (thickness of the plates is 1.5 mm – Procedure A) in dependence on ZnO concentration and particle size

Particle size [nm]	ZnO [wt%]	Transmittance at different wavelengths in the UV region				
		290 nm	300 nm	320 nm	340 nm	360 nm
71.7	1.0	0.054	0.243	0.219	0.118	0.105
	0.1	0.127	0.098	0.178	0.033	0.084
	0.01	6.645	8.880	9.501	10.494	11.147
86.2	1.0	0.075	0.103	0.180	0.135	0.143
	0.1	0.100	0.031	0.210	0.103	0.244
	0.01	8.266	11.592	12.914	14.219	14.844
33.3	1.0	0.072	0.152	0.134	0.043	0.208
	0.1	0.508	0.512	1.196	1.577	1.271
	0.01	4.484	6.862	9.745	10.946	11.708
32.1	1.0	0.298	0.401	0.364	0.166	0.296
	0.1	3.312	5.749	9.541	10.501	9.940
	0.01	4.592	5.852	7.813	8.789	9.515

absorption of PMMA/ZnO nanocomposites and therefore enhances the UV resistance of such materials [35, 42, 59, 60]. Transmittances at various UV wavelengths for ZnO/PMMA nanocomposites are summarized in Table 3. UV absorption of ZnO/PMMA is very high in the wavelength region between 290 and 370 nm: 98 % of the incident UV light is absorbed by 0.1 or 1% of nano ZnO in the composite (Table 4). Even at a very low concentration (0.01%) of nano ZnO, UV absorption is still between 60 and 90% of the incident UV light intensity, depending on the ZnO particle size.

Due to the application aspect we focused on the preparation of a PMMA nanocomposite with high UV opacity (absorption) and with optimal visible transparency, using the unmodified as-synthesized nano ZnO with the smallest particle sizes (ZnO EG 32 nm; ZnO PD 33 nm) to reduce their optical scattering. Measured hydrodynamic radii (Table 2) show that even aggregates formed by 4–8 ZnO particles of these two ZnO samples have sizes close to 100 nm at ZnO concentration of 0.01 wt%. For the preparation of larger PMMA sheets (15×20 cm) we used the prepolymer procedure which is used industrially because it gives a product with excellent optical transparency [61]. Its purpose is to reduce the shrinking during the polymerization of MMA, thus preventing the formation of bubbles in the PMMA sheet. In order to additionally slow down the reagglomeration of ZnO particles after the sonication the concentration of nano ZnO was reduced to 0.05 wt%. Surprisingly, UV absorption of these samples did not deteriorate, while their visible transparency was substantially enhanced (Figure 7a and b). The influence of particle size on the UV-VIS absorption properties can be demonstrated by comparing the UV-VIS spectra of submicrometer ZnO (350 nm) composite (Figure 7a A and Figure 7b A) with those of nano ZnO (32 or 33 nm) composite (Figure 7a B and Figure 7b B). Submicrometer ZnO composite

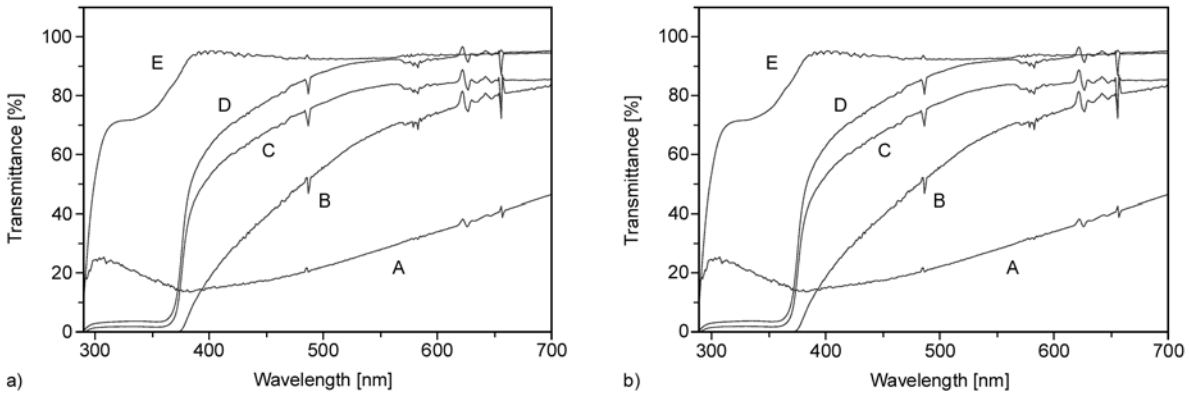

Figure 7. UV-VIS spectra of PMMA/ZnO nanocomposites in dependence of ZnO concentration and nanocomposite preparation procedure: a) ZnO synthesized in EG A) submicrometer (350 nm) ZnO 0.1% – procedure B, B) 0.1% – procedure B, C) 0.05% – procedure B, D) 0.05% – procedure C, E) pure PMMA; b) ZnO synthesized in PD A) submicrometer (350 nm) ZnO 0.1% – procedure B, B) 0.1% – procedure B, C) 0.05% – procedure B, D) 0.05% – procedure C, E) pure PMMA

shows reduced absorption in the UV region and poor transparency for visible light compared to the nano ZnO composite.

TEM micrographs of PMMA/ZnO nanocomposites prepared by the prepolymer procedure show homogeneously distributed ZnO particles with particle sizes up to 100 nm and only a few agglomerates with sizes between 100 and 300 nm (Figure 8). Rather low number of particles in TEM micrographs (Figure 8a and b) may cause doubts about the high UV absorption of these nanocomposites. The particles in Figure 8b were counted and there were 106 particles or agglomerates in a 100 nm thick section. Considering that the thickness of nanocomposite plate is 3.5 mm, and assuming that nano ZnO is uniformly distributed in PMMA matrix, this number should be multiplied with $3.5 \cdot 10^4$ to get the number of particles through the entire cross-section of the plate, giving the final particle number of $3.7 \cdot 10^6$. This is a very large number and therefore the probability that a photon of UV light hits or interacts with a ZnO particle is very high, explaining thus the very high UV absorption at rather low concentrations of nano ZnO.

The aggregation of nano ZnO particles was additionally reduced using sonication through the entire prepolymer synthesis (Procedure C). Sonication is very effective in breaking up the ZnO aggregates. After the sonication is stopped, ZnO particles can not reagglomerate again due to entrapment in PMMA chains. UV-VIS spectra of these samples (Figures 7a D and Figures 7b D) confirm that these materials are optically transparent with slightly yellowish color as a consequence of some optical scattering due to the presence of small amounts of larger agglomerates. Such materials have potential application as UV opaque or UV stabilized transparent PMMA sheets.

PMMA materials are often used in various outdoor applications in which they are exposed to high loads of sunlight. In such conditions the colorless transparent materials change their color to yellow or brown, and even their mechanical properties are deteriorated. We tested the resistance of the nanocomposites to sunlight by the Sun test (Table 5). Differences in ΔE values indicate a significant enhancement of ZnO/PMMA resistance to sunlight compared to pure PMMA. The color change (yellowing) is a consequence of the photodegradation of PMMA chains. There are two possible mechamisms which contribute to the reduction of yellowing in PMMA/ZnO nanocomposites. The first one is the high UV absorption of nano ZnO causing less UV light to penetrate into the material and causing degradation of PMMA. The second one is that nano ZnO causes changes in the chemical structure of PMMA (lower concentration of vinylidene chain end double bonds),

Table 5. Resistance to sunlight (Sun test) in dependence of nano ZnO concentration: ZnO (EG – 32 nm and PD – 33 nm)

Sample designation	ZnO [wt%]	ΔE[a]
PMMA	0	10.6–10.8
ZnO (PD)/PMMA	0.05	3.1–4.6
ZnO (PD)/PMMA	0.1	0.6–0.9
ZnO (EG)/PMMA	0.05	4.1–4.3
ZnO (EG)/PMMA	0.1	1.7–2.1

[a]Δ*E* is colour change measured by colorimeter relatively to the unexposed sample

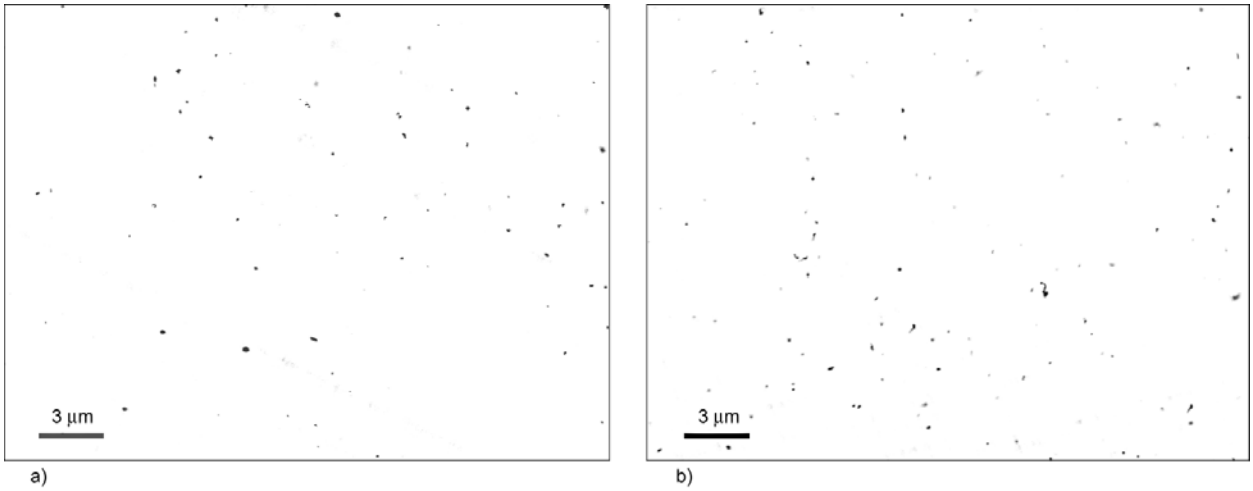

Figure 8. TEM micrographs of PMMA/ZnO nanocomposite prepared by the prepolymer procedure (procedure B) (ZnO concentration = 0.1%): a) ZnO (PD – 33 nm), b) ZnO (EG – 32 nm)

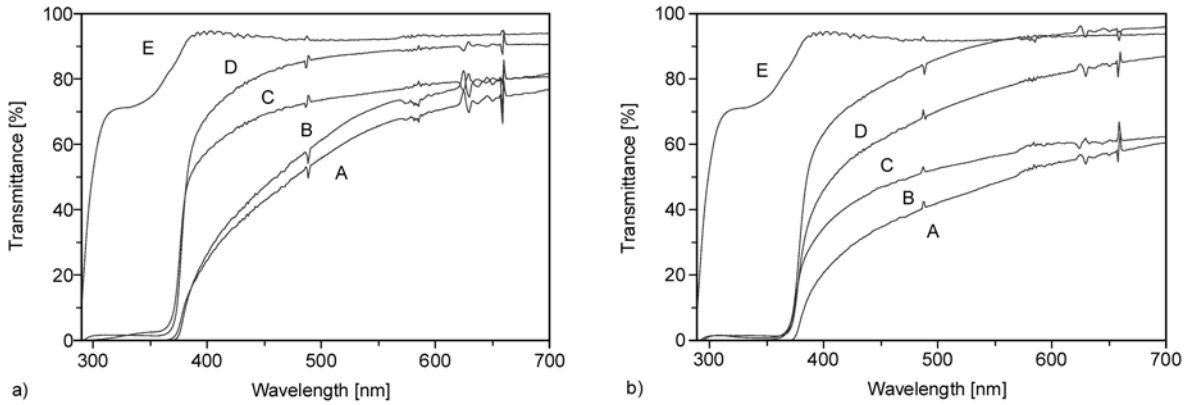

Figure 9. UV-VIS spectra of ZnO/ PMMAnanocomposites exposed to sun test compared to unexposed samples in dependence of ZnO concentration: a) ZnO (EG – 32 nm), b) ZnO (PD – 33 nm): A) 0.1 wt% ZnO unexposed sample, B) 0.1 wt% ZnO, C) 0.05 wt% ZnO unexposed sample, D) 0.05 .% ZnO, E) pure PMMA

if MMA is polymerized in its presence [30, 33]. Vinylidene double bonds are weak points where the photodegradation of PMMA starts and their lower concentration in PMMA chains means that such material is more resistant to photodegradation.

UV-VIS spectra of PMMA/ZnO nanocomposites exposed to the sun test show a small decrease in visible transparency due to color change during the sun test (Figure 9). It can be also seen that ZnO particles synthesized in PD (Figure 9b) showed higher protection to sunlight than those synthesized in EG (Figure 9a) and that protection is more effective at higher ZnO concentration (0.1 wt%), as expected. These results indicate the high potential of these materials in applications with high exposure to sunlight.

Preparation of ZnO/PMMA nanocomposites has attracted considerable attention in the last seven years. Most authors studied the preparation of ZnO/PMMA nanocomposites in the form of thin films from the solution [36, 54, 58–60, 62]. In our case we used unmodified ZnO for the preparation of nanocomposites. Synthesized ZnO is organophilic due to the presence of organometallic intermediates and solvent (diol) residues on the particle surface. The synthetic procedure of ZnO filler preparation is quite simple and also easy to transfer to a pilot level. We used an industrially used prepolymer procedure for the preparation of 3.5 mm thick nanocomposite plates. Due to the absence of additional surface modification the highest nano ZnO concentration to obtain transparent materials is rather low (0.05–0.1 wt%) but we showed that even in this concentration range UV absorption (above 95%) and protection from sunlight are very high. The absence of surfactants is an advantage because they can change other properties of these materials (e.g. mechanical properties, sunlight stability), making them unsuitable for outdoor applications. UV absorption and sunlight resistance as well as thermal stability are additionally improved at nano ZnO concentrations higher than 0.1 wt% where visible transparency becomes rather poor. Such nanocomposites can be applied for various nontransparent PMMA materials such as aluminium hydroxide filled PMMA or other highly filled PMMA materials.

4. Conclusions

Nano ZnO particles have been synthesized by the polyol method in various diols (EG, PD, BD and TEG) with and without p-TsOH as an end capping agent. The addition of p-TsOH reduces the average particle size and increases the ZnO crystallinity as compared to ZnO prepared without p-TsOH. Particle sizes of nano ZnO particles, prepared in various diols, are in correlation with the diol chain length. With increased diol chain length the average particle size of ZnO is also increased (EG 32 nm, PD 33 nm, BD 72 nm, TEG 86 nm). Zn(II) acetate hydrolysis in diols proceeds through the $Zn_4O(CH_3COO)_6$ reaction intermediate as supported by FTIR and ^{13}C NMR spectroscopy.

Unmodified as-synthesized nano ZnO powders were used for the preparation of PMMA nanocomposites. Dispersions of ZnO particles in the monomer, MMA, in the concentration range between 0.01 and 0.1 wt% are stable for at least 45 min, although they form agglomerates consisting of two to six parti-

cles. TEM micrographs of nanocomposites also show small agglomerates of ZnO nanoparticles homogeneously distributed in the PMMA matrix, thus confirming the results of DLS measurements.

ZnO nanoparticles thermally stabilize the PMMA matrix by shifting its 5% weight loss degradation temperature from 10 to 30 °C towards higher temperatures in dependence on the particle size. ZnO with smaller average particle sizes show a more intense stabilization effect. Thermal stabilization of nanocomposites is dependent on the ZnO concentration: the addition of 1 wt% of ZnO shifts 5% weight loss degradation temperature by 30°C to higher temperatures, while at lower ZnO concentrations shifts are rather small.

ZnO/PMMA nanocomposites exhibit excellent absorption of UV light in the region between 290 and 370 nm even at concentrations of only 0.05 wt% of nano ZnO. The transmittance of the visible light was optimized by reducing the ZnO concentration and by modifying the nanocomposite preparation procedure. Nanocomposites with efficient UV absorption and high visible light transmittance were prepared by the prepolymer procedure using constant sonication during the prepolymer synthesis at ZnO concentrations between 0.05 and 0.1 wt%. Nano ZnO significantly enhances the resistance to sunlight depending on the concentration of ZnO, thus giving these materials high potential in various applications with high UV and sunlight loads.

Acknowledgements

The financial support of Slovenian Ministry of Higher Education, Science and Technology, Slovenian Research Agency and EU Research Agency through research programmes P2-0145, P2-030 and Novapol ERA-NET MNT project is gratefully acknowledged. The authors thank Andrej Beličič, M.Sc., of the Kolpa company for the Sun test measurements and Igor Djerdj, Ph.D., of the Rudjer Boskovic institute for HR TEM microscopy.

References

[1] Xie W., Yang Z., Chun H.: Catalytic properties of lithium-doped ZnO catalysts used for biodiesel preparations. Industrial and Engineering Chemistry Research, **46**, 7942–7949 (2007).
DOI: 10.1021/ie070597s

[2] Hoffman A. J., Yee H., Mills G., Hoffmann M. R.: Photoinitiated polymerization of methyl methacrylate using Q-sized ZnO colloids. Journal of Physical Chemistry, **23**, 5540–5546 (1992).
DOI: 10.1002/chin.199240085

[3] Rout C. S., Raju A. R., Govindaraj A., Rao C. N. R.: Ethanol and hydrogen sensors based on ZnO nanoparticles and nanowires. Journal of Nanoscience and Nanotechnology, **7**, 1923–1929 (2007).
DOI: 10.1166/jnn.2007.742

[4] Rout C. S., Hedge M., Govindaraj A., Rao C. N. R.: Ammonia sensors based on metal oxide nanostructures. Nanotechnology, **18**, 205504/1–205504/9 (2007).
DOI: 10.1088/0957-4484/18/20/205504

[5] Ayudhya S. K. N., Tonto P., Mekasuwandumrog O., Pavarajarn V., Praserthdam P.: Solvothermal synthesis of ZnO with various aspect ratios using organic solvents. Crystal Growth and Design, **6**, 2446–2450 (2006).
DOI: 10.1021/cg050345z

[6] Zhang J., Sun L., Yin J., Su H., Liao C., Yan C.: Control of ZnO morphology via a simple solution route. Chemistry of Materials, **14**, 4172–4177 (2002).
DOI: 10.1021/cm020077h

[7] Peiró A. M., Ravirajan P., Govender K., Boyle D. S., O'Brien P., Bradley D. D. C., Nelson J., Durrant J. R.: Hybrid polymer/metal oxide solar cells based on ZnO columnar structures. Journal of Materials Chemistry, **16**, 2088–2096 (2006).
DOI: 10.1039/b602084d

[8] Lin C-C., Lee W-S., Sun C-C., Whu W-H.: A varistor–polymer composite with nonlinear electrical-thermal switching properties. Ceramics International, **34**, 131–136 (2008).
DOI: 10.1016/j.ceramint.2006.09.018

[9] Pal U., Serrano J. G., Santiago P., Xiong G., Ucer K. B., Williams R. T.: Synthesis and optical properties of ZnO nanostructures with different morphologies. Optical Materials, **29**, 65–69 (2006).
DOI: 10.1016/j.optmat.2006.03.015

[10] Liu D-P., Li G-D., Su Y., Chen J-S.: Highly luminescent ZnO nanocrystals stabilized by ionic-liquid components. Angewandte Chemie, International Edition, **45**, 7370–7373 (2006).
DOI: 10.1002/anie.200602429

[11] Schwartz D. A., Norberg N. S., Nguyen Q. P., Parker J. M., Gamelin D. R.: Magnetic quantum dots: Synthesis, spectroscopy, and magnetism of Co^{2+}- and Ni^{2+}-doped ZnO nanocrystals. Journal of the American Chemical Society, **125**, 13205–13218 (2003).
DOI: 10.1021/ja036811v

[12] Hu Y., Jiang Z., Xu C., Mei T., Guo J., White T.: Monodisperse ZnO nanodots: Synthesis, charaterization, and optoelectronic properties. Journal of Physical Chemistry, **111**, 9757–9760, (2007).
DOI: 10.1021/jp0726384

[13] Ghoshal T., Kar S., Chaudhuri S.: ZnO doughnuts: Controlled synthesis, growth mechanism, and optical properties. Crystal Growth and Design, **7**, 136–141 (2007).
DOI: 10.1021/cg060289h

[14] Demir M. M., Muñoz-Espí R., Lieberwirth I., Wegner G.: Precipitation of monodisperse ZnO nanocrystals via acid-catalyzed esterification of zinc acetate. Journal of Materials Chemistry, **16**, 2940–2947 (2006). DOI: 10.1039/b601451h

[15] Bitenc M., Dražić G., Orel Z. C.: Characterization of crystalline zinc oxide in the form of hexagonal bipods. Crystal Growth and Design, **10**, 830–837 (2010). DOI: 10.1021/cg901193g

[16] Ambrožič G., Djerdj I., Škapin S. D., Žigon M., Orel Z. C.: The double role of p-toluenesulfonic acid in the formation of ZnO particles with different morphologies. CrystEngComm, **12**, 1862–1868 (2010). DOI: 10.1039/b924412n

[17] Liu B., Zeng H. C.: Hydrothermal synthesis of ZnO nanorods in the diameter regime of 50 nm. Journal of the American Chemical Society, **125**, 4430–4431 (2003). DOI: 10.1021/ja0299452

[18] Sun X. M., Chen X., Deng Z. X., Li Y. D.: A CTAB-assisted hydrothermal orientation growth of ZnO nanorods. Materials Chemistry and Physics, **78**, 99–104 (2003). DOI: 10.1016/S0254-0584(02)00310-3

[19] Bitenc M., Podbrščček P., Orel Z. C., Cleveland M. A., Paramo J. A., Peters R. M., Strzhemecny Y. M.: Correlation between morphology and defect luminescence in precipitated ZnO nanorod powders. Crystal Growth and Design, **9**, 997–1001 (2009). DOI: 10.1021/cg8008078

[20] Yang L., Wang G. Z., Tang C. J., Wang H. Q., Zhang L.: Synthesis and photoluminescence of corn-like ZnO nanostructures under solvothermal-assisted heat treatment. Chemical Physics Letters, **409**, 337–341 (2005). DOI: 10.1016/j.cplett.2005.05.015

[21] Yu S-H., Yang J., Quian Y-T., Yoshimura M.: Optical properties of ZnS nanosheets, ZnO dendrites, and their lamellar precursor $3ZnS{\cdot}(NH_2CH_2CH_2NH_2)_{0.5}$. Chemical Physics Letters, **361**, 362–366 (2002).

[22] Ambrožič G., Škapin S. D., Žigon M., Orel Z. C.: The synthesis of zinc oxide nanoparticles from zinc acetylacetonate hydrate and 1-butanol or isobutanol. Journal of Colloid and Interface Science, **346**, 317–323 (2010). DOI: 10.1016/j.jcis.2010.03.001

[23] Guo L., Ji Y., Xu H.: Regularly shaped, single-crystalline ZnO nanorods with wurtzite structure. Journal of the American Chemical Society, **124**, 14864–14865 (2002). DOI: 10.1021/ja027947g

[24] Mondelaers D., Vanhoyland G., Van den Rul H., D'Haen J., Van Bael M. K., Mullens J., Van Poucke L. C.: Synthesis of ZnO nanopowder via an aqueous acetate-citrate gelation method. Materials Research Bulletin, **37**, 901–914 (2002). DOI: 10.1016/S0025-5408(02)00727-4

[25] Wang Z., Zhang H., Zhang L., Yuan J., Yan S., Wang C.: Low-temperature synthesis of ZnO nanoparticles by solid-state pyrolytic reaction. Nanotechnology, **14**, 11–15 (2003). DOI: 10.1088/0957-4484/14/1/303

[26] Pillai S. C., Kelly J. M., McCormack D. E., O'Brien P. O., Ramesh R.: The effect of processing conditions on varistors prepared from nanocrystalline ZnO. Journal of Materials Chemistry, **13**, 2586–2590 (2003). DOI: 10.1039/B306280E

[27] Masala O., Seshandri R.: Synthesis routes for large volumes of nanoparticles. Annual Review of Materials Research, **34**, 41–81 (2004). DOI: 10.1146/annurev.matsci.34.052803.090949

[28] Feng X., Hu M. Z.: Ceramic nanoparticle synthesis. in 'Encyclopaedia of nanoscience and nanotechnology' (ed.: Nalwa H. S.) American Scientific Publishers, Stevenson Ranch, Vol 1, 687–726 (2004).

[29] Jézéquel D., Guenot J., Jouini N., Fiévet F.: Submicrometer zinc-oxide particles – Elaboration in polyol medium and morphological-characteristics. Journal of Materials Research, **1**, 77–83 (1995). DOI: 10.1557/JMR.1995.0077

[30] Seelig E. W., Tang B., Yamilov A., Cao H., Chang R. P. H.: Self-assembled 3D photonic crystals from ZnO colloidal spheres. Materials Chemistry and Physics, **80**, 257–263 (2003). DOI: 10.1016/S0254-0584(02)00492-3

[31] Anžlovar A., Crnjak Orel Z., Žigon M.: Morphology and particle size of di(ethylene glycol) mediated metallic copper nanoparticles. Journal of Nanoscience and Nanotechnology, **8**, 3516–3525 (2008). DOI: 10.1166/jnn.2008.165

[32] Demir M. M., Memesa M., Castignolles P., Wegner G.: PMMA/zinc oxide nanocomposites prepared by in-situ bulk polymerization. Macromolecular Rapid Communications, **27**, 763–770 (2006). DOI: 10.1002/marc.200500870

[33] Muñoz-Espí R., Jeschke G., Lieberwirth I., Gómez C. M., Wegner G.: ZnO–latex hybrids obtained by polymer-controlled crystallization: A spectroscopic investigation. Journal of Physical Chemistry B, **111**, 697–707 (2007). DOI: 10.1021/jp066380d

[34] Golovko D. S., Muñoz-Espí R., Wegner G.: Interaction between poly(styrene–acrylic acid) latex nanoparticles and zinc oxide surfaces. Langmuir, **23**, 3566–3569 (2007). DOI: 10.1021/la0632880

[35] Kickelbick G.: Concepts for the incorporation of inorganic building blocks into organic polymers on a nanoscale. Progress in Polymer Science, **28**, 83–114 (2003). DOI: 10.1016/S0079-6700(02)00019-9

[36] Khrenov V., Klapper M., Müllen K.: Surface functionalized ZnO particles designed for the use in transparent nanocomposites. Macromolecular Chemistry and Physics, **206**, 95–101 (2005).
DOI: 10.1002/macp.200400213

[37] Khrenov V., Schwager F., Klapper M., Koch M., Müllen K.: Compatibilization of inorganic particles for polymeric nanocomposites. Optimization of the size and the compatibility of ZnO particles. Polymer Bulletin, **58**, 799–807 (2007).
DOI: 10.1007/s00289-006-0721-1

[38] Hong R. Y., Quian J. Z., Cao J. X.: Synthesis and characterization of PMMA grafted ZnO nanoparticles. Powder Technology, **163**, 160–168 (2006).
DOI: 10.1016/j.powtec.2006.01.015

[39] Tang E. J., Cheung G. X., Ma X. L.: Preparation of nano-ZnO/PMMA composite particles via grafting of the copolymer onto the surface of zinc oxide nanoparticles. Powder Technology, **161**, 209–214 (2006).
DOI: 10.1016/j.powtec.2005.10.007

[40] Tang E. J., Chung G. X., Pang X. S., Ma X. L., Xing F. B.: Synthesis of nano-ZnO/poly(methyl methacrylate) composite microsphere through emulsion polymerization and its UV-shielding property. Colloid and Polymer Science, **284**, 422–428 (2006).
DOI: 10.1007/s00396-005-1389-z

[41] Liu P., Su Z.: Preparation and characterization of PMMA/ZnO nanocomposites via in-situ polymerization method. Journal of Macromolecular Science: Physics, **45**, 131–138 (2006).
DOI: 10.1080/00222340500408085

[42] Yu H. Y., Du J., Gu J. S., Guan M. Y., Wu Z. C., Ling Q., Sun Y. M.: Chemical modification on the surface of nano-particles of ZnO and its characterization (in Chinese). Spectroscopy and Spectral Analysis, **24**, 177–179 (2004).

[43] Shim J-W., Kim J-W., Han S-H., Chang I-S., Kim H-K., Kang H-H., Lee O-S., Suh K-D.: Zinc oxide/polymethylmethacrylate composite microspheres by in situ suspension polymerization and their morphological study. Colloids and Surfaces A: Physicochemical and Engineering Aspects, **207**, 105–111 (2002).
DOI: 10.1016/S0927-7757(02)00044-4

[44] Tasbihi M., Lavrenčič Štangar U., Černigoj U., Kogej K.: Low-temperature synthesis and characterization of anatase TiO_2 powders from inorganic precursors. Photochemical and Photobiological Sciences, **8**, 719–725 (2009).
DOI: 10.1039/b817472e

[45] Heller R. B., McGannon J., Weber A. H.: Precision determination of the lattice constants of zinc oxide. Journal of Applied Physics, **21**, 1283–1284 (1950).
DOI: 10.1063/1.1699591

[46] Sinha A., Sharma B. P.: Preparation of copper powder by glycerol process. Materials Research Bulletin, **37**, 407–416 (2002).
DOI: 10.1016/S0025-5408(01)00819-4

[47] Hayashi S., Nakamori N., Kanamori H.: Generalized theory of average dielectric constant and its application to infrared absorption by ZnO small particles. Journal of the Physical Society of Japan, **46**, 176–183 (1979).
DOI: 10.1143/JPSJ.46.176

[48] Johnson M. K., Powell D. B., Cannon R. D.: Vibrational-spectra of carboxylato complexes. 1. Infrared and Raman-spectra of berrylium(II) acetate and formate and of zinc(II) acetate and zinc(II) acetate dihydrate. Spectrochimica Acta, **37**, 899–904 (1981).
DOI: 10.1016/0584-8539(81)80011-6

[49] Johnson M. K., Powell D. B., Cannon R. D.: Vibrational spectra of carboxylato complexes–II. Some oxotetranuclear complexes. Spectrochimica Acta, **38**, 125–131 (1982).
DOI: 10.1016/0584-8539(82)80187-6

[50] Berkesi O., Dreveni I., Körtvélyesi T., Andor J. A., Mink J., Goggin P. L.: Influence of the alkyl-chain on the symmetry and structural changes of $Zn_4O(RCO_2)_6$ complexes in film phase – An FT-IR study. Vibrational Spectroscopy, **43**, 227-236 (2007).
DOI: 10.1016/j.vibspec.2006.08.002

[51] Schmidt T., Müller G., Spanhel L., Kerkel K., Forchel A.: Activation of 1.54 μm Er^{3+} fluorescence in concentrated II–VI semiconductor cluster environments. Chemistry of Materials, **10**, 65–71 (1998).
DOI: 10.1021/cm9702169

[52] Dreveni I., Berkesi O., Janovics I., Andor J. A., Mink J.: Fourier transform infrared spectroscopic study on the molecular structure of bis(butanoato) zinc(II) and μ_4-oxohexa-μ-butanoatotetrazinc(II) complexes. Vibrational Spectroscopy, **2**, 205–209 (1991).
DOI: 10.1016/0924-2031(91)85027-K

[53] Koshevar V. D.: The influence of poly(methyl methacrylate) on the stability of zinc oxide dispersions in nonaqueous media of various acidity. Colloid Journal of the Russian Academy of Sciences, **57**, 649–652 (1995).

[54] Demir M. M., Castignolles P., Akbey Ü., Wegner G.: In-situ bulk polymerization of dilute particle/MMA dispersions. Macromolecules, **40**, 4190–4198 (2007).
DOI: 10.1021/ma070142e

[55] Ding Y., Gui Z., Zhu J., Wang Z., Hu Y., Song L.: Poly(methyl methacrylate)–nanoribbon nanocomposites with high thermal stability and improvement in the glass-transition temperature. Journal of Materials Research, **22**, 3316–3323 (2007).
DOI: 10.1557/JMR.2007.0427

[56] Kashiwagi T., Inaba A., Brown J. E., Hatada K., Kitayama T., Masuda E.: Effects of weak linkages on the thermal and oxidative degradation of poly(methyl methacrylates). Macromolecules, **19**, 2160–2168 (1986).
DOI: 10.1021/ma00162a010

[57] Anžlovar A., Crnjak Orel Z., Žigon M.: Poly(methyl methacrylate) composites prepared by in situ polymerization using organophillic nano-to-submicrometer zinc oxide particles. European Polymer Journal, **46**, 1216–1224 (2010).
DOI: 10.1016/j.eurpolymj.2010.03.010

[58] Miyazaki H., Teranishi Y., Ota T.: Fabrication of UV-opaque and visible-transparent composite film. Solar Energy Materials and Solar Cells, **90**, 2640–2646 (2006).
DOI: 10.1016/j.solmat.2006.02.030

[59] Demir M. M., Koynov K., Akbey Ü., Bubeck C., Park I., Lieberwirth I., Wegner G.: Optical properties of composites of PMMA and surface-modified zincite nanoparticles. Macromolecules, **40**, 1089–1100 (2007).
DOI: 10.1021/ma062184t

[60] Sun D., Miyatake N., Sue H-J.: Transparent PMMA/ZnO nanocomposite films based on colloidal ZnO quantum dots. Nanotechnology, **18**, 215606/1–215606/6 (2007).
DOI: 10.1088/0957-4484/18/21/215606

[61] Slone R. V.: Methacrylic polymers. in 'Kirk-Othmer encyclopedia of chemical technology' Wiley, New York, Vol 16, 271–298 (2005).
DOI: 10.1002/ 0471238961.1305200814152201.a01.pub2

[62] Xiong M., Gu G., You B., Wu L.: Preparation and characterization of poly(styrene butylacrylate) latex/nano-ZnO nanocomposites. Journal of Applied Polymer Science, **90**, 1923–1931 (2003).
DOI: 10.1002/app.12869

eXPRESS Polymer Letters Vol.5, No.7 (2011) 620–634
Available online at www.expresspolymlett.com
DOI: 10.3144/expresspolymlett.2011.60

Isolation and recovery of microbial polyhydroxyalkanoates

*B. Kunasundari, K. Sudesh**

Ecobiomaterial Research Laboratory, School of Biological Sciences, Universiti Sains Malaysia, 11800 Penang, Malaysia

Received 17 November 2010; accepted in revised form 18 January 2011

Abstract. The deleterious environmental impacts caused by plastic wastes have attracted worldwide concern. The bio-based and biodegradable polyhydroxyalkanoate (PHA) appears to be one of the potential candidates to replace some conventional plastics. However, high production cost of PHAs has limited their market penetration. The major cost absorbing factors are the upstream fermentation processes and the downstream PHA recovery technologies. The latter significantly affects the overall process economics. Various recovery technologies have been proposed and studied in small scales in the laboratory as well as in industrial scales. These include solvent extraction, chemical digestion, enzymatic treatment and mechanical disruption, supercritical fluid disruption, flotation techniques, use of gamma irradiation and aqueous two-phase system. This paper reviews all the recovery methods known to date and compares their efficiency and the quality of the resulting PHA. Some of the large-scale production of PHA and the strategies employed to reduce the production cost are also discussed.

Keywords: *biodegradable polymers, polyhydroxyalkanoate, recovery, microorganism*

1. Introduction

The versatility of plastic materials in terms of mechanical properties and durability has been manipulated by mankind to enhance quality of life without realizing they have become increasingly ubiquitous. The world's plastics production was estimated to be 260 million tonnes in 2007 [1]. It is clear from this figure that the long term deleterious environmental impacts caused by plastics were entirely overlooked and this in turn poses greater difficulties for plastic waste disposal. Therefore, the development and use of biodegradable plastics is gaining more serious attention. The most extensively studied thermoplastic biopolymers are the polyhydroxyalkanoates (PHA) and polylactic acid (PLA) [2]. PHA is attractive because of its biodegradability and physical properties that closely resemble some conventional plastics such as polypropylene (PP) and low-density polyethylene (LDPE) [3]. In addition, because of the diverse types of monomers (about 150 different structures), it is possible to produce PHA copolymers having a wide range of properties. The various PHA monomers can be classified based on the number of carbon atoms as short-chain length PHA (scl-PHA), medium-chain length PHA (mcl-PHA) and long-chain length PHA (lcl-PHA). Scl-PHA refers to PHA comprised of monomers having 5 or less carbon atoms. These include 3-hydroxybutyrate and 3-hydroxyvalerate. The mcl-PHA is comprised of monomers having 6 to 14 carbon atoms. These include 3-hydroxyhexanoate, 3-octanoate and 3-hydroxydecanoate. The lcl-PHA, which is uncommon and least studied, consists of monomers with more than 14 carbon atoms. Recently, it has also been made possible to synthesize a new type of PHA containing lactide as a co-monomer [4–6]. All these developments indicate that PHA may become the preferred next generation bioplastic. However, to date the market penetration of PHA is still scarce. This is mainly due to

*Corresponding author, e-mail: ksudesh@usm.my

its high production cost. The main reasons behind the economic disadvantages are the costly fermentation and purification technologies. The latter significantly affects the overall process economics. Much work has been carried out to lower the PHA production cost by the use of effective and inexpensive carbon source and genetically engineered microorganisms. Sugars have been shown to be an effective feedstock for PHA production in Brazil, especially when the PHA production is integrated to the sugarcane-processing factory [7]. On the other hand, it has been demonstrated that vegetable oils are also potential feedstock for PHA production [8–12] in countries like Malaysia where palm oil is produced in very large scales. High levels of PHA accumulation have been achieved using crude palm kernel oil. The yield of PHA from vegetable oils is at least two times the yield of PHA from sugars [13]. However, the real cost associated with PHA would only diminish with the development of a cheaper and environmentally friendly PHA recovery method. This article reviews the currently known methods for the recovery of PHA. Some of the large-scale production of PHA and the strategies employed to reduce the production cost are also discussed.

2. PHA biosynthesis

PHA is a lipid-like compound synthesized by many microorganisms as a form of storage material. Upon

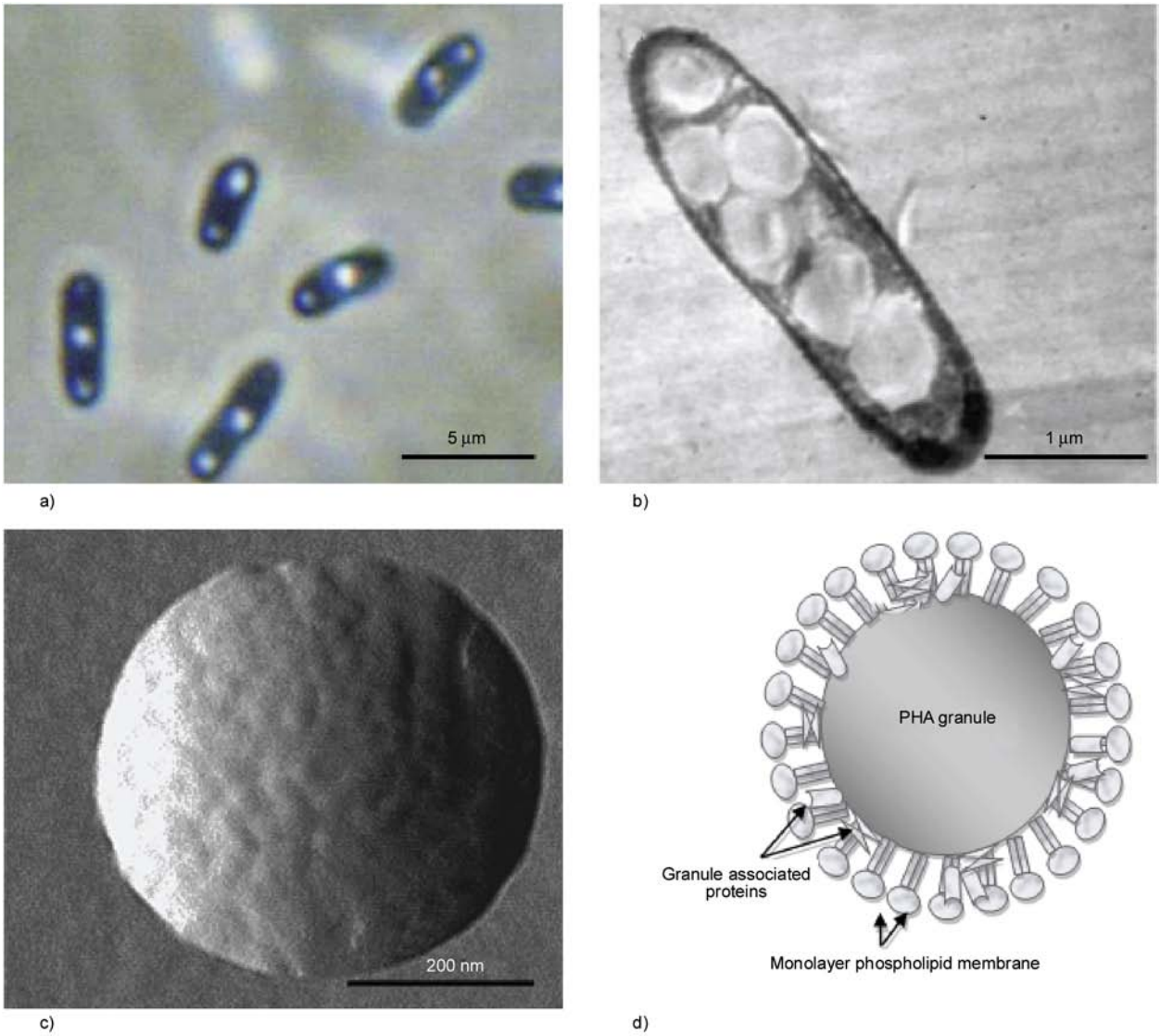

Figure 1. Morphology of PHA granules in the bacterial cells observed under (a) Phase contrast and (b) Transmission Electron Microscope. (c) Atomic force microscope deflection image showing the presence of globular particles on the granule surface. (d) A model representing the native PHA granule with a protein monolayer on the surface (Not drawn according to actual scale)

synthesis, PHA is accumulated in the form of granules in the bacterial cell cytoplasm. The average size of the PHA granules is approximately 0.2–0.5 μm (Figure 1). Figure 1 shows the morphology of PHA granules when observed using various microscopy techniques. Atomic force microscopy analysis has shown the presence of a protein monolayer on the surface of PHA granules [14–15]. In order to recover the PHA granules, it is necessary to rupture the bacterial cell and remove the protein layer that coats the PHA granules. Alternatively, the PHA has to be selectively dissolved in a suitable solvent. Formation of PHA granules is dependent on the presence of suitable metabolic pathways. Figure 2 shows a simplified metabolic pathway for the biosynthesis of poly(3-hydroxybutyrate) [P(3HB)], which is the most common type of PHA. The biosynthesis of P(3HB) is initiated by the condensation of two acetyl-CoA molecules by β-ketothiolase (PhaA) to form acetoacetyl-CoA. Subsequently, NADPH-dependent acetoacetyl-CoA reductase (PhaB) catalyzes the reduction of acetoacetyl-CoA to the (R)-isomer of 3-hydroxybutyryl-CoA which is then polymerized into P(3HB) by the PHA synthase (PhaC) [3]. To date, *Cupriavidus necator* (formerly known as *Wautersia eutropha*, *Ralstonia eutropha* and *Alcaligenes eutrophus*) is the most extensively studied microorganism for the cost-effective production of PHA. Numerous other strains such as *Bacillus cereus* SPV, *Sinorhizobium meliloti*, *Azotobacter chroococcum* G-3, *Pseudomonas putida* KT2440 and *Metylobacterium* sp V49 also gaining attention for the PHA production. Besides wild-type strains, recombinant strains are also being developed. Various types of recombinant *Escherichia coli* strains are able to synthesize PHA to high intracellular level and some are amenable to genetically mediated lysis system to facilitate the release of the PHA granules [16]. Compared to the extensive research on the biosynthesis of PHA, research on the downstream processing of PHA is scarce. Table 1 shows the various extraction methods that have been reported. The following section will describe all these methods and finally compare their advantages and disadvantages (Table 2). This study is important to choose a suitable method that could effectively isolate PHA from the microbial cells.

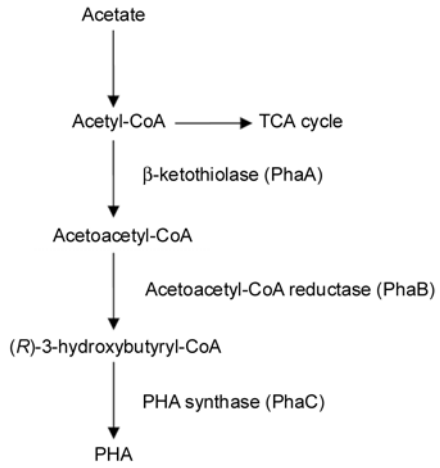

Figure 2. The most studied metabolic pathway for the biosynthesis of polyhydroxyalkanoates (PHA)

3. Recovery techniques for the isolation and purification of PHA from microbial cells

3.1. Solvent extraction

Solvent extraction is the most extensively adopted method to recover PHA from the cell biomass (Table 1). This method is also used routinely in the laboratory because of its simplicity and rapidity. Two main steps are involved, first is the modification of cell membrane permeability thus allowing release and solubilization of PHA. This is then followed by non-solvent precipitation [17]. Extraction of PHA with solvents such as chlorinated hydrocarbons, i.e. chloroform, 1,2-dichloroethane [18] or some cyclic carbonates like ethylene carbonate and 1,2-propylene carbonate [19] is common. Lower chain ketone such as acetone is the most prominent solvent especially for the extraction of mcl-PHA [20]. Precipitation of PHA is commonly induced by non-solvent such as methanol and ethanol [18]. Solvent extraction has undoubted advantages over the other extraction methods of PHA in terms of efficiency. This method is also able to remove bacterial endotoxin and causes negligible degradation to the polymers [17]. So, it is possible to obtain very pure PHA with high molecular weights. Unfortunately, large-scale application of solvent extraction is generally viewed as a method that is not environmentally friendly. In addition, several other factors discourage the use of solvents such as high capital and operational costs. Another problem is the high viscosity of the extracted polymer solution when the P(3HB) concentration exceeds 5% (w/v) (Table 2). The viscosity of the solution interferes with cell debris removal resulting in lengthy separation process. Besides, there is a possibility that solvent

Table 1. Various PHA recovery methods that have been reported

Extraction method	Comments	Strain	Results	Reference
Solvent extraction	Chloroform	*Bacillus cereus* SPV	Purity: 92%; Yield: 31%	Valappil *et al.* [31]
	Chloroform	*Cupriavidus necator* DSM 545	Purity: 95%; Yield: 96%	Fiorese *et al.* [25]
	1,2-Propylene carbonate	*C. necator* DSM 545	Purity: 84%; Yield:95%	Fiorese *et al.* [25]
	Acetone-water process		Yield: 80–85%	Narasimhan *et al.* [65]
	Methyl *tert*-butyl ether	*Pseudomonas putida* KT2440	Yield: 15–17.5 wt%	Wampfler *et al.* [26]
	Methylene chloride	*C. necator*	Purity: 98%	Zinn *et al.* [66]
	Non halogenated solvents-isoamy propionate, propyl butyrate, isoamyl valerat etc.	*C. necator*		Mantelatto and Durao [67]
	Acetone, room temperature	*P. putida* GPo1	Yield: 94%	Elbahloul and Steinbüchel [64]
Digestion method				
Surfactant	SDS	Recombinant *Escherichia coli*	Purity: 99%; Yield:89%	Choi and Lee [54]
	Palmitoyl carnitine	*C. necator*, *Alcaligenes latus*	Degree of lysis: 56–78%	Lee *et al.* [68]
Sodium hypochlorite	Sodium hypochlorite	*C. necator*, Recombinant *E. coli*	Purity: 86%; Purity: 93%	Hahn *et al.* [69]
	Sodium hypochlorite	*C. necator* DSM 545	Purity: 98%	Berger *et al.* [70]
Surfactant-sodium hypochlorite	SDS-Sodium hypochlorite	*Azotobacter chroococcum* G-3	Purity: 98%; Yield: 87%	Dong and Sun [28]
	Triton X-100-sodium hypochlorite	*C. necator* DSM 545	Purity: 98%	Ramsay *et al.* [27]
Surfactant-Chelate	Triton X-100-EDTA	*Sinorhizobium meliloti*	Purity: 68%	Lakshman and Shamala [34]
	Betaine-EDTA disodium salt	*C. necator* DSM 545	Purity: >96%; Yield: 90%	Chen *et al.* [33]
Dispersion of sodium hypochlorite and chloroform	Chloroform- sodium hypochlorite	*B. cereus* SPV	Purity: 95%; Yield: 30%	Valappil *et al.* [31]
	Chloroform- sodium hypochlorite	*C. necator*, Recombinant *E. coli*	Purity: >98%	Hahn *et al.* [69]
Selective dissolution by protons	Sulfuric acid	*C. necator*	Purity: >97%; Yield: > 95%	Yu and Chen [21]
Enzymatic digestion	*Microbispora* sp culture-chloroform	*S. meliloti*	Purity: 94%	Lakshman and Shamala [34]
	Enzyme combined with SDS-EDTA	*P. putida*	Purity: 93%	Kathiraser *et al.* [71]
	Bromelain; pancreatin	*C. necator*	Purity: 89%; Purity: 90%	Kapritchkoff *et al.* [39]
Mechanical disruption	Bead mill	*A. latus*		Tamer *et al.* [23]
	High pressure homogenization	*A. latus*		Tamer *et al.* [23]
	SDS-High pressure homogenization	*Metylobacterium* sp V49	Purity: 95%; Yield: 98%	Ghatnekar *et al.* [48]
	Sonication	Baci*llus flexus*	Purity: 92%; Yield: 20%	Divyashree *et al.* [37]
Supercritical fluid	SC-CO_2	*C. necator*	Yield: 89%	Hejazi *et al.* [49]
Cell fragility	Chloroform	*B. flexus*	Yield: 43%	Divyashree and Shamala [56]
	Sodium hypochlorite	*B. flexus*	Yield: 50%	Divyashree and Shamala [56]
	Alkaline hydrolysis	*B. flexus*	Yield: 50%	Divyashree and Shamala [56]
Self flotation of cell debris	Chloroform	*Zobellella denitrificans* MW1	Purity: 98%; Yield: 85%	Ibrahim and Steinbüchel [57]
Dissolved air flotation	Enzymatic hydrolysis, sonification, flotation	*P. putida*	Purity: 86%	van Hee *et al.* [58]
Aqueous two phase system	*Microbispora* sp culture-ATPS	*B. flexus*	Purity: 95%; Yield: 50%	Divyashree *et al.* [37]
Gamma irradiation	Radiation-chloroform	*B. flexus*	Yield: 45–54%	Divyashree and Shamala [61]
Air classification		*E. coli*	Purity: 97%; Yield: 90%	Noda [72]
		C. necator	Purity: 95%; Yield: 85%	Noda [72]
Spontaneous liberation		*E. coli*	Autolysis of 80%	Jung *et al.* [73]

Table 2. Comparison of the advantages and disadvantages of various PHA extraction methods

Recovery method	Advantages	Disadvantages
Solvent extraction	Removal of endotoxin Useful for medical applications High purity Negligible/limited degradation to the polymer Higher molecular weight	Not environmentally friendly Consumption of large volume of toxic and volatile solvents High capital and operation cost Difficulty in extracting PHA from solution containing more than 5% (w/v) P(3HB) Lengthy process Native order of polymer chains in PHA granules might be disrupted
Chemical Digestion Surfactant	Extracted PHA retains original molecular weight Native order of polymer chains in PHA granules is retained	Low purity of PHA Treatment required to remove surfactant from wastewater
Sodium hypochlorite	Higher purity of PHA can be obtained	Severe reduction in molecular weight of the extracted PHA
Sequential surfactant-hypochlorite	High quality of PHA Rapid recovery and simple process Retain native order of polymer chains in PHA granules Lower operating cost compared to solvent extraction	Combined cost of surfactant and sodium hypochlorite Wastewater treatment required to remove residual surfactant and sodium hypochlorite
Dispersion sodium hypochlorite and solvent extraction	High purity of PHA Reduced viscosity of solvent phase due to digestion of non-polymer cellular material (NPCM) by sodium hypochlorite	Not environmentally friendly Consumption of large volume of toxic and volatile solvents Higher recovery cost
Surfactant-chelate	Convenient operation High quality of product	Produce large volume of wastewater
Selective dissolution of NPCM by protons	Low operating cost Higher recovery yield	Severe reduction in molecular weight if the process parameters are not controlled stringently
Enzymatic digestion	Mild operation conditions Good recovery with good quality	Complex process High cost of enzymes
Bead mill	No chemicals used Less contamination Not susceptible to blockages No micronization of PHA granules	Require several passes Long processing time Various process parameters have to be controlled precisely
High pressure homogenization	No chemicals used Less contamination	Severe micronization of PHA granules Depends on both process and microbial physiological parameters Possible for thermal degradation of desired products Formation of fine cellular debris that interfere with downstream processing
Supercritical fluid (SCF)	Simple Inexpensive Rapid Environmentally friendly	Dependent on process parameters Frequent need for clean up Difficulties in extracting polar analytes Difficulties in dealing with natural samples
Cell fragility	Simple recovery method Mild extraction conditions	Need to balance cell wall softening and cell wall integrity
Self-flotation	Cost effective as additional steps could be avoided	Consumption of large volume of toxic and volatile solvents
Dissolved-air flotation	No chemicals used Less contamination	Requires several consecutive flotation steps
Aqueous two phase system (ATPS)	Short processing time Low material cost Low energy consumption Good resolution High yield and a relatively high capacity	Dependent on process parameters Issue of robustness and reproducibility Absence of commercial kits to evaluate ATPS at bench scale Poor understanding of the mechanism
Gamma irradiation	Retention of solvent solubility due to the low degree of cross-linking No chemicals used/Less contamination	Length of irradiation time High initial investment cost

extraction may disrupt the unique nascent state of the P(3HB) granules that maybe useful in certain applications. In case of accidents, the potential release of a large amount of highly toxic and volatile solvents to the environment is also of great concern [17, 21–23]. Therefore, 1,2-propylene carbonate has been proposed as an alternative to halogenated solvents in the recovery process of PHA [24–25]. Higher boiling point (240°C) of 1,2-propylene carbonate prevents the evaporation to the environment

at lower temperatures and allows its reusability for several cycles of purification. This could reduce the solvent consumption and therefore it is viewed as economically advantageous. Besides, 1,2-propylene carbonate is considered safe due to its low toxicity. It is widely used in many applications including cosmetics [24]. Fiorese *et al.* [25] reported a maximum PHA yield of 95% and a purity of 84% when extracted from the *C. necator* cells at 130°C for 30 min without involving any pretreatment. This is comparable to the values obtained from chloroform extraction (94% yield and 98% purity). For the extraction of mcl-PHA, methyl *tert*-butyl ether (MTBE) has been evaluated and the extractability was found to be promising as in the case with chlorinated-solvents [26]. Wampfler *et al*. [26] claimed that MTBE would have lower environmental impact if the recovery of PHA as well as the production and recycling of MTBE could be carried out in closed facilities.

3.2. Digestion methods

While solvent extraction techniques involve the solubilization of the PHA granules, digestion methods involve the solubilization of the cellular materials surrounding the PHA granules. Digestion methods are well established approaches developed as an alternative to solvent extraction and can be classified into either chemical digestion or enzymatic digestion. Because of the ready availability of various chemicals with known properties many studies have been directed towards the development of chemical digestion methods compared to enzymatic digestion.

3.2.1. Chemical digestion

Various chemical digestion methods have been evaluated for the recovery PHA from cellular biomass (Table 1). The approach is based on the solubilization of non-PHA cellular mass (NPCM) and mainly utilizes sodium hypochlorite or surfactants. The important features of sodium hypochlorite such as strong oxidizing properties and non-selectivity can be manipulated to digest NPCM and facilitate PHA recovery [21]. A range of surfactants has been evaluated such as sodium dodecyl sulfate (SDS), Triton X-100, palmitoyl carnitine, betaine and among them, SDS showed good performance. However, the quality of PHA obtained using either surfactant or sodium hypochlorite alone was not good enough (Table 2). Therefore, a combination of surfactant-sodium hypochlorite was used [22]. Isolation of PHA granules by surfactant digestion exhibited lower degree of purity but had slightly higher molecular weight than sodium hypochlorite digestion (Table 2). In contrast, PHA of higher purity was obtained using sodium hypochlorite but with severe degradation of molecular weight up to 50% [27]. Sequential surfactant-hypochlorite treatment promoted better and rapid recovery of PHA [27–28] and resulted in 50% reduction of overall cost when compared to solvent extraction [22]. Yet, the low operating cost [17] and technical simplicity of this process are not complemented by the complex and unresolved problems caused by surfactant in wastewater treatment and relatively high cost of chemical agents such as SDS and sodium hypochlorite (Table 2) [22]. Hahn and co-researchers established a separation process that took advantage of both differential digestion and solvent extraction [29–30]. The hydrophobicity of P(3HB) and hydrophilicity of lyophilized cells accounted for the development of dispersions of a sodium hypochlorite solution and chloroform. A study by Valappil *et al.* [31] described that the high molecular weight of P(3HB) could be retained by using this method. The main limitation is the use of large quantity of solvent that would raise the recovery cost (Table 2). Surfactant-chelate digestion system was also explored to improve cell disruption and to increase the rate of PHA release [32]. Use of recycled wastewater was proposed later as this system produced large volume of wastewater [33]. Surfactant-chelate digestion (Triton X-100 and ethylenediaminetetraacetic acid [EDTA]) could isolate PHA with 90% purity from enzymatically hydrolyzed cells of *S. meliloti* [34]. Another method is the selective dissolution of non-PHA cell mass by protons to enhance PHA recovery [21–22]. This method is comprised of few steps, but the most important is the solubilization of NPCM in an acidic solution to release partially crystallized PHA granules and later subjecting the suspension to decolorization in a bleaching solution. This method was claimed to lower the recovery cost by using cheaper chemicals with higher recovery efficiency. However, the process parameters have to be controlled stringently if the molecular weight is to be maintained at a minimum of 50% the original molecular

weight. The P(3HB) granules recovered by this method was reported to be highly crystalline.

3.2.2. Enzymatic digestion

Recovery process of PHA using enzymatic digestion involves a rather complex procedure (Table 1). Solubilization of cell components other than PHA typically consists of heat treatment, enzymatic hydrolysis and surfactant washing [35]. To date, various types of enzymes, especially proteases, have been evaluated for their efficiency in causing cell lysis [36]. Lakshman and Shamala [34] used *Microbispora* sp. culture, which was identified to secrete protease, in the fermented broth of *S. meliloti* containing 50% of PHA to induce hydrolysis. The culture was introduced to the thermally (80°C for 10 min) inactivated biomass of *S. meliloti* and incubated for 72 h. The *S. meliloti* cells were hydrolyzed by the protease resulting in the release of the intracellular components together with the PHA granules. The culture containing the lysed cells was then subjected to a simple filtration process and PHA of 94% purity was recovered using chloroform extraction. In contrast, PHA with only 66% purity was isolated from the undigested cells by using chloroform extraction. Similar study was conducted recently with a different strain by Divyashree *et al*. [37]. *Microbispora* sp. culture mixed with *Bacillus flexus* and subjected to separation by aqueous two phase system (ATPS) resulted in PHA with 92% purity. The enzyme technique is attractive because of its mild operation conditions (Table 2) [38–39]. Because enzymes are very specific with respect to the reactions they catalyze, recovery of PHA with good quality could be expected. Nevertheless, the high cost of enzymes and complexity of the recovery process outweigh its advantages [39].

3.3. Mechanical disruption

Mechanical cell disruption is widely used to liberate intracellular protein [40]. The concept has been tested to recover PHA from bacterial cells [23]. Among the various mechanical disruption methods, bead milling and high-pressure homogenization dominate the large scale cell disruption in pharmaceutical and biotechnology industries [41]. Unlike other recovery methods, mechanical disruption is favored mainly due to economic advantageous and because it causes mild damage to the products [23]. Mechanical disruption of cells does not involve any chemicals so it minimizes environmental pollution [17] and contamination to the products [23]. In general, the drawbacks of mechanical disruption method are, high capital investment cost, long processing time and difficulty in scaling up [42–43].

3.3.1. Bead mill

The principle of bead mills is based on the shearing action and energy transfer from beads to cells in the contact zones (Table 1). The key parameters that affect the disruption process are the bead loading and bead diameter [38]. Tamer *et al*. [23] reported that with bead diameter of 512 μm and 2800 rpm agitation speed, complete disruption of the *Alcaligenes latus* cells was achieved after eight passes when the loading was 85% compared to loading of 75% that required more than 16 passes to release most of the cellular protein. The extent of cell disruption also depends on numerous parameters such as residence time distribution (RTD), shear forces, type of microorganisms, cell concentration, feed rate of the suspension, agitator speed, geometry of the grinding chamber and design of the stirrer [44]. Bead mills disruption was recommended for PHA recovery as it requires less power supply, not susceptible to blockages and different diameter of beads did not significantly affect the disruption rate although micronization of P(3HB) is possible with smaller bead size [23]. The major concern is that large number of factors has to be considered to establish a good bead mill disruption system (Table 2) [44].

3.3.2. High pressure homogenization

With high pressure homogenization, disruption of cell suspension occurs under high pressure through an adjustable, restricted orifice discharge valve (Table 1) [45]. Process parameters such as operating pressure, number of passes, suspension temperature and homogenizer valve design must be carefully scrutinized for efficient disruption [46–47]. It was reported that less efficient recovery of P(3HB) from *A. latus* was obtained with homogenizer compared to bead mill disruption due to severe micronization [23]. Nevertheless, P(3HB) with 95% purity and 98% yield was recovered from 5% (w/v) SDS pretreated *Methylobacterium* sp V49 cells subjected to homogenization at an operating pressure 400 $kg \cdot cm^{-2}$ after two cycles [48]. Process parame-

ters are not the only factors that influence the cell disruption but microbial physiological parameters, namely type and growth phase of the microorganisms as well as cell concentration also affect the disruption efficiency (Table 2). Generally, Gram-positive bacteria are more difficult to be disrupted compared to Gram-negative bacteria [47]. Among the drawbacks associated with high pressure homogenization include the possibility of thermal degradation of desired products [48] and formation of fine cellular debris that would interfere with the further downstream processing of PHA granules [46].

3.4. Supercritical fluid (SCF)

Supercritical fluids (SCF) have emerged as a potential extraction technique in the areas of PHA recovery (Table 1) [49–51]. The unique physicochemical properties of SCF such as high density and low viscosities proposed them as suitable extraction solvents [49]. The advantages offered by SCF have led to its popularity (Table 3). Supercritical-carbon dioxide (SC–CO_2) is the most predominantly used SCF due to its low toxicity and reactivity, moderate critical temperature and pressure (31°C and 73 atm), availability, low cost, and non-flammability [49]. By using this method, P(3HB) recovery of 89% from *C. necator* at 200 atm, 40°C and 0.2 ml of methanol was reported [49]. Besides, there is a patent literature which describes on the purification of biopolymers such as rubber from plant material using SCF [52]. Although, the recovery obtained are comparable to other methods, it has to be highlighted that SC–CO_2 efficiency in bacterial cell disruption is very much dependent on the process parameters such as operating pressure, temperature, type of modifier as well as culture cultivation time (Table 2) [53]. High temperature and pressure significantly influence the physiological properties of cell membrane that prevent the biopolymer from being extracted. The addition of modifier plays an important role in increasing the polarity of the CO_2 therefore suitable modifier should be selected to enhance the cell wall permeability. Matured cells are difficult to be disrupted compared to those in early-exponential phase as new proteins would be synthesized increasing the cell resistance to disruption. In order to make the process more economically viable, Khosravi-Darani *et al*. [53] investigated on a series of pretreatment to improve the SC–CO_2 disruption. They found that with 1% (v/v) toluene as a modifier, 200 bar of pressure, 30°C temperature and two times SC–CO_2 pressure release, up to 81% P(3HB) recovery could be achieved by using wet cells of *C. necator*. To further improve the purity of the P(3HB), chemical pretreatment with 0.4% (w/w) sodium hydroxide (NaOH) was employed. The proposed recovery process of PHA is more economical as the costly freeze drying step could be avoided.

Table 3. Summary of supercritical fluids (SCF) cell disruption

Extraction method	Advantages	Disadvantages	References
Supercritical fluid (SCF)	Simple, inexpensive Rapid Environmentally friendly Fluid solvation power Minimizes equipment and labor needs, contamination and loss of yield Solution for drastic problems related to • non-thermal cell inactivation • enzyme inactivation • permeabilization • extraction of fermentation products	Frequent need for clean up Difficulties in • extracting polar analytes • measurement and prediction of biomolecules solubility at varying pressure and temperature for process optimization • dealing with natural samples	Luque de Castro and Jiménez-Carmona [74] Khosravi-Darani *et al.* [53] Cornish *et al.* [52] Khosravi-Darani and Mozafari [50]
Types of SCF			
Carbon dioxide	Low toxicity and reactivity Moderate critical temperature and pressure Good availability Low cost Non-flammable	Low dielectric constant	Hejazi *et al.* [49] Luque de Castro and Jiménez-Carmona [74]
Ammonia	Better solvent strength than carbon dioxide	Difficult to pump Chemically reactive Dangerous for routine use	Luque de Castro and Jiménez-Carmona [74]
Methanol	Excellent solvent	High critical temperature Liquid at ambient temperature, therefore complicates extraction process	Luque de Castro and Jiménez-Carmona [74]

3.5. Cell fragility

Increase in osmotic fragility during the accumulation of PHA are well documented with some microorganisms such as *Azotobacter vinelandii* UWD and recombinant *E. coli* (Table 1) [54–55]. The cell wall strength of these microorganisms could be compromised by modifying the composition of the growth medium. Cell fragility mechanism is not only restricted to Gram negative microorganisms but could be also exploited for Gram positive microorganisms [56]. Page and Cornish [55] demonstrated that the addition of fish peptone to the cultivation medium of *A. vinelandii* UWD led to the formation of large, pleomorphic, osmotically sensitive cells while high molecular weight P(3HB) synthesis was enhanced. About 92% of P(3HB) could be quickly extracted from the fragile cells with 1 N aqueous NH_3 (pH 11.4) at 45°C for 10 min. The same phenomenon was observed with *B. flexus* [56]. The cells grown in the inorganic salts medium suffered from the absence of diaminopimelic acid (DAP) and decreased concentrations of other amino acids. DAP is an important component that formed cross bridge in the peptidoglycan and have a great influence on the structural stability of the cell wall. Up to 86–100% PHA recovery was obtained using hot chloroform or mild alkaline hydrolysis with cells cultivated in inorganic medium while only 32–56% of PHA was able to be extracted from cells grown in organic medium supplemented with peptone or yeast. Simple recovery method with mild extraction conditions could be developed based on cell fragility. However, it is necessary to balance the cell wall softening and cell wall integrity [55] in order to promote microbial growth with higher PHA content (Table 2).

3.6. Flotation

Ibrahim and Steinbüchel [57] investigated the recovery of P(3HB) from a recently isolated bacterium, *Zobellella denitrificans* MW1 (Table 1). Simple extraction with various organic solvents followed by self-flotation of cell debris was tested. The cells were mixed with chloroform at 30°C for 72 h and later subjected to self-flotation of cell debris overnight at room temperature. This method allowed efficient recovery of 85% (w/w) of P(3HB) with purity of 98%. This method should be cost effective as additional steps such as centrifugation and wastage of polymer during recovery could be avoided (Table 2) [57]. Adoption of green solvents together with flotation technique perhaps would add more benefits for the downstream processing of PHA. Previously, selective dissolved-air flotation was also applied to extract mcl-PHA from the cell debris of *P. putida* (Table 1) [58]. The main limitation of dissolved-air flotation is that it requires several consecutive flotation steps (Table 2).

3.7. Aqueous two phase system (ATPS)

Another potential method for the recovery of PHA was recently reported using *B. flexus* [37]. Aqueous two phase system (ATPS) is formed when two polymers at low concentrations (or of one polymer and an inorganic salt) that display incompatibility are mixed such that two immiscible phases coexist (Table 1) [59]. PHA containing *B. flexus* cells were subjected to enzymatic hydrolysis of *Microbispora* sp. cells filtrate and later introduced to polymer-salt ATPS system (Polyethylene glycol [PEG] 8000/phosphate, pH 8.0 and 28°C) reported recovery of high molecular weight PHA ($1 \cdot 10^6$) with 97% purity. In addition, the authors highlighted that protease present in the *Microbispora* sp. cells filtrate was also isolated with several fold purity as a byproduct together with PHA [37]. Several factors, i.e. polymer molecular weight, concentration of polymer and salt, pH, molecular mass, charge etc. have to be considered to choose a good ATPS recovery system. This technique is considered attractive because of short processing time, low material cost, low energy consumption, good resolution, high yield and a relatively high capacity [59–60]. However, ATPS is not yet being used in industrial scale due to problems such as robustness, reproducibility, absence of commercial kits to evaluate ATPS at bench scale as well as poor understanding of the mechanism (Table 2) [60].

3.8. Gamma irradiation

The effect of gamma irradiation on the wet cells of *B. flexus* to assist cell disruption for PHA recovery has also been investigated (Table 1) [61]. PHA recovery of 54% (based on biomass dry weight) was attained with the irradiated cells (10 kGy) subjected to chloroform extraction at room temperature in a short period. However, only 18–20% of PHA (based on biomass dry weight) was recovered from

unirradiated cells exposed to chloroform extraction at 37°C and 150 rpm for 2 h. Gamma irradiation offers many advantages such as promoting optimal disruption of cells at low dosage of irradiation which enable easier recovery of PHA. Besides, retention of solvent solubility due to the low degree of cross-linking was reported [61]. Furthermore, radiation induced cell disruption is independent of any chemicals resulting in relatively contamination free process. The major setbacks of this technique are the length of irradiation time and the initial investment cost that hinders large scale applications (Table 2) [62].

The chemicals and the conditions used for each recovery technique described above are summarized in Table 4. This table clearly shows that chemicals such as organic solvents, alkaline or acidic solutions and surfactants are widely used in most of the PHA recovery methods and have been tested under different working conditions. Even with fragile cells, mild chemicals such as aqueous NH_3 are still required in order to completely rupture the cells. In contrast, enzymatic digestion seems to be more environmentally friendly. However, pure enzymes are costly. In order to address the cost issue, some researchers have used whole microbial cultures as the source of the enzymes. It has been reported that the use of *Microbispora* sp. culture instead of pure enzymes to hydrolyze *S. meliloti* cells and was found to be promising. Some methods like bead mill, high-pressure homogenization and supercritical fluid disruption are also environmentally friendly since no chemicals are involved in the PHA recovery process. The use of gamma irradiation has to be extensively studied to prove its efficiency.

4. Large scale production of PHA

The underlying challenge for the commercialization of PHA is the high production cost which arises predominantly due to expensive purification technologies of PHA. Still, many attempts have been made on the development of simple fermentation strategies as well as modification of recovery techniques in order to scale-up the PHA production.

Table 4. Various chemicals and conditions used in PHA recovery techniques

Recovery method	Strain	Chemical(s) and conditions	Reference
Solvent extraction	*Cupriavidus necator* DSM 545	1,2-propylene carbonate, 130°C for 30 min	Fiorese *et al.* [25]
Digestion with surfactant	Recombinant *Escherichia coli*	Sodium dodecyl sulfate (SDS), 30°C, 1 h	Choi and Lee [54]
Digestion with sodium hypochlorite	*C. necator* Recombinant *E. coli*	Sodium hypochlorite, 30°C, 1 h	Hahn *et al*. [69]
Digestion with surfactant-sodium hypochlorite	*Azotobacter chroococcum* G-3	SDS, 55°C, 15 min followed by sodium hypochlorite, 30°C, 3 min	Dong and Sun [28]
Digestion with surfactant-chelate	*Sinorhizobium meliloti*	Triton X-100 mixed with EDTA, 50°C, 10 min	Lakshman and Shamala [34]
Dispersion of sodium hypochlorite and chloroform	Bacillus cereus SPV	50 ml chloroform : 50 ml sodium hypochlorite, 38°C, 1 h	Valappil *et al.* [31]
Selective dissolution by protons	Cell slurry	0.1 M H_2SO_4, 100°C, 120 min followed by pH adjustment (pH 10) and decolorization using bleaching solution, 2 h, room temperature	Yu [22]
Enzymatic digestion	*S. meliloti*	*Microbispora* sp. culture-chloroform	Lakshman and Shamala [34]
Bead mill	*Alcaligenes latus*	Bead diameter of 512 μm, bead loading of 85%, 2800 rpm	Tamer *et al.* [23]
High pressure homogenization	*Methylobacterium* sp V49	Operating pressure 400 $kg \cdot cm^{-2}$, 5% (w/v) SDS	Ghatnekar *et al.* [48]
Supercritical fluid	*C. necator*	Supercritical CO_2, 100 min, 200 atm, 40°C and 0.2 ml of methanol	Hejazi *et al.* [49]
Cell fragility	*Azotobacter vinelandii* UWD	1 N aqueous NH_3 (pH 11.4), 45°C 10 min	Page and Cornish [55]
Self flotation of cell debris	*Zobellella denitrificans* MW1	Chloroform, 30°C, 72 h, Self flotation of cell debris overnight at room temperature	Ibrahim and Steinbüchel [57]
Aqueous two phase system	*B. flexus*	Polyethylene glycol [PEG] 8000/phosphate, pH 8.0 and 28°C, 30 min	Divyashree *et al.* [37]
Gamma irradiation	*B. flexus*	Radiation doses of 10–40 kGy	Divyashree and Shamala [61]

Chen *et al.* [63] investigated the accumulation of poly(3-hydroxybutyrate-*co*-3-hydroxyhexanoate) [P(3HB-*co*-3HHx)] from *Aeromonas hydrophila* 4AK4, which was cultivated in a 20 000 l fermentor using lauric acid as the carbon source under phosphorus limitation. A maximum cell dry weight (CDW) of 50 g/l and PHA content of 50 wt% was achieved by optimizing the carbon source concentrations and the time point for applying phosphorus limitation. The cultivated cells were initially precipitated by adding 1% Na_2HPO_4, 1% $CaCl_2$, and 100 ppm polyacrylamide into the fermentor and filter-pressed to remove water. The cakes of cells were then freeze-dried and ground into powder. PHA extraction was carried out by gently stirring 200–500 kg of dried cells at 60°C for 2 h in 30 000 l extraction tank containing 5000 l of ethyl acetate. The polymer solution was passed through a metal filter and centrifuged to remove cell debris before performing precipitation using 15 000 l of hexane or heptane. Finally, the flocculants of polymer were collected using filter press followed by washing with ethanol before being vacuum-dried. The use of solvents such as ethyl acetate, hexane or heptane were thought to reduce the PHA recovery cost, which accounted to more than 50% of the overall PHA production cost since the solvents could be recovered by distillation. The idea of acetone-water based PHA extraction was proposed to make the recovery process more economically feasible. Recently, large-scale cultivation of *P. putida* GPo1 and recovery of poly(3-hydroxyoctanoate) (PHO) were studied [64]. As high as 53 g/l of CDW with 60 wt% PHA accumulation was obtained by manipulating the inoculum size (1–2%), pH of the medium as well as carbon (octanoic acid) and nitrogen (ammonium octanoate) source concentrations. Continuous separation together with continuous cell release from the separator was used to separate the cells before the freeze drying process. The recovery process involved 25 kg freeze-dried cells in 250 l of acetone which was later concentrated to 75 l. Acetone as an alternative to chlorinated solvents, is an inexpensive, relatively safe and readily available renewable resource, which can be produced as a by-product of microbial fermentation. The acetone recovered through distillation was used several times to lower the extraction costs. The recycling strategy applied in this research [64] was similar to the work described by Chen and co-workers [63]. Precipitation solvents composed of 70% (v/v) methanol and 70% (v/v) ethanol has also been evaluated. This mixture overcomes the problem of 10 volumes of PHA non-solvent consumption for precipitation of the polymer when acetone was used as a solvent. Instead, 1:1 (v/v) ratio of the mixture to PHO concentrate was sufficient to isolate 94% of PHO with 99% purity [64]. Comparison of the two PHA recovery methods reported using different types of solvents suggests the latter to have more profound economical impacts. The best option is to reduce the extensive use of solvents. If acetone-water based recovery method could be developed and extended for extraction of various types of PHA, it will be possible to reduce the extraction cost.

5. Summary and outlook

Microbial PHA is a potential renewable biopolymer with properties closely resembling some common petrochemical plastics. Because of the vast range of structurally different monomers that can be polymerized by microbes, a wide range of material properties can be achieved. Metabolic engineering and high-density cell culture technologies can be exploited for the large-scale production of specified PHA. Based on information reported in the literatures, it is not impossible to grow bacterial cells up to a density of 150 g/l with a PHA content of more than 80 wt% of the cell dry weight. However, the extraction and purification of the PHA granules from the cell biomass is a challenging task especially when one considers the use of environmentally hazardous chemicals as an unacceptable option in the production of eco-friendly materials. This paper has reviewed the various types of methods that have been tested for the extraction and purification of PHA granules from microbial cell biomass. While cost is a major deciding factor in the selection of a suitable method, it is generally expected that the usage of strong chemicals and solvents need to be minimized. The final intended application for the PHA will determine the degree of purity of the PHA granules. For example, in medical applications it is absolutely necessary that the PHA should be free from bacterial endotoxins and other contaminating chemicals and solvents. On the other hand, if the PHA is intended for applications such as mulching

film or garbage bags, a lower degree of purity may be acceptable. Regardless of its final applications, the molecular weights of the recovered PHA should be sufficiently high. This is because the thermal processing of the PHA would result in the reduction of its molecular weights to some extent. Therefore, it is important to have PHA resins with as high a molecular weight as possible. In order to obtain PHA with a high degree of purity, more stringent recovery process is needed. This often results in PHA with lower molecular weights. In addition, the recovery yield will also be lower. Therefore, the challenge in the recovery process is to maintain the original molecular weights while not compromising the degree of purity for various applications. These criteria have to be achieved in an environmentally friendly manner. Finally, and most importantly, the cost of the recovery process should be economically feasible. Together with PHA recovery techniques, fermentation strategies also should be governed. Development of strains that could effectively overproduce PHA from various unprocessed, cheap and renewable carbon sources also plays an important role in lowering the cost of PHA production. Commercialization of PHA could be accomplished by broadening the PHA application areas and exploring more high value added usage such as medical applications.

Acknowledgements

B. Kunasundari gratefully acknowledges USM Fellowship for financial support. We also thank Yoga Sugama Salim and Rathi Devi Nair for their help in editing this manuscript.

References

[1] Lazarevic D., Aoustin E., Buclet N., Brandt N.: Plastic waste management in the context of a European recycling society: Comparing results and uncertainties in a life cycle perspective. Resources, Conservation and Recycling, **55**, 246–259 (2010).
DOI: 10.1016/j.resconrec.2010.09.014

[2] Chen G-Q.: A microbial polyhydroxyalkanoates (PHA) based bio- and materials industry. Chemical Society Reviews, **38**, 2434–2446 (2009).
DOI: 10.1039/b812677c

[3] Sudesh K., Abe H., Doi Y.: Synthesis, structure and properties of polyhydroxyalkanoates: Biological polyesters. Progress in Polymer Science, **25**, 1503–1555 (2000).
DOI: 10.1016/S0079-6700(00)00035-6

[4] Taguchi S., Yamada M., Matsumoto K., Tajima K., Satoh Y., Munekata M., Ohno K., Kohda K., Shimamura T., Kambe H., Obata S.: A microbial factory for lactate-based polyesters using a lactate-polymerizing enzyme. Proceedings of the National Academy of Sciences of the United States of America, **105**, 17323–17327 (2008).
DOI: 10.1073/pnas.0805653105

[5] Yamada M., Matsumoto K., Nakai T., Taguchi S.: Microbial production of lactate-enriched poly[(R)-lactate-co-(R)-3-hydroxybutyrate] with novel thermal properties. Biomacromolecules, **10**, 677–681 (2009).
DOI: 10.1021/bm8013846

[6] Shozui F., Matsumoto K., Nakai T., Yamada M., Taguchi S.: Biosynthesis of novel terpolymers poly (lactate-co-3-hydroxybutyrate-co-3-hydroxyvalerate)s in lactate-overproducing mutant *Escherichia coli* JW0885 by feeding propionate as a precursor of 3-hydroxyvalerate. Applied Microbiology and Biotechnology, **85**, 949–954 (2009).
DOI: 10.1007/s00253-009-2100-y

[7] Koller M., Hesse P., Kutschera C., Bona R., Nascimento J., Ortega S., Agnelli J. A., Braunegg G.: Sustainable embedding of the bioplastic poly-(3-hydroxybutyrate) into the sugarcane industry: Principles of a future-oriented technology in Brazil. in 'Polymers – Opportunities and risks II: Sustainability, product design and processing' (eds.: Eyerer P., Weller M., Hübner C.) Springer-Verlag Berlin Heidelberg, New York, Vol 12, 81–96 (2009).
DOI: 10.1007/698_2009_11

[8] Loo C-Y., Lee W-H., Tsuge T., Doi Y., Sudesh K.: Biosynthesis and characterization of poly(3-hydroxybutyrate-co-3- hydroxyhexanoate) from palm oil products in a *Wautersia eutropha* mutant. Biotechnology Letters, **27**, 1405–1410 (2005).
DOI: 10.1007/s10529-005-0690-8

[9] Lee W-H., Loo C-Y., Nomura C. T., Sudesh K.: Biosynthesis of polyhydroxyalkanoate copolymers from mixtures of plant oils and 3-hydroxyvalerate precursors. Bioresource Technology, **99**, 6844–6851 (2008).
DOI: 10.1016/j.biortech.2008.01.051

[10] Ng K-S., Ooi W-Y., Goh L-K., Shenbagarathai R., Sudesh K.: Evaluation of jatropha oil to produce poly (3-hydroxybutyrate) by *Cupriavidus necator* H16. Polymer Degradation and Stability, **95**, 1365–1369 (2010).
DOI: 10.1016/j.polymdegradstab.2010.01.021

[11] Kahar P., Tsuge T., Taguchi K., Doi Y.: High yield production of polyhydroxyalkanoates from soybean oil by *Ralstonia eutropha* and its recombinant strain. Polymer Degradation and Stability, **83**, 79–86 (2004).
DOI: 10.1016/S0141-3910(03)00227-1

[12] Sudesh K., Bhubalan K., Chuah J-A., Kek Y-K., Kamilah H., Sridewi N., Lee Y-F.: Synthesis of polyhydroxyalkanoate from palm oil and some new applications. Applied Microbiology and Biotechnology, **89**, 1373–1386 (2010).

[13] Akiyama M., Tsuge T., Doi Y.: Environmental life cycle comparison of polyhydroxyalkanoates produced from renewable carbon resources by bacterial fermentation. Polymer Degradation and Stability, **80**, 183–194 (2003).
DOI: 10.1016/S0141-3910(02)00400-7

[14] Sudesh K., Gan Z., Maehara A., Doi Y.: Surface structure, morphology and stability of polyhydroxyalkanoate inclusions characterised by atomic force microscopy. Polymer Degradation and Stability, **77**, 77–85 (2002).
DOI: 10.1016/S0141-3910(02)00081-2

[15] Sudesh K., Maehara A., Gan Z., Iwata T., Doi Y.: Direct observation of polyhydroxyalkanoate granule-associated-proteins on native granules and on poly(3-hydroxybutyrate) single crystals by atomic force microscopy. Polymer Degradation and Stability, **83**, 281–287 (2004).
DOI: 10.1016/S0141-3910(03)00273-8

[16] Khanna S., Srivastava A. K.: Recent advances in microbial polyhydroxyalkanoates. Process Biochemistry, **40**, 607–619 (2005).
DOI: 10.1016/j.procbio.2004.01.053

[17] Jacquel N., Lo C-W., Wei Y-H., Wu H-S., Wang S. S.: Isolation and purification of bacterial poly(3-hydroxyalkanoates). Biochemical Engineering Journal, **39**, 15–27 (2008).
DOI: 10.1016/j.bej.2007.11.029

[18] Ramsay J. A., Berger E., Voyer R., Chavarie C., Ramsay B. A.: Extraction of poly-3-hydroxybutyrate using chlorinated solvents. Biotechnology Techniques, **8**, 589–594 (1994).
DOI: 10.1007/BF00152152

[19] Lafferty R. M., Heinzle E.: Use of cyclic carbonic acid esters as solvents for poly-(β-hydroxybutyric acid). U.S. Patent 4140741, USA (1979).

[20] Jiang X., Ramsay J. A., Ramsay B. A.: Acetone extraction of mcl-PHA from *Pseudomonas putida* KT2440. Journal of Microbiological Methods, **67**, 212–219 (2006).
DOI: 10.1016/j.mimet.2006.03.015

[21] Yu J., Chen L. X. L.: Cost-effective recovery and purification of polyhydroxyalkanoates by selective dissolution of cell mass. Biotechnology Progress, **22**, 547–553 (2006).
DOI: 10.1021/bp050362g

[22] Yu J.: Recovery and purification of polyhydroxyalkanoates. U.S. Patent 7514525, USA (2009).

[23] Tamer I. M., Moo-Young M., Chisti Y.: Disruption of *Alcaligenes latus* for recovery of poly(β-hydroxybutyric acid): Comparison of high-pressure homogenization, bead milling, and chemically induced lysis. Industrial and Engineering Chemistry Research, **37**, 1807–1814 (1998).
DOI: 10.1021/ie9707432

[24] McChalicher C. W. J., Srienc F., Rouse D. P.: Solubility and degradation of polyhydroxyalkanoate biopolymers in propylene carbonate. AIChE Journal, **56**, 1616–1625 (2010).
DOI: 10.1002/aic.12087

[25] Fiorese M. L., Freitas F., Pais J., Ramos A. M., de Aragão G. M. F., Reis M. A. M.: Recovery of polyhydroxybutyrate (PHB) from *Cupriavidus necator* biomass by solvent extraction with 1,2-propylene carbonate. Engineering in Life Sciences, **9**, 454–461 (2009).
DOI: 10.1002/elsc.200900034

[26] Wampfler B., Ramsauer T., Rezzonico S., Hischier R., Köhling R., Thöny-Meyer L., Zinn M.: Isolation and purification of medium chain length poly(3-hydroxyalkanoates) (mcl-PHA) for medical applications using nonchlorinated solvents. Biomacromolecules, **11**, 2716–2723 (2010).
DOI: 10.1021/bm1007663

[27] Ramsay J. A., Berger E., Ramsay B. A., Chavarie C.: Recovery of poly-3-hydroxyalkanoic acid granules by a surfactant-hypochlorite treatment. Biotechnology Techniques, **4**, 221–226 (1990).
DOI: 10.1007/BF00158833

[28] Dong Z., Sun X.: A new method of recovering polyhydroxyalkanoate from *Azotobacter chroococcum*. Chinese Science Bulletin, **45**, 252–256 (2000).
DOI: 10.1007/BF02884685

[29] Hahn S. K., Chang Y. K., Kim B. S., Chang H. N.: Optimization of microbial poly(3-hydroxybutyrate) recovery using dispersions of sodium hypochlorite solution and chloroform. Biotechnology and Bioengineering, **44**, 256–261 (1994).
DOI: 10.1002/bit.260440215

[30] Hahn S. K., Chang Y. K., Kim B. S., Lee K. M., Chang H. N.: The recovery of poly(3-hydroxybutyrate) by using dispersions of sodium hypochlorite solution and chloroform. Biotechnology Techniques, **7**, 209–212 (1993).
DOI: 10.1007/BF02566149

[31] Valappil S. P., Misra S. K., Boccaccini A. R., Keshavarz T., Bucke C., Roy I.: Large-scale production and efficient recovery of PHB with desirable material properties, from the newly characterised *Bacillus cereus* SPV. Journal of Biotechnology, **132**, 251–258 (2007).
DOI: 10.1016/j.jbiotec.2007.03.013

[32] Chen Y., Chen J., Yu C., Du G., Lun S.: Recovery of poly-3-hydroxybutyrate from *Alcaligenes eutrophus* by surfactant–chelate aqueous system. Process Biochemistry, **34**, 153–157 (1999).
DOI: 10.1016/S0032-9592(98)00082-X

[33] Chen Y., Yang H., Zhou Q., Chen J., Gu G.: Cleaner recovery of poly(3-hydroxybutyric acid) synthesized in *Alcaligenes eutrophus*. Process Biochemistry, **36**, 501–506 (2001).
DOI: 10.1016/S0032-9592(00)00225-9

[34] Lakshman K., Shamala T. R.: Extraction of polyhydroxyalkanoate from *Sinorhizobium meliloti* cells using *Microbispora* sp. culture and its enzymes. Enzyme and Microbial Technology, **39**, 1471–1475 (2006). DOI: 10.1016/j.enzmictec.2006.03.037

[35] Holmes P. A., Lim G. B.: Separation process. U.S. Patent 4910145, USA (1990).

[36] Yasotha K., Aroua M. K., Ramachandran K. B., Tan I. K. P.: Recovery of medium-chain-length polyhydroxyalkanoates (PHAs) through enzymatic digestion treatments and ultrafiltration. Biochemical Engineering Journal, **30**, 260–268 (2006). DOI: 10.1016/j.bej.2006.05.008

[37] Divyashree M. S., Shamala T. R., Rastogi N. K.: Isolation of polyhydroxyalkanoate from hydrolyzed cells of *Bacillus flexus* using aqueous two-phase system containing polyethylene glycol and phosphate. Biotechnology and Bioprocess Engineering, **14**, 482–489 (2009). DOI: 10.1007/s12257-008-0119-z

[38] Middelberg A. P. J.: Process-scale disruption of microorganisms. Biotechnology Advances, **13**, 491–551 (1995). DOI: 10.1016/0734-9750(95)02007-P

[39] Kapritchkoff F. M., Viotti A. P., Alli R. C. P., Zuccolo M., Pradella J. G. C., Maiorano A. E., Miranda E. A., Bonomi A.: Enzymatic recovery and purification of polyhydroxybutyrate produced by *Ralstonia eutropha*. Journal of Biotechnology, **122**, 453–462 (2006). DOI: 10.1016/j.jbiotec.2005.09.009

[40] Harrison S. T. L.: Bacterial cell disruption: A key unit operation in the recovery of intracellular products. Biotechnology Advances, **9**, 217–240 (1991). DOI: 10.1016/0734-9750(91)90005-G

[41] Bury D., Jelen P., Kaláb M.: Disruption of *Lactobacillus delbrueckii* ssp. *bulgaricus* 11842 cells for lactose hydrolysis in dairy products: A comparison of sonication, high-pressure homogenization and bead milling. Innovative Food Science and Emerging Technologies, **2**, 23–29 (2001). DOI: 10.1016/S1466-8564(00)00039-4

[42] Park P. K., Kim E. Y., Chu K. H.: Chemical disruption of yeast cells for the isolation of carotenoid pigments. Separation and Purification Technology, **53**, 148–152 (2007). DOI: 10.1016/j.seppur.2006.06.026

[43] Balasundaram B., Harrison S. T. L.: Influence of the extent of disruption of Bakers' yeast on protein adsorption in expanded beds. Journal of Biotechnology, **133**, 360–369 (2008). DOI: 10.1016/j.jbiotec.2007.07.724

[44] Doucha J., Lívanský K.: Influence of processing parameters on disintegration of *Chlorella* cells in various types of homogenizers. Applied Microbiology and Biotechnology, **81**, 431–440 (2008). DOI: 10.1007/s00253-008-1660-6

[45] Geciova J., Bury D., Jelen P.: Methods for disruption of microbial cells for potential use in the dairy industry – A review. International Dairy Journal, **12**, 541–553 (2002). DOI: 10.1016/S0958-6946(02)00038-9

[46] Kelly W. J., Muske K. R.: Optimal operation of high-pressure homogenization for intracellular product recovery. Bioprocess and Biosystems Engineering, **27**, 25–37 (2004). DOI: 10.1007/s00449-004-0378-9

[47] Diels A. M. J., Michiels C. W.: High-pressure homogenization as a non-thermal technique for the inactivation of microorganisms. Critical Reviews in Microbiology, **32**, 201–216 (2006). DOI: 10.1080/10408410601023516

[48] Ghatnekar M. S., Pai J. S., Ganesh M.: Production and recovery of poly-3-hydroxybutyrate from *Methylobacterium* sp V49. Journal of Chemical Technology and Biotechnology, **77**, 444–448 (2002). DOI: 10.1002/jctb.570.abs

[49] Hejazi P., Vasheghani-Farahani E., Yamini Y.: Supercritical fluid disruption of *Ralstonia eutropha* for poly (β-hydroxybutyrate) recovery. Biotechnology Progress, **19**, 1519–1523 (2003). DOI: 10.1021/bp034010q

[50] Khosravi-Darani K., Mozafari M. R.: Supercritical fluids technology in bioprocess industries: A review. Journal of Biochemical Technology, **2**, 144–152 (2009).

[51] Khosravi-Darani K., Vasheghani-Farahani E., Yamini Y., Bahramifar N.: Solubility of poly(β-hydroxybutyrate) in supercritical carbon dioxide. Journal of Chemical and Engineering Data, **48**, 860–863 (2003). DOI: 10.1021/je020168v

[52] Cornish K., Martin J. A., Marentis R. T., Plamthottam S.: Extraction and fractionation of biopolymers and resins from plant materials. U.S. Patent 7259231, USA (2007).

[53] Khosravi-Darani K., Vasheghani-Farahani E., Shojaosadati S. A., Yamini Y.: Effect of process variables on supercritical fluid disruption of *Ralstonia eutropha* cells for poly(R-hydroxybutyrate) recovery. Biotechnologyl Progress, **20**, 1757–1765 (2004). DOI: 10.1021/bp0498037

[54] Choi J-I., Lee S. Y.: Efficient and economical recovery of poly(3-hydroxybutyrate) from recombinant *Escherichia coli* by simple digestion with chemicals. Biotechnology and Bioengineering, **62**, 546–553 (1999). DOI: 10.1002/(SICI)1097-0290(19990305)62:5<546::AID-BIT6>3.0.CO;2-0

[55] Page W. J., Cornish A.: Growth of *Azotobacter vinelandii* UWD in fish peptone medium and simplified extraction of poly-β-hydroxybutyrate. Applied and Environmental Microbiology, **59**, 4236–4244 (1993).

[56] Divyashree M. S., Shamala T. R.: Extractability of polyhydroxyalkanoate synthesized by *Bacillus flexus* cultivated in organic and inorganic nutrient media. Indian Journal of Microbiology, **50**, 63-69 (2010). DOI: 10.1007/s12088-010-0013-1

[57] Ibrahim M. H. A., Steinbüchel A.: Poly(3-hydroxybutyrate) production from glycerol by *Zobellella denitrificans* MW1 via high-cell-density fed-batch fermentation and simplified solvent extraction. Applied and Environmental Microbiology, **75**, 6222–6231 (2009). DOI: 10.1128/AEM.01162-09

[58] van Hee P., Elumbaring A. C. M. R., van der Lans R. G. J. M., Van der Wielen L. A. M.: Selective recovery of polyhydroxyalkanoate inclusion bodies from fermentation broth by dissolved-air flotation. Journal of Colloid and Interface Science, **297**, 595–606 (2006). DOI: 10.1016/j.jcis.2005.11.019

[59] Yang S., Huang Z., Jiang Z., Li L.: Partition and purification of a thermostable xylanase produced by *Paecilomyces thermophila* in solid-state fermentation using aqueous two-phase systems. Process Biochemistry, **43**, 56–61 (2008). DOI: 10.1016/j.procbio.2007.10.013

[60] Rito-Palomares M.: Practical application of aqueous two-phase partition to process development for the recovery of biological products. Journal of Chromatography B, **807**, 3–11 (2004). DOI: 10.1016/j.jchromb.2004.01.008

[61] Divyashree M. S., Shamala T. R.: Effect of gamma irradiation on cell lysis and polyhydroxyalkanoate produced by *Bacillus flexus*. Radiation Physics and Chemistry, **78**, 147–152 (2009). DOI: 10.1016/j.radphyschem.2008.08.010

[62] Bhattacharya A.: Radiation and industrial polymers. Progress in Polymer Science, **25**, 371–401 (2000). DOI: 10.1016/S0079-6700(00)00009-5

[63] Chen G. Q., Zhang G., Park S. J., Lee S. Y.: Industrial scale production of poly(3-hydroxybutyrate-co-3-hydroxyhexanoate). Applied Microbiology and Biotechnology, **57**, 50–55 (2001). DOI: 10.1007/s002530100755

[64] Elbahloul Y., Steinbüchel A.: Large-scale production of poly(3-hydroxyoctanoic acid) by *Pseudomonas putida* GPo1 and a simplified downstream process. Applied and Environmental Microbiology, **75**, 643–651 (2009). DOI: 10.1128/AEM.01869-08

[65] Narasimhan K., Cearley A. C., Gibson M. S., Welling S. J.: Process for the solvent-based extraction of polyhydroxyalkanoates from biomass. U.S. Patent 7378266, USA (2008).

[66] Zinn M., Weilenmann H-U., Hany R., Schmid M., Egli T.: Tailored synthesis of poly([R]-3-hydroxybutyrate-co-3-hydroxyvalerate) (PHB/HV) in *Ralstonia eutropha* DSM 428. Acta Biotechnologica, **23**, 309–316 (2003). DOI: 10.1002/abio.200390039

[67] Mantelatto P. E., Durao N. A. S.: Process for extracting and recovering polyhydroxyalkanoates (PHAs) from cellular biomass. U.S. Patent 20080193987, USA (2008).

[68] Lee K. M., Chang H. N., Chang Y. K., Kim B. S., Hahn S. K.: The lysis of gram-negative *Alcaligenes eutrophus* and *Alcaligenes latus* by palmitoyl carnitine. Biotechnology Techniques, **7**, 295–300 (1993). DOI: 10.1007/BF00150902

[69] Hahn S. K., Chang Y. K., Lee S. Y.: Recovery and characterization of poly(3-hydroxybutyric acid) synthesized in *Alcaligenes eutrophus* and recombinant *Escherichia coli*. Applied and Environmental Microbiology, **61**, 34–39 (1995).

[70] Berger E., Ramsay B. A., Ramsay J. A., Chavarie C., Braunegg G.: PHB recovery by hypochlorite digestion of non-PHB biomass. Biotechnology Techniques, **3**, 227– 232 (1989). DOI: 10.1007/BF01876053

[71] Kathiraser Y., Aroua M. K., Ramachandran K. B., Tan I. K. P.: Chemical characterization of medium-chain-length polyhydroxyalkanoates (PHAs) recovered by enzymatic treatment and ultrafiltration. Journal of Chemical Technology and Biotechnology, **82**, 847–855 (2007). DOI: 10.1002/jctb.1751

[72] Noda I.: Process for recovering polyhydroxyalkanotes using air classification. U.S. Patent 5849854, USA (1998).

[73] Jung I. L., Phyo K. H., Kim K. C., Park H. K., Kim I. G.: Spontaneous liberation of intracellular polyhydroxybutyrate granules in *Escherichia coli*. Research in Microbiology, **156**, 865–873 (2005). DOI: 10.1016/j.resmic.2005.04.004

[74] Luque de Castro M. D., Jiménez-Carmona M. M.: Where is supercritical fluid extraction going? TrAC Trends in Analytical Chemistry, **19**, 223–228 (2000). DOI: 10.1016/S0165-9936(99)00228-9

eXPRESS Polymer Letters Vol.5, No.7 (2011) 635–642
Available online at www.expresspolymlett.com
DOI: 10.3144/expresspolymlett.2011.61

Studies on single polymer composites of poly(methyl methacrylate) reinforced with electrospun nanofibers with a focus on their dynamic mechanical properties

K. P. Matabola[1,3], *A. R. de Vries*[2*], *A. S. Luyt*[3], *R. Kumar*[1]

[1]CSIR Materials Science and manufacturing, P. O. Box 1124, Port Elizabeth 6000, South Africa
[2]Department of Science and Technology, Private Bag X 894, Pretoria 0001, South Africa
[3]Department of Chemistry, University of the Free State (Qwaqwa Campus), Private Bag X 13, Phuthaditjhaba 9866, South Africa

Received 22 November 2010; accepted in revised form 18 January 2011

Abstract. The dynamic mechanical properties of single polymer composites of poly(methyl methacrylate) (PMMA) reinforced with electrospun PMMA nanofibers of different diameters are reported. The effect of electrospinning parameters on the morphology and diameters of the electrospun high molecular weight PMMA was investigated in order to obtain suitable diameters for the reinforcing fibers. Scanning electron microscopy (SEM) was used to study the morphology and diameters of the nanofibers produced at different electrospinning conditions. It was found that polymer solution concentration influences the diameter of the electrospun nanofibers more than the spinning voltage and spinning distance. SEM analysis of the PMMA nanofibers showed that the fibers had a smooth, regular and cylindrical morphology with no beads and junctions. Effects of the processing temperature for the preparation of the single polymer composites via film stacking were investigated. Dynamic mechanical analysis showed a pronounced improvement in the storage modulus of the composites compared to the matrix.

Keywords: *nanomaterials, electrospinning, poly(methyl methacrylate), single polymer composites*

1. Introduction

Single polymer composites refer to composites in which both reinforcements and matrix are from the same polymer, thereby supporting the ease of recyclability [1]. The concept was first described by Capiati and Porter [2] decades ago for high density polyethylene. Following their pioneering work, single polymer composites have been successfully manufactured for a variety of different semi-crystalline and amorphous polymers, including polyethylene [3], polypropylene [4], poly(ethylene napthalate) [5], poly(lactic acid) [6], polyamide [7] and poly(methyl methacrylate) (PMMA) [8–9]. Several techniques have been reported for the production of these composites, such as film-stacking [10] which will be used in this study, hot compaction [11] and co-extrusion [12]. The underlying basis of the techniques is to set a suitable processing window that utilises the difference in the melting temperature of the reinforcement and the matrix [13]. The small difference in melting temperature between the fiber and the matrix poses a challenge during fabrication. To overcome this problem, polymers with the same chemical composition but different chemical structure than the fiber were mostly used [14]. PMMA single polymer composites with improved mechanical properties [8–9] were produced by hot compaction utilising the melt spun micron-size fibers.

*Corresponding author, e-mail: andrew.devries@dst.gov.za

Unlike the single polymer composites involving semi-crystalline polymers, PMMA single polymer composites are unique in the sense that they were fabricated from amorphous PMMA with sufficient amount of molecular orientation [8]. Our hypothesis is that the composite performance can further be improved by using PMMA nanofibers and these fibers can be produced by the electrospinning technique.

Electrospinning is one of the recently recognised fields of nanoscience and nanotechnology that has the potential to produce polymer nanofibers [15–18]. Although many reports are already available on PMMA electrospun nanofibers, PMMA of much lower molecular weight was used in these studies [19, 20]. It is assumed that PMMA of higher molecular weight would serve as better reinforcement in single PMMA composites than those of lower molecular weight.

In this work, PMMA nanofibers of different diameters were produced by electrospinning technique and are used as reinforcements in PMMA single polymer composites. Effects of electrospinning parameters on the morphology and diameter of the nanofibers were investigated by scanning electron microscopy (SEM). The composites were manufactured by the film stacking technique applying a two-component approach and the properties of the composites were assessed by dynamic mechanical analyser (DMA).

2. Experimental

2.1. Materials

High molecular weight PMMA ($PMMA_{high}$, M_w = 996 000 g/mol) was purchased from Sigma Aldrich (Schenelldorf, Germany). N,N-dimethylformamide (DMF) and tetrahydrofuran (THF) were obtained from Sigma Aldrich (Schenelldorf, Germany) and Labscan Analytical Sciences (Gliwice, Poland), respectively, and used without any further purification. Polymer solutions for the electrospinning of $PMMA_{high}$ were prepared by dissolving 4, 5 and 6 wt% PMMA in a 1:1 THF:DMF solvent mixture. The electrospun $PMMA_{high}$ nanofibers were used as the reinforcing phase and a low molecular weight PMMA ($PMMA_{low}$, 90 000 g/mol, Altuglass V825-TL grade) purchased from Advanced Polymers (Altuglass International, Rho (MI), Italy) was used as the matrix material.

2.2. Electrospinning process

In the electrospinning process, $PMMA_{high}$ solutions were placed in a 5 ml syringe and gravity-fed through the tip. A copper wire was inserted into the polymer solution to act as a positive electrode. A high voltage supply, manufactured at University of Stellenbosch, Cape Town, South Africa, was used to charge the polymer solution, which resulted in an accelerated fluid jet towards a grounded aluminium collector. The electrospinning voltages used were 10, 15, 20 and 25 kV at a spinning distance of 10 and 15 cm. The electrospinning process was done in a horizontal mode in a fume hood at room temperature.

2.3. Composite preparation

The $PMMA_{low}$ pellets were dried in an oven at 60°C for 12 h before use. They were compression moulded to a film (layer thickness of 0.80 mm) on a CSIR (Port Elizabeth, South Africa) in-house compression moulding machine at a temperature of 200°C and a pressure of 2.5 bar. Two layers of nanofiber mats were sandwiched in-between four layers of a PMMA film sandwich structure. The sandwich material was then placed between two plates separated by two teflon sheets and compression moulded for 10 min at a low pressure (0.5 bar) and for 5 min at a higher pressure (2.5 bar). The processing temperatures used were 140, 150 and 160°C, respectively at constant pressure and holding time. After compression moulding, the samples were water-cooled under pressure for 7 min.

2.4. Characterization

The morphology of the resulting $PMMA_{high}$ nanofibers was characterised by SEM. A Gemini LEO 1525 FE-SEM (Carl Zeiss NTS GmbH, Germany) at an accelerating voltage of 5 or 10 kV using an In-lens detector was used. Before the observation, the fibers were coated with a 20 nm layer of evaporated carbon using an Emitech K950X evaporator (Quorum Technologies, Kent, UK). SEM analysis was also used to determine the intactness of the nanofibers on the cross-sectional area of the PMMA single polymer composites. The samples were prepared by fracturing under 3-point bending. Differential scanning calorimetry (DSC) was carried out with a Perkin Elmer DSC 7 (Life and Analytical Science, Shelton, USA) under nitrogen atmosphere. About

5 mg of sample was hermetically sealed in an aluminium pan for the measurements. The DSC samples were heated from 25 to 330°C at a heating rate of 10°C/min. The dynamic mechanical properties of the composite samples were determined using a Perkin Elmer DMA 8000 (Life and Analytical Science, Shelton, USA) in a dual cantilever bending mode at a frequency of 1 Hz and a scan rate of 2°C/min. The temperature was varied from room temperature to 160°C. The sample dimensions were 50 mm×9 mm×4 mm.

3. Results and discussion

3.1. Electrospinning of PMMA nanofibers

The influence of polymer solution concentration, applied voltage and spinning distance on the morphology and diameters of the electrospun $PMMA_{high}$ nanofibers were investigated in order to obtain nanofibers of different diameters. This is important for studying the effect of the fiber diameter on the properties of the single polymer composites of PMMA. Effects of various parameters on the morphology and diameter of the electrospun fibers are discussed.

Effect of PMMA concentration

The polymer solution concentration determines the spinnability of a solution [21]. The concentrations examined in this study were 4, 5 and 6 wt% $PMMA_{high}$ in a DMF/THF solvent mixture. The average fiber diameters were determined from measuring the diameters of 40 individual fibers. It can be seen from Table 1 that the fiber diameter increases with an increase in polymer solution concentration. The smaller diameter of the nanofibers from the lower concentrations is the result of the solution being stretched easily during electrospinning. The larger nanofiber diameters at high concentrations are attributed to the viscosity of the solution that was high enough to lower the bending instability of the jet. The solution becomes resistant to stretching by the electrical charges on the electrospinning jet [22].

Figure 1 shows the electron micrographs of the nonwoven fiber mats electrospun from 4, 5 and 6 wt% $PMMA_{high}$ solutions at a voltage of 15 kV onto an electrically grounded electrode positioned 10 cm from the syringe tip. The SEM images show the presence of fibers in the 200 to 900 nm range with smooth, regular and cylindrical morphology. No beads and junctions were observed in the fibers.

Effect of applied voltage

Table 1 shows the correlation between the fiber diameter and the applied voltage of the PMMA fibers electrospun at a spinning distance of 10 and 15 cm.

Table 1. Effect of different electrospinning parameters on the diameters of PMMA fibers obtained from $PMMA_{high}$ polymer solution

Applied voltage [kV]	4 wt%		5 wt%		6 wt%	
	Average diameter [nm] of PMMA nanofibers at two different spinning distances					
	10 cm	15 cm	10 cm	15 cm	10 cm	15 cm
10	348±57	220±46	589±89	665±103	1091±297	906±141
15	**286±36**	**307±50**	**624±86**	**708±87**	**854±244**	**909±159**
20	348±62	344±85	553±93	586±65	838±175	897±125
25	323±42	304±39	561±98	415±44	839±121	772±164

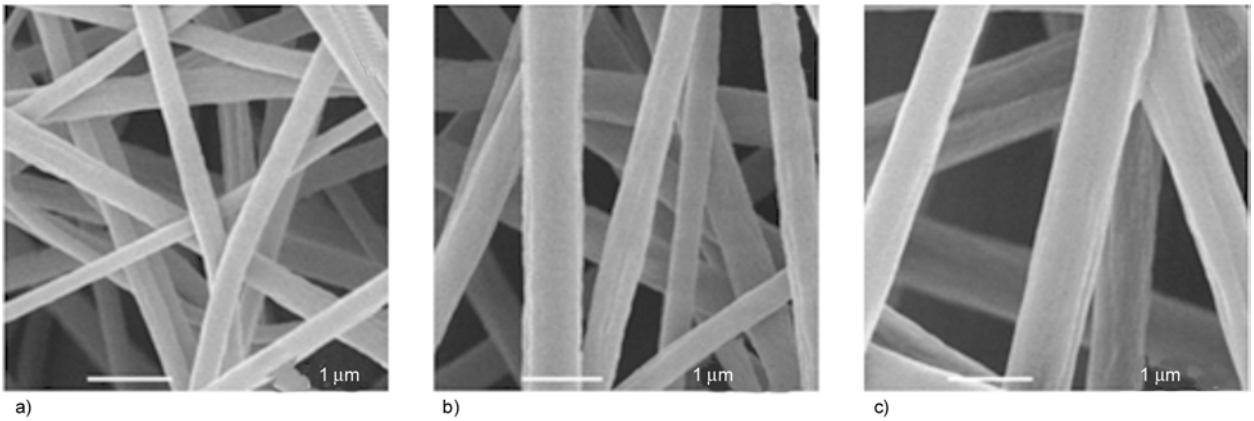

Figure 1. SEM images of (a) 200–400 nm, (b) 400–650 nm and (c) 600–900 nm electrospun $PMMA_{high}$ fibers

It can be seen that an increase in the applied voltage resulted in a decrease in the fiber diameter for the more concentrated PMMA solution (6 wt% PMMA) at a shorter spinning distance (10 cm). No significant changes in the diameters of the less concentrated solutions were observed, however, decreased fiber diameters were observed particularly at higher voltages. The decrease in fiber diameter with an increase in the spinning voltage became more noticeable at increased spinning distance (Table 1). The effect was observed for the more concentrated polymer solutions (5 and 6 wt% PMMA).

Effect of spinning distance

It can be seen from Table 1 that an increase in the spinning distance generally seemed to favour the production of nanofibers with slightly reduced diameters in this instance, depending on the spinning voltage. Some researchers mentioned that an increase in spinning distance resulted in a significant reduction in the diameter of the fibers for different polymers, including PMMA of a significantly lower molecular weight [23]. This indicates that different polymers or different molecular weights of the same polymer behave differently towards changing of the electrospinning parameters.

3.2. Thermal analysis of electrospun PMMA nanofibers

Differential scanning calorimetry (DSC) was done on the electrospun PMMA nanofibers in order to determine the thermal behaviour of the nanofibers. The results are presented in Figure 2. It can be seen from Figure 2 that the glass transitions (T_g) of the PMMA nanofibers and the PMMA matrix sheet are not clearly visible as compared to the neat powder. However, the DMA (discussed in section 3.3) shows the clear indication of the T_g of the matrix. Moreover, it is indicated that the nanofibers and the PMMA matrix sheet are thermally more stable than the as-received high molecular weight PMMA powder.

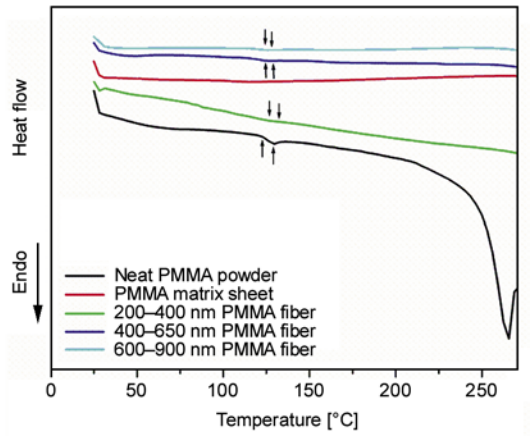

Figure 2. DSC results of $PMMA_{high}$ powder, $PMMA_{high}$ nanofibers and PMMA matrix sheet

3.3. PMMA single polymer composites

Investigation of processing conditions for single polymer composites of PMMA

The effect of the processing temperature on the morphology of the composites was investigated. The aim was to find a suitable processing temperature for the preparation of a quality PMMA single polymer composite. Since PMMA is amorphous, the amount of orientation (although not determined in this study) in the electrospun nanofibers will determine the processing window. SEM analysis of the cross-sections of the PMMA composites was used to check the intactness of the nanofibers and the integrity of the interface between the matrix and the reinforcement. $PMMA_{high}$ nanofibers with a diameter ranging from 400–650 nm were used to investigate suitable processing conditions for preparing single polymer composites of PMMA. $PMMA_{low}$ was used as the matrix material.

Figure 3 shows the SEM images of the composites prepared at 140, 150 and 160°C. The processing temperatures are well above the glass transition (T_g) of PMMA. The SEM images of the composites prepared at 140 and 150°C show two phases. Thus, the composites have a layered structure consisting of outer film layers and a layer in-between, which is associated with the non-woven nanofiber mats plus the softened matrix which has diffused on nonwoven fiber mat. Possible partial softening of the surface of the non-woven fiber mat is present. This results in a good interface, which should translate into enhanced mechanical properties as a result of efficient stress transfer. The SEM images seem to be in agreement with the previous study of Capiati and Porter [2]. It is likely that the layered structure observed for the composites is due to a combination of two composite fabrication methods, namely film stacking and hot compaction. Hine *et al.* [24] demonstrated that such a combination of film stacking with hot compaction results in a better overall balance of mechanical properties and a wider tempera-

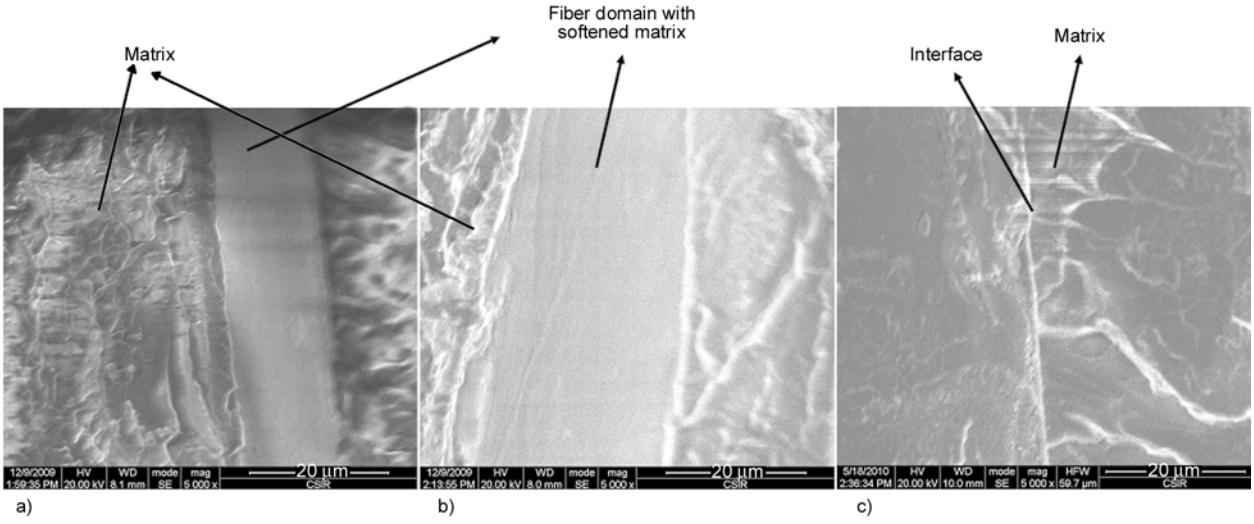

Figure 3. SEM images (scale bar: 20 µm) of PMMA single polymer composites prepared at (a) 140°C, (b) 150°C and (c) 160°C

ture range for processing compared to a standard compaction procedure without a film. Furthermore, this combination gives rise to better wetting of the reinforcement compared to the traditional film stacking process, due to the partial melting of the entire fiber surface. This better wetting of the fibers results in good interfacial adhesion between the phases, which can be seen from the SEM images in Figure 3.

However, delamination between the different matrix layers for the composites prepared at 140°C was observed. This was due to insufficient softening of the matrix material at a processing temperature of 140°C. The SEM analysis of the composite samples prepared at 160°C does not show two well-defined phases (Figure 3c). This suggests that the nanofibers could have also softened in addition to the matrix. Thus, a processing temperature of 160°C does not seem to be suitable for the preparation of the PMMA single polymer composites. The best composite with two distinguishable physical phases with adequate melting of the matrix material was therefore obtained at a processing temperature of 150°C.

Dimension of the layer related to the non-woven fiber mat, as observed from Figure 3, is around 10 to 15 µm. On the other hand, the diameter of the non-woven PMMA fibers was found to be around 200–900 nm (Figure 1 and Table 1). Differences in the nanofiber dimensions, as visualised in Figures 1 and 3, are explained by Figure 4. Before compression moulding, non-woven PMMA fibers mats are entangled among themselves (left hand side of Figure 4). For preparing single polymer composite, PMMA sheets are stacked above and below the non-woven mat. Under pressure, PMMA matrix softens and fills the vacant spaces around non-woven fiber mat.

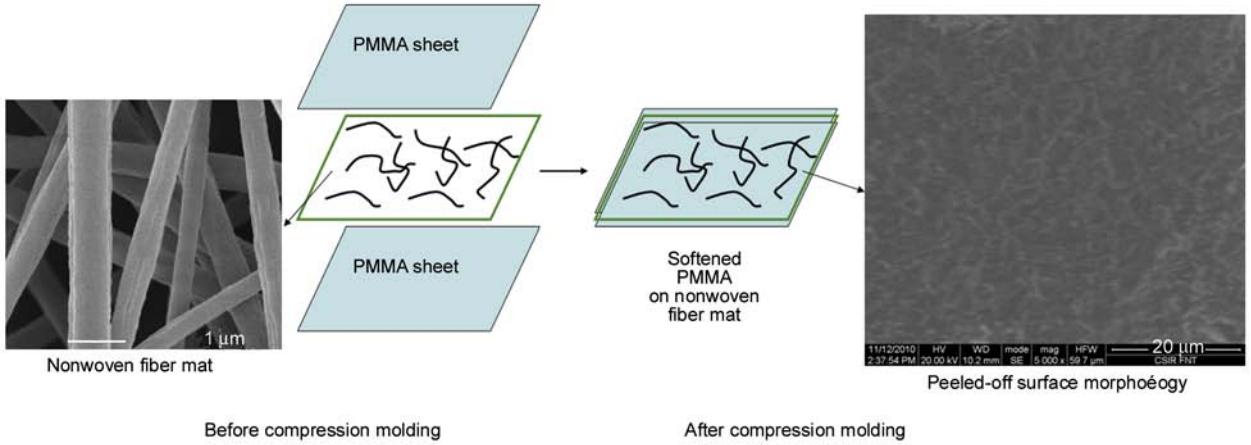

Figure 4. The appearance of PMMA nanofiber non- woven mat in single polymer composites system after compression molding. Scale bar for peeled-off picture is 20 µm.

SEM morphology of peeled-off structure after compression moulding (right hand side of Figure 4) demonstrates the presence of softened PMMA as well as non-woven PMMA mat. However, these nanofibers are hidden when the cross-section morphology of the composites are taken. This is attributed to the absence of fiber pull-out from the matrix when fractured.

Preparation and characterisation of single polymer composites of PMMA

The effects of the nanofiber diameter and nanofiber loading on the dynamic mechanical properties of six different types of PMMA single polymer composites prepared at 150°C were investigated. The nanofiber reinforcements consisted of three different fiber diameter ranges at two different loadings. The nanofibers electrospun at 15 kV and 10 cm at the various concentrations were used to prepare the single polymer composites (Table 1, conditions in bold font). Designations for six different types of composites are presented in Table 2.

The change in storage modulus and damping behaviour (tanδ) of the neat PMMA matrix compared to the composites SPC01 to SPC03 with 5 wt% nanofiber loading are shown in Figure 5. A slightly higher stiffness was observed for SPC01 and SPC02 compared to the neat PMMA matrix. A significantly higher reinforcing affect of the higher diameter fibers at a loading of 5 wt% was observed. Composite SPC03 showed an increase in stiffness of approximately 46% compared to the neat PMMA matrix. A slight increase in the peak temperatures of the tanδ peaks of the composites compared to the neat PMMA matrix was observed (Figure 5b). This increase is once again more noticeable in SPC03. This means that the inclusion of the nanofibers affected the mobility of the polymer chains to some degree. Furthermore, at a 5 wt% inclusion of the nanofibers, no significant shift in the peak temperature is observed for SPC01 and SPC02 compared to the neat PMMA matrix. However, the peak temperature shifted marginally by about 4°C in the case of SPC03 compared to the matrix. This means that there is stronger physical interaction between the higher diameter nanofibers and the neat PMMA matrix.

The storage modulus and damping behaviour (tanδ) of the neat PMMA matrix compared to the composites SPC04 to SPC06 with 10 wt% nanofiber loading are shown in Figure 6. The stiffness of all the composites was higher than that of the neat PMMA matrix. A maximum improvement in stiffness of 83% compared to the matrix was obtained. This is due to the reinforcing effect of the nanofibers. Different stiffness and damping behaviour was observed for the composites with 10 wt% nanofiber loading compared to the ones with a 5 wt% nanofiber loading. The composites (SPC04 and SPC05) reinforced with fibers of smaller diameters showed a larger improvement in stiffness compared to the one reinforced with the highest diameter fibers. This is con-

Table 2. Designations of PMMA single polymer composites

Sample designation	Matrix	Reinforcement by	
		5 wt% of PMMA nanofibers [nm]	10 wt% of PMMA nanofibers [nm]
SPC01	PMMA sheet	200–400	NA
SPC02		400–650	NA
SPC03		600–900	NA
SPC04		NA	200–400
SPC05		NA	400–650
SPC06		NA	600–900

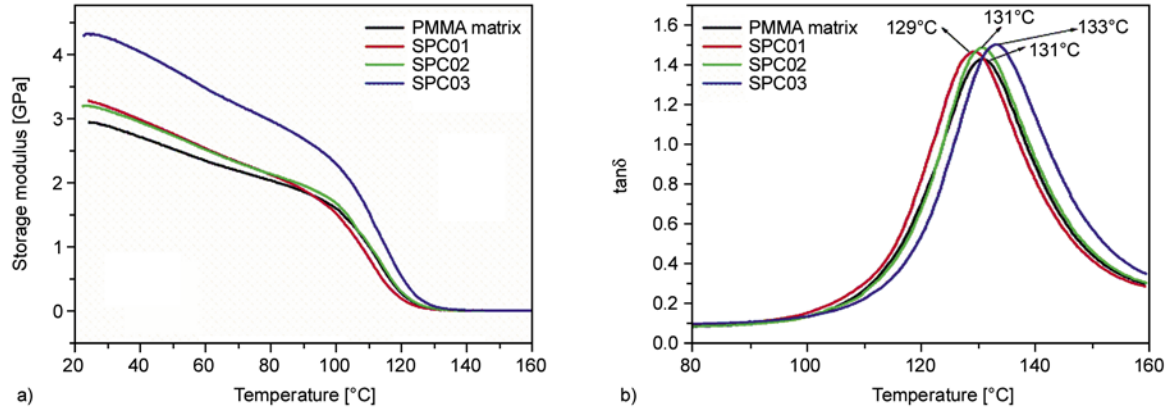

Figure 5. Effect of fiber diameter on the storage modulus (a) and tanδ (b) for PMMA composites at 5 wt% nanofiber loading and processing temperature of 150°C

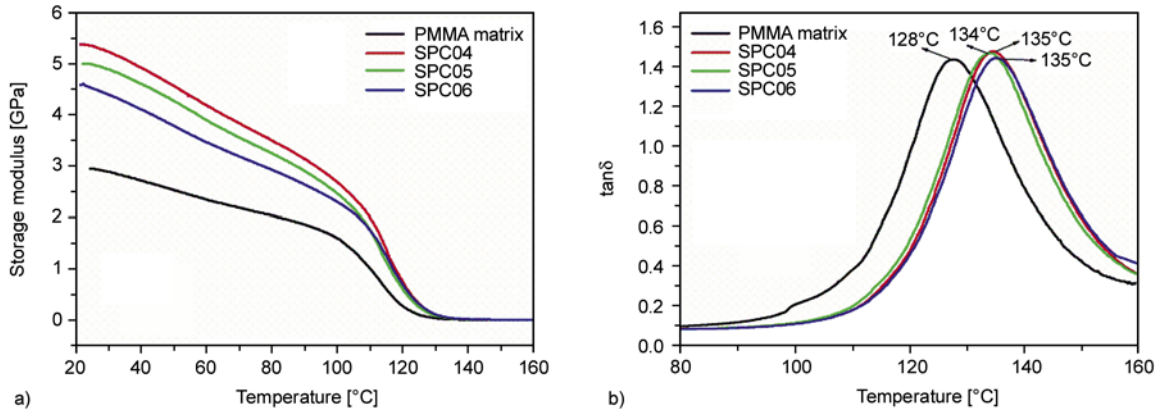

Figure 6. Effect of fiber diameter on the storage modulus (a) and tanδ (b) for PMMA composites at 10 wt% nanofiber loading and processing temperature of 150°C

trary to what was observed for the composites with a 5 wt% nanofiber loading. This is probably as a result of the higher fiber content and the larger surface area of the nanofibers with smaller diameters. In this case an increase in the stiffness of the composites is observed as the diameter of the reinforcement decreases. In addition, a less pronounced decrease in the stiffness of all the composites compared to the neat PMMA matrix was observed. Figure 6b shows the damping behaviour of the neat PMMA matrix compared to the composites reinforced with a 10 wt% nanofiber loading. Similar damping behaviour is observed for all the composites. The addition of a 10 wt% nanofiber loading had no significant effect on the maximum value of the tanδ peaks of the composites. Thus, the mobility of the polymer chains in the matrix and the composites are quite similar. Nevertheless, the position of the T_g of the composites shifted to higher temperatures as compared to the PMMA matrix. This shift to higher temperatures is attributed to the increase in the stiffness of the composites due to reinforcement effect of the nanofibers.

4. Conclusions

In this study, the effects of processing parameters on the morphology of electrospun PMMA fibers have been investigated. PMMA nanofibers with diameters ranging from 200–900 nm were prepared under various conditions. The SEM analysis of the PMMA nanofibers showed that the fibers had a smooth, regular and cylindrical morphology with no beads and junctions. The spinning voltage and the spinning distance, in general, did not have a significant influence on the morphology and diameters of the fibers. However, an increase in polymer solution concentration resulted in a significant increase in fiber diameter. The processing conditions for the preparation of single polymer composites of PMMA were investigated. It was determined that a processing temperature of 150°C was adequate for the preparation of a good composite because at this temperature distinct layer of fibers and matrix were observed. The composites generally showed an improvement in dynamic mechanical properties compared to the neat PMMA matrix. The increases in the stiffness (up to 83%) and glass transition temperatures (up to 10°C) of the composites were pronounced in the case of a 10 wt% nanofiber loading.

Acknowledgements

The author would like to thank Mrs. Valencia Jacobs for SEM analysis and Council for Scientific and Industrial Research of South Africa for financial assistance.

References

[1] Kmetty A., Bárány T., Karger-Kocsis J.: Self-reinforced polymeric materials: A review. Progress in Polymer Science, **35**, 1288–1310 (2010). DOI: 10.1016/j.progpolymsci.2010.07.002

[2] Capiati N. J., Porter P. S.: The concept of one polymer composites modelled with high density polyethylene. Journal of Materials Science, **10**, 1671–1677 (1975). DOI: 10.1007/BF00554928

[3] Mosleh M., Suh N. P., Arinez J.: Manufacture and properties of a polyethylene homocomposite. Composites Part A: Applied Science and Manufacturing, **29**, 611–617 (1998). DOI: 10.1016/S1359-835X(97)00122-X

[4] Loos J., Schinanski T., Hofman J., Peijs T., Lemstra P. J.: Morphological investigations of polypropylene single-fibre reinforced polypropylene model composites. Polymer, **42**, 3827–3834 (2001). DOI: 10.1016/S0032-3861(00)00660-1

[5] Hine P. J., Astruc A., Ward I. M.: Hot compaction of polyethylene naphthalate. Journal of Applied Polymer Science, **93**, 796–802 (2004). DOI: 10.1002/app.20517

[6] Li R., Yao D.: Preparation of single poly(lactic acid) composites. Journal of Applied Polymer Science, **107**, 2909–2916 (2008). DOI: 10.1002/app.27406

[7] Gong Y., Yang G.: All-polyamide composites prepared by resin transfer molding. Journal of Materials Science, **45**, 5237–5243 (2010). DOI: 10.1007/s10853-010-4565-6

[8] Wright D. D., Lautenschlager E. P., Gilbert J. L.: Bending and fracture toughness of woven self-reinforced composite poly(methyl methacrylate). Journal of Biomedical Materials Research, **36**, 441–453 (1997). DOI: 10.1002/(SICI)1097-4636(19970915)36:4<441::AID-JBM2>3.0.CO;2-E

[9] Wright-Charlesworth D. D., Lautenschlager E. P., Gilbert J. L.: Hot compaction of poly(methyl methacrylate) composites based on fiber shrinkage results. Journal of Materials Science: Materials in Medicine, **16**, 967–975 (2005). DOI: 10.1007/s10856-005-4431-2

[10] Bárány T., Karger-Kocsis J.: Development and characterization of self-reinforced poly(propylene) composites: Carded mat reinforcement. Polymers for Advanced Technologies, **17**, 818–824 (2006). DOI: 10.1002/pat.813

[11] Hine P. J., Ward I. M., Jordan N. D., Olley R., Bassett D. C.: A comparison of the hot-compaction behavior of oriented, high-modulus, polyethylene fibers and tapes. Journal of Macromolecular Science: Physics, **40**, 959–989 (2001). DOI: 10.1081/MB-100107570

[12] Alcock B., Cabrera N. O., Barkoula N-M., Reynolds C. T.: The effect of temperature and strain rate on the mechanical properties of highly oriented polypropylene tapes and all-polypropylene composites. Composites Science and Technolology, **67**, 2061–2070 (2007). DOI: 10.1016/j.compscitech.2006.11.012

[13] Bárány T., Izer A., Karger-Kocsis J.: Impact resistance of all-polypropylene composites composed of alpha and beta modifications. Polymer Testing, **28**, 176–182 (2009). DOI: 10.1016/j.polymertesting.2008.11.011

[14] Yao D., Li R., Nagarajan P.: Single-polymer composites based on slowly crystallizing polymers. Polymer Engineering and Science, **46**, 1223–1230 (2006). DOI: 10.1002/pen.20583

[15] Dzenis Y.: Spinning continuous fibers for nanotechnology. Science, **304**, 1917–1919 (2004). DOI: 10.1126/science.1099074

[16] Li D., Xia Y.: Electrospinning of nanofibers: Reinventing the wheel? Advanced Materials, **16**, 1151–1170 (2004). DOI: 10.1002/adma.200400719

[17] Teo W. E., Ramakrishna S.: A review on electrospinning design and nanofibre assemblies. Nanotechnolgy, **17**, 89–106 (2006). DOI: 10.1088/0957-4484/17/14/R01

[18] Formhals A.: Process and apparatus for preparing artificial threads. U.S. Patent 1975504, USA (1934).

[19] Liu J., Kumar S.: Microscopic polymer cups by electrospinning. Polymer, **46**, 3211–3214 (2005). DOI: 10.1016/j.polymer.2004.11.116

[20] Wang H., Li Q., Yang Q., Li Y., Wang W., Sun L., Zhang C., Li Y.: Electrospun poly(methyl methacrylate) nanofibers and microparticles. Journal of Materials Science, **45**, 1032–1038 (2010). DOI: 10.1007/s10853-009-4035-1

[21] Sill T. J., von Recum H. A.: Electrospinning: Applications in drug delivery and tissue engineering. Biomaterials, **29**, 1989–2006 (2008). DOI: 10.1016/j.biomaterials.2008.01.011

[22] Jacobs V., Anandjiwala R. D., Maaza M.: The influence of electrospinning parameters on the structural morphology and diameter of electrospun nanofibers. Journal of Applied Polymer Science, **115**, 3130–3136 (2010). DOI: 10.1002/app.31396

[23] Doshi J., Reneker D. H.: Electrospinning process and applications of electrospun fibers. Journal of Electrostatics, **35**, 151–160 (1995). DOI: 10.1016/0304-3886(95)00041-8

[24] Hine P. J., Olley R. H., Ward I. M.: The use of interleaved films for optimising the production and properties of hot compacted, self reinforced polymer composites. Composites Science and Technology, **68**, 1413–1421 (2008). DOI: 10.1016/j.compscitech.2007.11.003

eXPRESS Polymer Letters Vol.5, No.7 (2011) 643–652
Available online at www.expresspolymlett.com
DOI: 10.3144/expresspolymlett.2011.62

Hollow fibers made from a poly(3-hydroxybutyrate)/poly-ε-caprolactone blend

C. Hinüber[1,2*], *L. Häussler*[1], *R. Vogel*[1], *H. Brünig*[1], *G. Heinrich*[1,3], *C. Werner*[1,2,4]

[1]Leibniz-Institut für Polymerforschung Dresden e.V., Hohe Str. 6, D-01069 Dresden, Germany
[2]Max Bergmann Zentrum für Biomaterialien Dresden, Budapester Str. 27, D-01069 Dresden, Germany
[3]Technische Universität Dresden, Institut für Werkstoffwissenschaft, Helmholtzstrasse 7, D-01069 Dresden, Germany
[4]Technische Universität Dresden, Zentrum für Regenerative Therapien Dresden, Tatzberg 47, D-01187 Dresden, Germany

Received 2 November 2010; accepted in revised form 20 January 2011

Abstract. Since poly(3-hydroxybutyrate) (PHB) is inherently brittle and possesses poor elastic properties, hollow fibers produced by melt spinning from pure PHB, as described in our earlier study [Macromolecular Materials and Engineering, 2010, 295/6, 585–594], do not meet the required needs regarding the mechanical performance. Besides hardly available PHB copolymers, also blend systems are known to enhance material properties and have thus been considered to be eligible to fabricate *flexible* or rather pliable hollow fibers based on PHB. Blends of PHB and poly-ε-caprolactone (PCL) are promising for the application in tissue engineering due to the inherent biocompatibility and biodegradability. A wide range of PHB/PCL compositions have been prepared by melt extrusion. Thermal and mechanical properties of the obtained specimens were analyzed in order to identify miscibility and degree of dispersion as well as to determine the influence on the overall mechanical performance. Even though these constituents are known to be immiscible, PHB/PCL 70/30 was proven to be an adequate composition. This blend showed a highly increased elongation and was found to be easily processable by melt spinning compared to pure PHB. From this blend well defined dimensionally stable bendable hollow fibers were fabricated.

Keywords: *biodegradable polymers, mechanical properties, PHB, PCL, melt spinning*

1. Introduction

Poly(3-hydroxybutyrate) (PHB), produced by microorganisms in order to store carbon as energy resource, is a promising material for applications requiring biocompatibility, non-toxicity as well as biodegradability [1, 2]. Therefore, investigating, developing and modifying PHB based materials are of great interest in regenerative medicine. In earlier studies it was shown that PHB can be fabricated to multifilament fibers with textile properties using a high-speed melt spinning and drawing technology and further processed into textile scaffolds and wound healing patches [3–6]. Recently, we demonstrated that dimensionally stable hollow fibers from PHB can be spun [7].

For instance, latest concepts in neuro-tissue engineering call for biocompatible, biodegradable and biofunctionalized polymers as temporary nerve guidance conduits. The strategies in neurosurgery tend to treat nerve injuries by means of tubulization techniques to initiate and stimulate nerve regeneration as explained in detail by Battiston *et al.* [8], and Ruiter *et al.* [9]. According to these authors, an ideal nerve guidance conduit performs better than an autograft, offering at least following features: biocompatibility; a biodegradable, non toxic mate-

*Corresponding author, e-mail: hinueber@ipfdd.de

rial; certain flexibility and certain porosity that guarantees permeation of nutrients and oxygen but avoids ingrowth of competitive cells. Besides this, an internal framework or a multichannel structure is regarded beneficial [9, 10]. Furthermore, a defined biomolecular functionalization including appropriate growth factors and/ or cells (e.g. Schwann cells) seems to be essential [11, 12]. Various degradable materials are under investigation: e. g. Matrigel, Collagen, PLLA, PLGA, PCL [9, 13, 14]. However, tubular structures made of very soft or fast degrading materials might collapse or kink before regeneration has been completed and will strongly constrict or even obstruct tissue regeneration [15]. Since PHB is a stiff and rather slowly degrading biopolymer, it has received more attention in neuronal regeneration research [11, 16, 17]. In contrary to time-consuming manual methods providing three dimensional structures via solvent casting methods, dip coating, wrapping of sheets or braiding of fibers around canules, the thermoplastical processability of PHB allows for a fast and continuous production of tube-like structures via melt spinning, which is the most efficient process to produce fibers [7]. Despite of brittleness and thermooxidative degradation, the feasibility of spinning dimensionally stable hollow fibers from PHB was shown for the first time. However, the main drawback of this material, poor mechanical performance due to its inherent rigidity, still remains an issue. Therefore, the following study addresses the modification of PHB to significantly enhance ductility. Besides PHB-copolymers exhibiting good elastic properties, blending with certain biopolymers seems to be a reasonable option. Blending is a known physical method to vary and tailor material properties by mixing two homopolymer components either in molten or in dissolved state. The aim of blending is to achieve intermediate or even superior properties while preserving the major characteristics of the pure components.

PHB has been blended with several other biocompatible and biodegradable polymers, for instance poly(ethylene oxide), poly (L-lactide), poly (L-lactic acid) or poly-ε-caprolactone (PCL), in order to improve weak properties [18, 19]. PCL in particular, a synthetic semicrystalline polyester also belonging to the category of biocompatible and biodegradable polymers, is considered as an interesting blend component due to the high ductility and thermal resistance. In fact, the melting temperature of PCL is significantly lower compared to PHB but PCL does not undergo rapid thermal degradation, hence processing far above melting temperature is not critical. PCL is generally miscible with a wide variety of polymers acting as a plasticizer and leading to a more flexible material by lowering the glass transition temperature (T_g) and the Young's modulus (E). However, PCL is known to be immiscible with PHB when blended mechanically or in solution and thus considered not to improve mechanical properties in case of PHB [18, 20–23]. Nevertheless, this blend system is highly discussed in literature due to results that are reported on the attempts to improve miscibility leading to increased ductility and also to tailor degradability. Avella *et al.* reported about physically blended PHB and PCL. No synergetic effects have been found and material performance was not improved for blends with less than 60 wt% of PCL. Soft PCL droplets within the PHB phase did not lower the rigidity [18]. Contrary to these findings Lovera *et al.* [19] showed an increased elasticity. Even though the aim of this study was rather the investigation of the degradation behaviour than the improvement of the mechanical properties of these solution cast blends, tensile tests demonstrated that a PHB/PCL 70/30 blend shows elongation values at break of about 50% whereas pure PHB tolerates a strain of 10% only, for non-degraded state, respectively. Lovera et al. also tried to improve miscibility of the PHB/PCL blends by using a chemically modified low molecular weight PCL. Blends with chemically modified PCL were proven to be partly miscible and showed a reduced degradation rate which is interesting in terms of tailoring the blend properties. Avella *et al.* [18] also reported on miscibility when utilizing low molecular weight PCL. This article reports about the formation of hollow fibers by melt spinning using a particular PHB/PCL blend in order to achieve a bendable hollow structure that is applicable in regenerative medical therapies, for instance as nerve guidance conduit.

2. Experimental part

2.1. Materials

High molecular weight poly(3-hydroxybutyrate) (Biocycle® 1000, M_w = 349 000) was obtained from

Biocycle (São Paulo/Brazil). High molecular weight poly-ε-caprolactone (capa® 6800, PCL, M_w = 120 000) was purchased from Perstorp UK Ltd. (Warrington/ UK).

Since the used spinning set-up does not include an extrusion or mixing process and thermo-oxidative degradation influences PHB properties quickly, carefully mixing of both polymer components in non molten state is of crucial impact. Polymer blends were prepared by

a) simply mixing of granulates of both components,
b) milling and mixing of fine powder, as well as
c) using a solvent and applying a precipitation procedure.

For spinning experiments, granules of both polymers have been milled into fine powder using a Retsch two step rotor-sieve mill with a sieve size of 0.5 mm (Ultra Centrifugal Mill ZM 200, Retsch, Haan/ Germany). Since PCL is cereous, both polymers were cooled down in liquid nitrogen for 5–10 minutes before milling. Thus, the milling procedure was simplified by polymer embrittlement and smudging of the sieve was avoided. Beneficial to the preparation of a homogenous mixture both polymer components were purified and mixed by dissolution in chloroform at 40°C and precipitated in methanol. Precipitated polymer mixture was finally separated from solvents by filtration and vacuum dried (115°C, 24 h). Remaining polymer 'flakes' were compacted into 2.5 cm discs using a hydraulic press and cut into smaller pieces to allow for easy filling.

2.2. Methods

2.2.1. Sample preparation

For thermal analysis (DSC), visualization (SEM) as well as for mechanical characterization (tensile test) samples of PHB/PCL with varying compositions were compounded from granulates (G) using a micro-scale twin screw extruder (Micro 5, DSM Research, Delft/Netherlands): PHB/PCL G 100/0, G 90/10, G 80/20, G 70/30, G 60/40, G 50/50. Sample mass was about 3 g per run. Compounding parameters were set to: 185°C, 80 rpm and 2 min. Besides simple extrusion of 'worm-like' structures, fiber-like structures were extruded by using self-constructed nozzles. No drawing process was applied to these fibers as usually practiced for melt spinning fibers. Extruded fibers varied in diameter from 0.4 to 1.0 mm. For the purpose of comparison, also a sample from precipitated material (F 70/30) was compounded and prepared for DSC measurements.

2.2.2. Differential Scanning Calorimetry (DSC)

The thermal analysis was carried out using differential scanning calorimetry (Q1000, TA Instruments, Dallas/Texas/ USA) in inert nitrogen atmosphere. Calibration was performed with an indium standard. A fresh sample of the compounded material (~5 mg) was prepared for each DSC run. Pieces of adequate size were cut from the extruded strand. Data for a cycle of heating-cooling-heating were collected. All measurements were replicated to verify the collected data. Specimens were exposed to the following DSC regime:

First heating, cooling and second heating scans were performed in a temperature range from –60°C (kept for 5 min) to +185°C (kept for 2 min) with a heating/cooling rate of 20 $K \cdot min^{-1}$. The glass temperature (T_g), the peak temperatures of melting (T_m) and crystallization (T_c) and the onset temperature of crystallization (T_o) as well as the melting and crystallization enthalpy (ΔH_m, ΔH_c) were determined.

2.2.3. Tensile tests

In order to provide a first insight into the mechanical properties of the blends, specimens of extruded fibers with varying compositions were selected and prepared for tensile testing: PHB, PHB/PCL 90/10, 70/30, 50/50 from granulate material and additionally PHB/PCL 70/30 from precipitated material to determine the influence of pre-mixing of both components. Mechanical testing was performed with a standard testing machine from the company Zwick (UPM Z010 Zwick GmbH & Co. KG, Ulm/Germany). The tensile tests were carried out with an overall sample length was 60 mm and a gauge length of test specimens of 20 mm. The diameter was measured for each specimen separately as it varied from 0.4 to 1.0 mm. A defined preload of 0.1 N was applied on the specimen prior to the measurement. The crosshead speed was maintained at 10 mm/min. Tensile properties were calculated as mean value of at least 3 specimens from the obtained stress-strain curves, considering the varying diameter.

2.2.4. Scanning Electron Microscopy (SEM)

Scanning electron microscopy was performed with an environmental scanning electron microscope from Philips (XL30 ESEM-FEG, Philips Deutschland GmbH, Hamburg/Germany) in SEM (high-vacuum) mode. To investigate the morphology cross sections of the specimens (compounded PHB/PCL 70/30 from granulate, powder, precipitated material) were imaged. All specimens were submerged into liquid nitrogen and fractured or cut and then sputter-coated with a thin layer of gold before SEM observation.

2.2.5. Melt spinning

As a result of the investigation of extruded fibers, the transfer to melt spinning experiments was carried out for the PHB/PCL 70/30 blend only. Melt spinning tests were performed using a self-constructed plunger-piston spinning device:

The spinning device, a bi-component spinning system with plunger and piston, was formerly designed and utilized for core-shell fiber spinning. As described elsewhere, compressed air was filled in as core content instead of the second polymer component to fabricate continuous hollow fibers [7]. About 10 g of polymer mixture (granulate material, powder and precipitated material, respectively) was filled in the piston whereas the plunger was already positioned. The piston and plunger were connected to the spinning block and the set-up was heated up to 185°C. The spinneret is available in the dimension of 0.3/0.6 and 0.4/0.7 mm inner/outer diameter. The mass throughput of the spinneret was set to 0.5–1 $cm^3 \cdot min^{-1}$. The resulting spinning pressure was in a range of 30 up to 100 bar. Spun fibers were wound up on a bobbin with an up-take speed varying between 20 up to 100 $m \cdot min^{-1}$. To adjust the inner diameter and the wall thickness of the hollow fibers the up-take speed (draw down ratio) was varied [24, 25]. The higher the applied draw down ratio is set, the smaller the obtained tube diameter. A low dosage of compressed air was used as core component to generate a hollow structure during melt spinning.

3. Results and discussion

3.1. Thermal analysis

DSC measurements of compounded blend systems were conducted to investigate whether there is miscibility or phase segregation for a particular composition, and the influence of PCL on the crystallization behaviour of PHB. The second heating curves, shown in Figure 1, reflected the immiscibility by the occurrence of two glass transitions at temperatures according to that of the components. With increasing PCL content the glass transition of PHB was overlapped by the melting of PCL. In Figure 2 the cooling cycle for the pure components in comparison to several blends is shown. These measurements are in complete accordance with the findings of Lovera *et al.* [19]: PHB crystallization temperature is shifted from 116°C to significantly lower temperatures (varying from 101–104°C for G specimens) when blended with PCL, demonstrating the disturbing effect of PCL on the PHB crystallization. This may be explained by a transfer of heterogeneities from PHB to PCL during blending. The shift to lower T_c is even more distinct (T_c = 90°C for F 70/30) for F 70/30. This effect can be attributed to the removal of several heterogeneities during the preparation procedure in solution. When the total amount of heterogeneities is decreased while the transfer of these from PHB towards PCL occurs in

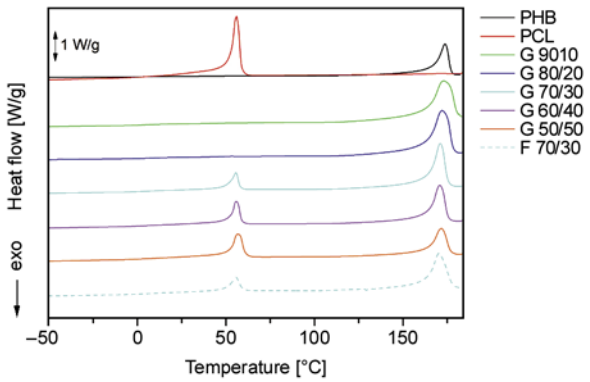

Figure 1. DSC second heating scans of pure PHB and pure PCL compared to PHB/PCL blends

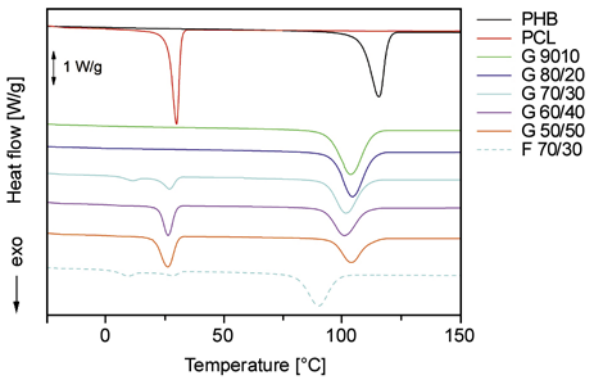

Figure 2. DSC cooling curves of pure PHB compared to PHB/PCL blends of varying composition

the same manner, PHB crystallization happens at significantly lower temperatures.

PCL crystallization is also shifted to lower temperatures for all blended specimens, indicating immiscibility. The G 90/10 as well as the G 80/20 blend shows a very small exotherm with $\Delta H_c \leq 0.5$ J/g for PCL at lower temperatures than the bulk crystallization. In G 70/30 as well as in F 70/30 two distinct PCL exotherms occur with lower crystallization temperatures compared to pure PCL. This phenomenon is referred as fractionated crystallization. The small effect of fractionated crystallization was also observed for the composition of PHB/PCL 65/35, but is not shown in Figure 2. The first crystallization step with lower supercooling corresponds to the bulk crystallization of PCL. The second one is a typical consequence of fine dispersed regions of the minor phase into isolated droplets within the matrix polymer. Nucleation is not induced at the same temperature for all PCL droplets. The crystallization takes place at different supercoolings due to the varying content and distribution of heterogeneities that are inherently existent and were donated by PHB within the dispersed droplets. The quantity of such crystallization steps varies and is dependent on the number and distribution of nucleating sites in the PCL phase. Notwithstanding that PHB and PCL are immiscible; it is assumed that a homogenously finely dispersed phase showing good interfacial adhesion could lead to improved properties.

For PHB/PCL 60/40 and 50/50 the phenomenon of fractionated crystallization is absent. Presumably in both blend systems both phases, PHB and PCL, coexist without droplet formation in a rather co-continuous alignment. Figure 2 shows well defined exotherms for both blends confirming the immiscibility of the components. The determined enthalpies verify the amount of both polymers, respectively.

3.2. Mechanical performance

Taking the results of the DSC measurement into account, samples of selected compositions have been chosen for the tensile tests. Extruded fibers have been evaluated: pure PHB, PHB/PCL 90/10, 70/30 and 50/50 from granulate mixture (G) as well as 70/30 from precipitated material (F) have been tested. The given values by Perstorp for the mechanical properties of PCL capa® 6800 have been verified. The aim of these measurements was to demonstrate and to prove the improved flexure of different blends compared to pure PHB and to chose a reasonable composition.

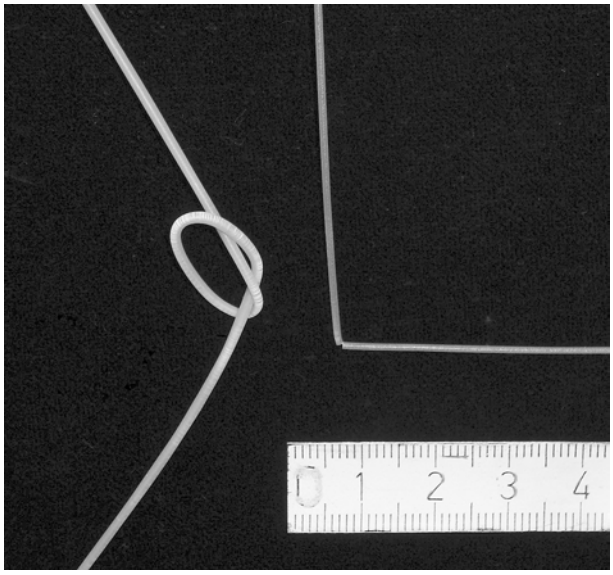

Figure 3. Image of extruded 'worm-like' structures to visualize the flexibility: left) PHB/PCL 70/30 (flakes) exhibits bendable properties, right) pure PHB shows brittle-fracture

A significant difference occurs in bending stiffness comparing PHB/PCL 70/30 with pure PHB, as demonstrated in Figure 3. Thinking of the desired application the tubular structure will neither be exposed to high tensile or compressive forces nor to extreme torsion or bending as demonstrated with this image. However, certain *flexibility* or rather pliability is required to prevent tubular structure from kinking or catastrophically failure. A bending test would be the optimal testing method to verify the improved characteristic. However, the available sample geometry (rod like structures) and the available testing equipment does not allow for appropriate standardized bending tests. Thus, tensile tests were carried out to demonstrate the tendency of an improved ductility, even though the bending stiffness was not measured directly.

At first view it seems that there is no significant improvement of ductility present when comparing PHB to the blends. The values for elongation at yield stress, shown in Figure 4 and listed in Table 1, are in a range of 2–4% for all measured specimens. However, to evidence an increased elasticity the elastic modulus (Young's modulus, E) shows a trend: E is clearly decreased with increasing PCL content

Table 1. Mechanical properties of pure components compared to extruded blend fibers

	Young's modulus [GPa]	Yield stress [MPa]	Elongation at yield stress [%]	Stress at break [MPa]	Elongation at break [%]
G PHB (n = 8)	1.5±0.06	26.5±1.4	2.9±0.3	25.9±1.5	3.1±0.5
G 90/10 (n =5)	1.5±0.17	25.5±1.8	2.6±0.2	21.8±1.3	11.3±4.9
G 70/30 (n = 5)	1.3±0.14	24.4±1.4	2.9±0.3	7.0±8.4	41.2±22.5
G 50/50 (n = 3)	1.1±0.19	22.8±0.4	3.6±0.7	27.0±3.6	630.9±271.8
F 70/30 (n = 7)	1.3±0.15	25.4±1.7	3.1±0.6	–	–
PCL (Perstorp)	0.5	16	–	54	920

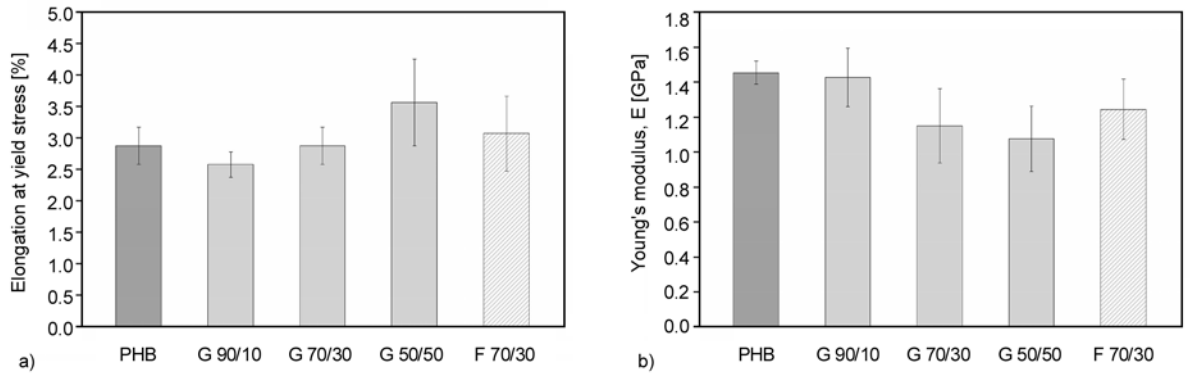

Figure 4. Mechanical properties determined from tensile tests: elongation at yield stress (a) and Young's modulus (b) (F = flakes from precipitated material; *given by Perstorp for capa® 8600)

as diagrammed with Figure 4. In order to understand and evaluate the determined values correctly some insight into the fracture behaviour needs to be given. It is known that PHB shows brittle-fracture, which is exactly what was observed within the test: maximal elongation (2.9%) is equal to the elongation at break (3.1%). The addition of 10 wt% PCL (G 90/10) already yields into an increased value for elongation at break. While elongation at yield stress is in the same range (2.6%) the elongation at break increased to 11.3%. Nevertheless, these specimens also show brittle-fracture.

However, the blend systems G 70/30 as well as G 50/50 show elongation with necking. Even though elongation at yield stress remains only about 3–4%, no brittle-fracture occurs in these cases, instead samples start to neck. For these specimens elongation at break is in the range from 10 up to 800%, respectively. Admittedly, a great variance occurs for the values of elongation at break for these blends. This might be explained by inhomogeneities in blend compositions and morphology that strongly affect the necking behaviour.

Considering the desired application, it is important to mention here that elongation at break is not required to be extremely high or even as high as for pure PCL (920 %). In this specific case it is necessary to prove that brittle-fracture can be prevented and a recognizable pliability can be obtained by blending PHB with PCL. The data for elongation at yield stress and the Young's modulus are in the similar range for G 70/30 compared to G 50/50. However, the failure behaviour differs since G 50/50 exhibits a significantly higher elongation at break (630.9%). Consequently, the addition of only 30 wt% of PCL is reasonable and adequate to adjust the desired characteristic in terms of avoiding brittle fracture and obtaining a bendable material. The aim of the study was the improvement of PHB properties by using a minimum amount of a second polymer.

Moreover, it needs to be mentioned that whitish horizontal stripes at macroscopic scale have been detected prior failure as it can be seen in Figure 3, indicating a certain material damage. The stripes occur at the knot sites for the regions of maximum of deformation; they are irreversible and are related to local crazing. Therefore, specimens can not be considered flexible but bendable.

To address the question of mixture homogeneity, which is essential for melt spinning, extruded fibers from precipitated material F 70/30 were compared to extruded fibers made from granulate material G 70/30. From the tensile test data no significant difference can be observed, except for elongation at break. No reliable data for elongation at break for

Figure 5. Compounded specimens from G 70/30 left (brownish) compared to F 70/30 (whitish) right

F 70/30 was measured because specimens showed failure out of gauge length in nearly all cases. Breaking behaviour can be considered similar to G 70/30: G 70/30 as well as F 70/30 showed elongation with necking instead of catastrophically failure. Both mixtures showed equal behaviour in terms of its bending properties.

As it is visualized in Figure 5, it is remarkable that precipitated blend material results into whitish almost transparent appearing samples, whereas compounded granules look brownish after compounding. Aesthetical optical appearance is definitively an issue in medical applications. Even more important is the well pre-mixed state of both components which is essential for further spinning experiments (see 2.3). Mixing of PHB and PCL in solution and subsequent precipitation leads to a well mixed state, to purification of the material and to the removal of low molecular constituents, which show higher sensibility to thermooxidative degradation. Thus, purified F 70/30 specimen exhibits a rather white appearance after compounding compared to the G 70/30 sample that contains more impurities and low molecular constituents.

3.3. Melt spinning

Finally, spinning experiments were conducted using the plunger-piston spinning device due to two advantages: first, the chance to use a minimum of material and the simplified handling of the spinning device compared to extrusion spinning and second the opportunity to spin at lower temperatures than 190°C to avoid thermooxidative degradation. Spinning of hollow fibers was successfully conducted at temperatures in the range of 183–185°C. As the premixing of blends is essential for spinning of homogenous fibers, different mixing states were tested: granulate material, powder and precipitated material. The spinning procedure for granulates as well as for powder mixture was instable and seemed to yield into segregation of both components during spinning. PCL melts at approximately 60°C, whereas PHB melting starts at 175°C. Thus, PCL melt already moves towards the nozzle by gravity yielding into phase segregation within the plunger. PHB/PCL 70/30 from precipitated material (F 70/30) did not show phase separation phenomena and thus melt spinning could be carried out successfully. Melt spinning of compacted flakes resulted in flexible hollow fibers of adequate optical and mechanical appearance. A SEM image of a hollow fibre is shown in Figure 6. Dimensionally stable and homogenous hollow fibers with smooth inner and outer tube surfaces have been fabricated. The rather flexible properties might be visualized by the soft cut leading to plastic deformation, which would not be visible for a brittle-fracture.

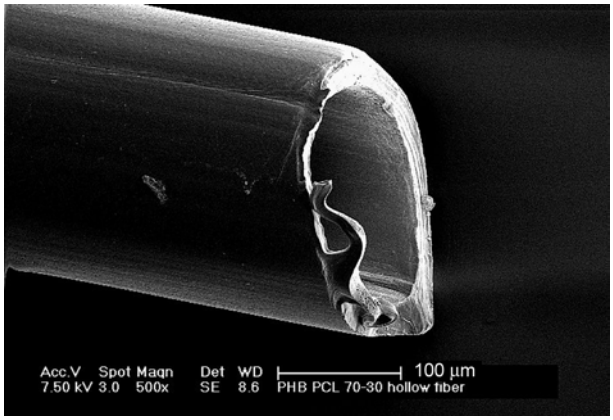

Figure 6. SEM image of hollow melt spun fiber from PHB/PCL 70/30

Through variation of the up-take speed and by dosage of the air pressure the diameter and the wall thickness of the hollow fibers was adjusted. The maximal diameter and wall thickness were limited by the geometry of the nozzle. By increasing the up-take speed of the bobbin (at constant mass throughput) a higher draw down ratio was set. The result was a reduced fiber diameter and a decreased wall thickness. The inner diameters of the fabricated tubes were in a range from 50 up to 600 µm.

3.4. Morphology

Figure 7 shows cryo-fractured cross sections of specimens of PHB/PCL 70/30 (G, P, F) that have been made by means of extrusion. The two phase system can be clearly seen for a) and b). Small homogenously dispersed droplets of PCL within the

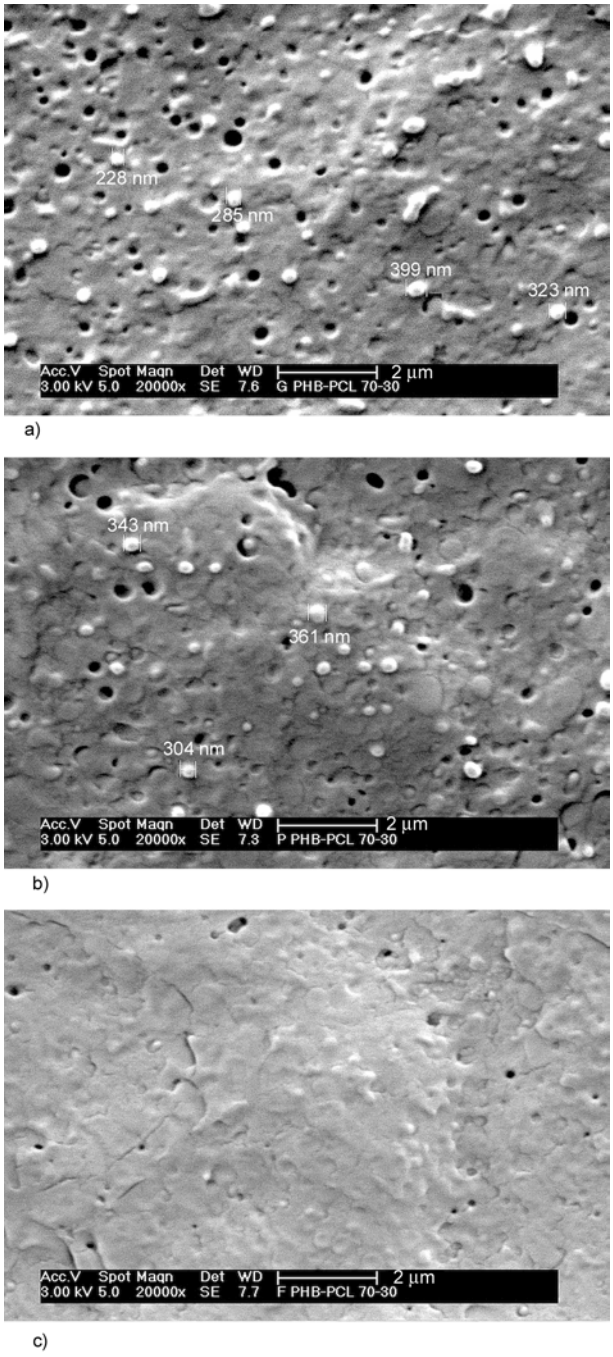

Figure 7. SEM images of extruded PHB/PCL 70/30 specimens: a) mixed granulates, b) powder mixture, c) precipitated material

PHB matrix are visible. Droplet size is in the range 200–400 nm. Some of them seem to be off place due to cryo-treatment in liquid nitrogen. PCL droplets might fall off at the surface of fracture since it is brittle at temperatures below –60°C (T_g). For the precipitated material such droplet structure is hardly visible. This procedure enables mixing on lowest possible molecular scale. Mixing in solution is therefore regarded to lead to the best available mixture for PHB/PCL 70/30 for spinning experiments.

4. Conclusions

Using a PHB/PCL 70/30 blend system dimensionally stable hollow biocompatible and biodegradable fibers have been produced by means of melt spinning. It was shown that a blend from precipitated material was well processable, whereas granulate material or powder mixtures were not spinnable due to phase separation phenomena. Contrary to other findings, tensile measurements showed evidence for significantly improved elastic properties for this immiscible blend in terms of bending stiffness. Brittle-fracture and catastrophical failure, as it is known for pure PHB, did not occur for the particular blend. Crazing deformation has been detected at the regions of maximum bending. However, the further application of the hollow fibers is not associated with maximum bending, high tension or compression stress. Thus, the achieved improvement of mechanical properties is satisfying.

For a composition of PHB/PCL 70/30 a microphase separation (fractionated crystallization) has been detected yielding into a fine homogenous dispersion of PCL droplets within in the matrix phase. However, the stated assumption that a fine dispersion of PCL droplets within the PHB matrix will lead to improved properties was not proven. A composition of 50/50, for which no droplet dispersion is visible, shows no significant difference in terms of *flexibility* compared to 70/30. Supposedly, the reason for better mechanical performance is a good interfacial adhesion between the different phases independent of their dispersion. A minimum of 30 wt% PCL is sufficient to adjust the mechanical properties towards the desired application in this case. The different contents of PCL may be useful to tailor the degradation rate. Providing adequate biological, physical and mechanical properties and a relevant biomolecular surface functionalization hollow fibers made from this specific blend are considered to be advanced structures for tissue engineering purposes, for instance as nerve guidance conduits. A certain porosity for permeation of nutrients and metabolites, one of the most important but challenging requirements for this particular application, has not been adjusted yet. The genera-

tion of a defined porous hollow fibers based on PHB will be subject of further investigations.

Acknowledgements

The authors would like to thank K. Scheibe, Dr. H. Scheibner and Dr. K. Schneider for carrying out the tensile measurements and the lively discussions.
Financial support from the Leibniz Institute for Polymer Research Dresden e.V. (*Departments: Mechanics and Structure, and Biofunctional Polymer Materials*) and the *German Research Foundation* (Ni 709/3-1) is gratefully acknowledged.

References

[1] Chen G-Q., Wu Q.: The application of polyhydroxyalkanoates as tissue engineering materials. Biomaterials, **26**, 6565–6578 (2005).
DOI: 10.1016/j.biomaterials.2005.04.036

[2] Freier T.: Biopolyesters in tissue engineering applications. Polymers for Regenerative Medicine, **203**, 1–61 (2006).
DOI: 10.1007/12_073

[3] Rentsch C., Rentsch B., Breier A., Hofmann A., Manthey S., Scharnweber D., Biewener A., Zwipp H.: Evaluation of the osteogenic potential and vascularization of 3D poly(3)hydroxybutyrate scaffolds subcutaneously implanted in nude rats. Journal of Biomedical Materials Research Part A, **92**, 185–195 (2010).
DOI: 10.1002/jbm.a.32314

[4] Schmack G., Jehnichen D., Vogel R., Tändler B.: Biodegradable fibers of poly(3-hydroxybutyrate) produced by high-speed melt spinning and spin drawing. Journal of Polymer Science Part B: Polymer Physics, **38**, 2841–2850 (2000).
DOI: 10.1002/1099-0488(20001101)38:21<2841::AID-POLB130>3.0.CO;2-#

[5] Vogel R., Tändler B., Häussler L., Jehnichen D., Brünig H.: Melt spinning of poly(3-hydroxybutyrate) fibers for tissue engineering using α-cyclodextrin/polymer inclusion complexes as the nucleation agent. Macromolecular Bioscience, **6**, 730–736 (2006).
DOI: 10.1002/mabi.200600116

[6] Kil'deeva N. R., Vikhoreva G. A., Gal'braikh L. S., Mironov A. V., Bonartseva G. A., Perminov P. A., Romashova A. N.: Preparation of biodegradable porous films for use as wound coverings. Applied Biochemistry and Microbiology, **42**, 631–635 (2006).
DOI: 10.1134/S0003683806060160

[7] Hinüber C., Häussler L., Vogel R., Brünig H., Werner C.: Hollow poly(3-hydroxybutyrate) fibers produced by melt spinning. Macromolecular Materials and Engineering, **295**, 585–594 (2010).
DOI: 10.1002/mame.201000023

[8] Battiston B., Geuna S., Ferrero M., Tos P.: Nerve repair by means of tubulization: Literature review and personal clinical experience comparing biological and synthetic conduits for sensory nerve repair. Microsurgery, **25**, 258–267 (2005).
DOI: 10.1002/micr.20127

[9] Ruiter G. C. W., Malessy M. J. A., Yaszemski M. J., Windebank A. J., Spinner R. J.: Designing ideal conduits for peripheral nerve repair. Neurosurgical Focus, **26**, E5/1–E5/9 (2009).
DOI: 10.3171/FOC.2009.26.2.E5

[10] Yao L., de Ruiter G. C. W., Wang H. A., Knight A. M., Spinner R. J., Yaszemski M. J., Windebank A. J., Pandit A.: Controlling dispersion of axonal regeneration using a multichannel collagen nerve conduit. Biomaterials, **31**, 5789–5797 (2010).
DOI: 10.1016/j.biomaterials.2010.03.081

[11] Novikova L. N., Pettersson J., Brohlin M., Wiberg M., Novikov L. N.: Biodegradable poly-β-hydroxybutyrate scaffold seeded with Schwann cells to promote spinal cord repair. Biomaterials, **29**, 1198–1206 (2008).
DOI: 10.1016/j.biomaterials.2007.11.033

[12] Terenghi G.: Peripheral nerve regeneration and neurotrophic factors. Journal of Anatomy, **194**, 1–14 (1999).
DOI: 10.1046/j.1469-7580.1999.19410001.x

[13] Jiang X., Lim S. H., Mao H-Q., Chew S. Y.: Current applications and future perspectives of artificial nerve conduits. Experimental Neurology, **223**, 86–101 (2010).
DOI: 10.1016/j.expneurol.2009.09.009

[14] Qian Z. Y., He Y., Zou Y. B., Li S., Liu X. B.: Structure and property study of degradable polyesteramide fibres: Processing and alkaline degradation behaviour. Polymer Degradation and Stability, **83**, 127–132 (2004).
DOI: 10.1016/S0141-3910(03)00233-7

[15] Belkas J. S., Munro C. A., Shoichet M. S., Johnston M., Midha R.: Long-term in vivo biomechanical properties and biocompatibility of poly(2-hydroxyethyl methacrylate-co-methyl methacrylate) nerve conduits. Biomaterials, **26**, 1741–1749 (2005).
DOI: 10.1016/j.biomaterials.2004.05.031

[16] Hazari A., Johansson-Rudén G., Junemo-Bostrom K., Ljungberg C., Terenghi G., Green C., Wiberg M.: A new resorbable wrap-around implant as an alternative nerve repair technique. The Journal of Hand Surgery, European Volume, **24**, 291–295 (1999).
DOI: 10.1054/JHSB.1998.0001

[17] Mohanna P-N., Young R. C., Wiberg M., Terenghi G.: A composite poly-hydroxybutyrate–glial growth factor conduit for long nerve gap repairs. Journal of Anatomy, **203**, 553–565 (2003).
DOI: 10.1046/j.1469-7580.2003.00243.x

[18] Avella M., Martuscelli E., Raimo M.: Review properties of blends and composites based on poly(3-hydroxy) butyrate (PHB) and poly(3-hydroxybutyrate-hydroxyvalerate) (PHBV) copolymers. Journal of Materials Science, **35**, 523–545 (2000).
DOI: 10.1023/A:1004740522751

[19] Lovera D., Márquez L., Balsamo V., Taddei A., Castelli C., Müller A. J.: Crystallization, morphology, and enzymatic degradation of polyhydroxybutyrate/polycaprolactone (PHB/PCL) blends. Macromolecular Chemistry and Physics, **208**, 924–937 (2007). DOI: 10.1002/macp.200700011

[20] Jenkins M. J., Cao Y., Howell L., Leeke G. A.: Miscibility in blends of poly(3-hydroxybutyrate-*co*-3-hydroxyvalerate) and poly(ε-caprolactone) induced by melt blending in the presence of supercritical CO_2. Polymer, **48**, 6304–6310 (2007). DOI: 10.1016/j.polymer.2007.08.033

[21] Qiu Z. B., Fujinami S., Komura M., Nakajima K., Ikehara T., Nishi T.: Structure and properties of biodegradable polymer-based blends. Macromolecular Symposia, **216**, 255–263 (2004). DOI: 10.1002/masy.200451224

[22] Chee M. J. K., Ismail J., Kummerlöwe C., Kammer H. W.: Study on miscibility of PEO and PCL in blends with PHB by solution viscometry. Polymer, **43**, 1235–1239 (2002). DOI: 10.1016/S0032-3861(01)00725-X

[23] Gassner F., Owen A. J.: Physical properties of poly(β-hydroxybutyrate)-poly(ε-caprolactone) blends. Polymer, **35**, 2233–2236 (1994). DOI: 10.1016/0032-3861(94)90258-5

[24] Beyreuther R., Brünig H.: Dynamics of fibre formation and processing. Springer, Berlin (2006).

[25] Ziabicki A.: Fundamentals of fiber formation: The science of fibre spinning and drawing. Wiley, New York (1976).

eXPRESS Polymer Letters Vol.5, No.7 (2011) 653–660
Available online at www.expresspolymlett.com
DOI: 10.3144/expresspolymlett.2011.63

Development and characterization of epoxy syntactic foam filled with epoxy hollow spheres

S. S. Samsudin, Z. M. Ariff, Z. Zakaria, A. A. Bakar*

School of Materials and Mineral Resources Engineering, Engineering Campus, Universiti Sains Malaysia, 14300 Nibong Tebal, Pulau Pinang, Malaysia

Received 10 August 2010; accepted in revised form 24 January 2011

Abstract. The present study focuses on the development and characterization of epoxy syntactic foam filled with epoxy hollow spheres (ESF/EHoS). The epoxy syntactic foam (ESF) was produced by embedding epoxy hollow spheres (EHoS) into a mixture of epoxy-hardener and 3% KOH solution. An innovative approach and simple procedure was implemented in the preparation of the EHoS where expanded polystyrene (EPS) beads were used as initiation material. The EPS beads were coated with the epoxy resin and these coated EPS beads were later cured and post-cured at high temperature which will also shrink the EPS beads thus producing a hollow structure. The physical and compressive properties of the developed ESF were characterized. The progressive collapse of the syntactic foam was monitored in real-time with respect to percentage of strain during a compression test. Results also indicated that the (ESF/EHoS) showed similar deformation pattern with other types of syntactic foams which exhibited the common three regions of deformations.

Keywords: *mechanical properties, epoxy hollow spheres, syntactic foam, compressive stress*

1. Introduction

Low density materials with capabilities of withstanding relatively high compressive stresses and deformation as well as damage tolerance have been an attractive research study for several decades. These materials are often used as core materials in sandwich composites for aerospace, automotive, civil as well as marine structural applications [1]. Open-cell foams are normally used for these kinds of properties but these cellular materials always have limitations in their applications because of their low compressive strength and modulus in sandwich structures [2, 3]. In order to overcome that problem, a class of closed cell foams known as syntactic foams were introduced by dispersing rigid hollow particles in a matrix material. These foams have been widely used in structural applications [4–7] since the late 1960's and early 1970's [8]. Syntactic foams can be classified as closed pore foams, since the porosity in these materials exists in the form of discrete hollow particles. The closed pore structure gives advantages of excellent mechanical properties, higher strength, low density as well as lower moisture absorption compared to the open cell foams [9]. Moreover, the usage of syntactic foams as core material in sandwich structure applications ensures high rigidity and compressive strength of the sandwich structures compared to utilization of other polymeric foams [10]. Several studies on mechanical properties of syntactic foams [7, 11–12] and their sandwich structures can be found in numerous published literature [9, 13–14].

Syntactic foams can be defined as composite materials in which hollow microspheres, or other small hollow particles, are randomly dispersed in a matrix [15]. Basically, there are two types of syntactic

*Corresponding author, e-mail: zulariff@eng.usm.my

foams: two-phase syntactic foams and three-phase syntactic foams. A two-phase syntactic foam consists of hollow spheres dispersed in a matrix resin [16] either in loose or close-packed structures [17] whereas a three-phase syntactic foam consists of hollow spheres dispersed in a matrix resin containing gaseous voids [18]. Usually, conventional syntactic foams were in two-phase systems. This type of syntactic foam actually has higher density and superior mechanical properties compared to the conventional blown foams, particularly in compression. The lowest practical densities for two-phase syntactic foams containing glass microspheres are limited and lie in the range of 500–600 kg/m^3 [16]. Nevertheless, densities below this value can be achieved only by intentional introduction of air bubbles into the resin thus forming the three-phase foams [16].

Microspheres can be considered versatile fillers compared to other any fillers because these materials can provide a variety of product enhancements and process improvements including low density, improved dimensional stability, increased impact strength, smoother surface finish, greater thermal insulation, easier machinability, faster cycle times, as well as cost savings [19]. Most microspheres are made from rigid shell materials such as polymeric materials (i.e. thermoplastic or thermoset resin) [20], ceramic, carbon, metal and glass [21] to obtain excellent end properties. In some cases, specialized surface treatments such as coatings on the surface of the microspheres will incorporate properties beyond those inherent to the microspheres' materials and construction, allowing the microspheres to be used for specific applications. Coating the microsphere adds new levels of functionality, such as dielectric, magnetic, fluorescent, conductive, thermal imaging properties or simply to improve bonding between the microspheres and the matrix. For example, coatings such as titanium dioxide (TiO_2) or silver can provide signature management capability where it will control the way in which objects are viewed when imaged using technologies such as radar or infrared imaging [19].

On the other hand, the matrix material binds the microspheres and gives the composite component its shape and determines the quality of its surface finish. Suitable materials can be selected for the matrix materials such as polymers, ceramics or metals [9]. Polymer matrices are commonly used for composites in commercial and high performance aerospace applications. The most widely used polymers are thermoset resins such as epoxy resin. Studies that utilize epoxy resin as the matrix can be found in several works [22–23] and these studies put more focuses on the use of glass hollow microspheres as the dispersed phase [22]. Besides that, most published studies also used and investigated various processing techniques in the production of syntactic foams [24–30]. Some of the literatures described the technique in detail [31, 32] and some patented their manufacturing techniques such done by Kim [33] and Meteer and Philipps [34]. Usually, syntactic foams where made by casting [24], pressure infiltration or by a blending method [26].

Generally, syntactic foams possess very good specific properties, especially compressive characteristics, due to the tailorability of their microstructures. Hence, it is important to understand the failure characteristic of syntactic foams during compressive deformation. In this study, epoxy resins were used as the binder while innovative epoxy hollow spheres (EHoS) were developed and used as reinforcing fillers. These materials were combined together using a simple casting technique. The developed EHoS were produced in-house, thus it would provide different approach in the production of syntactic foam compared to previously studied syntactic foams which usually utilized hollow spheres manufactured by established industries [23, 35–37]. Because the matrix and hollow sphere were made from the same materials, the high possibility of achieving good compatibility in the system is an added advantage. Furthermore, the (ESF/EHoS) system is projected to be able to provide new ideas in the development of syntactic foams production.

2. Experimental

2.1. Materials

D.E.R. 331, a clear liquid epoxy resin, manufactured by DOW Chemical Company (Michigan, U.S.A) was selected for the study. This is a diglycidyl ether of Bisphenol A (DGEBA) based resin with this following characteristics: Epoxide equivalent weight (g/eq) value of 182–192, viscosity in the range of 11 000–14 000 mPa·s and density of 1.16 g/ml at 25°C. D.E.R 331 was chosen as the polymer matrix for the syntactic foam due to wide

variety of curing agents available to cure the liquid epoxy resin at ambient conditions.

The above mentioned epoxy pre-polymer is an epoxy resin system which is supplied in liquid state and can be hardened by a curing agent when they are mixed in stoichiometric ratio. Clear epoxy hardener 8161 [isophorone diamine (IPD)] was chosen as the curing agent for this study and this chemical was supplied by ZARM Scientific and Supplies Sdn. Bhd (Malaysia). The characteristics of this curing agent are: Amine value of 260–284 mg (KOH)/gm, viscosity in the range of 300–600 mPa·s and specific gravity of 1.03 g/ml at 25°C. When used with D.E.R 331 resin, the curing agent would provide a reasonably good curing process within 2 to 7 days at ambient temperature.

It is difficult to mix large volumes of hollow spheres in the resin if the viscosity is high. Hence, a diluent was added to reduce the viscosity of the resin mix. To obtain this, Potassium Hydroxide (KOH) aqueous solution with a concentration 3% (w/w), was added to the mix to bring down the viscosity of the resin. Besides being the diluent for the system, the KOH solution also functions as an emulsifier that could be utilized to stabilize another foaming activity (i.e. physical frothing) which was initiated by extensive mixing during the preparation of the resin mix. The KOH solution was added to the mix in order to stabilize the cellular structure produced by the physical frothing. The KOH used for this study was obtained from BDH laboratories with lot number 217 C179854 and production code number 29628 5Q.

2.2. Preparation of epoxy hollow spheres

A resin mixture comprising of clear epoxy resin (D.E.R 331) and polyamine hardener (clear epoxy hardener 8161) with 2:1 ratio was formulated and mixed by using an in-house fabricated intensive mixer to produce the epoxy system. The EPS beads were later added into the prepared epoxy system in apportioned quantities and were ensured to be fully coated by the epoxy system. These beads were supplied by San Yong Enterprise Sdn. Bhd. with different range of sizes (3–6.5 mm) and will be used as intermediate materials to develop the EHoS. After that, the epoxy-coated EPS were transferred onto a tray filled with sufficient amount of $CaCO_3$ powder. This step is to ensure that the stickiness problem of the uncured epoxy-coated beads was addressed thus preventing the beads from clumping to each other. These coated EPS beads were then cured in an oven for 15 minutes at 80°C and post-cured at 120°C for 90 minutes to shrink all the EPS beads inside the epoxy-coated spheres with the intention to produce hollow structures within the spheres. The resultant cured EHoS were then sprayed with compressed air to remove excess $CaCO_3$ powder on their surface.

2.3. Preparation of epoxy syntactic foam

In order to produce the epoxy syntactic foams (ESF), initial preparation of the experimental setup needs to be readily available. The preparation step involves determining the amount of EHoS needed in the next experimental procedure (depending on the size of the spheres) by completely filling a polypropylene mould. This pre-determined amount of EHoS was then removed from the mould and properly put aside. All these initial preparation procedures are essential in ensuring that the mould will be completely filled and because the amount of EHoS was obtained in such a way that would restrict the spheres from floating to the surface during the foam production.

After the preparation steps have been implemented, the mixture for the matrix was prepared by mixing the epoxy resin and the hardener continuously together with the 3% KOH solution for about 15 minutes. The amount of KOH solution was fixed at 40% by weight with respect to the resin mix. The prepared cured EHoS were then added at regular intervals into the mixture subsequently after the matrix system preparation process has been completed within the duration of 15 minutes. Using such procedure, the uncured matrix compound consisting of EHoS dispersed in the epoxy matrix was achieved. The mixture was then poured evenly into the mould and after the mixture has been transferred into the mould successfully, a constant load with standard weight (1.2 kg) was placed on top of the mould lid to maintain the EHoS in their well-dispersed state. The summary of the initial preparation step and the production of a well dispersed sphere within the mould are illustrated in Figure 1.

The mixture was left at room temperature to complete the curing process for 24 hours. The cured composites were then demoulded and cut according to standard dimensions for respective testing after

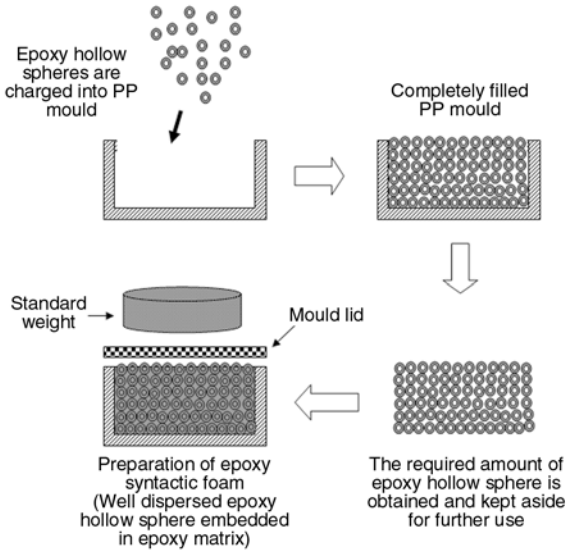

Figure 1. The summary of the initial preparation step and the production of a well dispersed sphere within the mould

Table 1. Composition of ESF/EHoS

Composition
Epoxy Resin
Hardener Polyamine
3% KOH Aqueous Solution
EHoS

seven days. Cutting process was done after seven days of the composites were produced due to the typical cure schedule (given by supplier) for epoxy resin with polyamine curing agent is around 2 to 7 days at room temperature. The composition of the ESF/EHoS is shown in Table 1.

2.4. Characterisation

In this study, the density measurement was made by measuring the mass and volume of regular parallelepiped specimens after removal of surface skin in accordance with standard procedure ASTM D3574. The specimens were cut into approximate dimension 50×50×25 mm from a uniform area free of irregularities. A Mitutoyo digital vernier caliper (Mitutoyo, Tokyo, Japan) was used to measure the dimension to an accuracy of 0.01 mm. All the specimens were ensured to be undistorted and conditioned in ambient room condition for 24 hours prior to mass and volume determination. The specimens were weighed on a Precisa digital analytical balance (Precisa Gravimetrics AG, Dietikon,Switzerland), model XT 220A to an accuracy of 0.0001 g. An average value determined from 5 samples was used as the density of the prepared foam. A digital image of the syntactic foam morphology was captured using a flatbed scanner. The sample image were then captured as to qualitatively assess and then further analyzed using Image J software to determine the spheres' cell sizes and their distribution within the matrix. In this method, the cells were selected randomly from the digital image and the image was then manually edited to highlight all cells boundaries at a set detection level of dark shades. Once this optimization is completed, thirty cells were counted from the selected regions of the observed digital images. This counting procedure was performed manually and the software was utilized to further conduct the statistical analysis such as determination of average cell size and cell distribution. Besides these measurements, the wall thickness of the produced EHoS was also assessed using similar image analysis facilities (see Figure 2). The amount of $CaCO_3$ embedded in the sphere wall was measured by placing a substantial amount of the EHoS in a furnace set at 600°C for 1 hour. This procedure burnt off the epoxy wall, and the remaining unburned portion was taken as the amount of $CaCO_3$ present in the sphere. The result indicated that the EHoS wall contained approximately 19% $CaCO_3$.

Compression test were carried out using a TestResources universal testing machine model Bi-00-71 (Shakopee, MN, USA). The samples were prepared in accordance with ASTM D3575, and at least four samples were tested. A crosshead speed of 6 mm/min was used to gradually monitor and record real-time changes that occurred during the compression test.

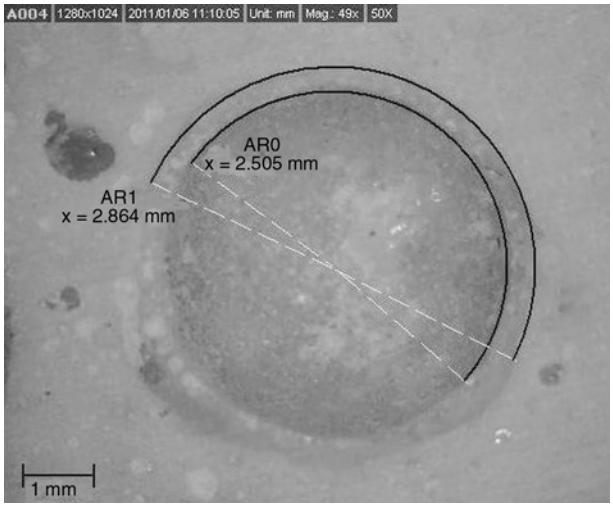

Figure 2. Digital image of a single EHoS showing its wall thickness

3. Results and discussion

Figure 3a shows a typical microstructure of the ESF/EHoS prepared in this study. Two types of porosity appeared in this material, which were contributed by the hollow spheres and matrix as shown in Figure 3b at high magnification. The hollow sphere porosity can be controlled by selecting the type and the size of hollow sphere. However, the matrix porosity could be attributed to air entrapment, which resulted in the formation of voids within the matrix during the mixing and coating procedure, as shown in Figure 2. Although an increase in porosity would undermine the mechanical properties the foam system, it can also be considered an advantage in that it can be manipulated to adjust the overall density and properties of the system. Table 2 shows several characteristics and properties of the produced ESF/EHoS.

The average density of the syntactic foam system was 566 kg/m^3 and this density was lower than the experimental result for control epoxy matrix without EHoS (1050 kg/m^3) and commercial epoxy matrix without EHoS (1160 kg/m^3) [3, 36]. This lower density was due to the utilization of the EHoS, which can effectively reduce the density of the materials and also provide a way of reducing the production cost which was attributed to the low price of the EPS bead templates compare to the other types hollow spheres available in the market. The cell sizes and their distribution are illustrated in Figure 4 where 30 readings were taken to ensure a good representation of the overall cell morphology. It can be seen that the cell sizes of the EHoS was quite close to one another and that cell wall thicknesses for the EHoS were nearly the same which is around 0.40 mm.

Table 2. Properties of the ESF/EHoS

	Properties
Compressive strength [MPa]	19.756
Modulus [MPa]	187.0±0.7
Cell size [mm]	Size range ~3–6
Density [kg/m^3]	566±9

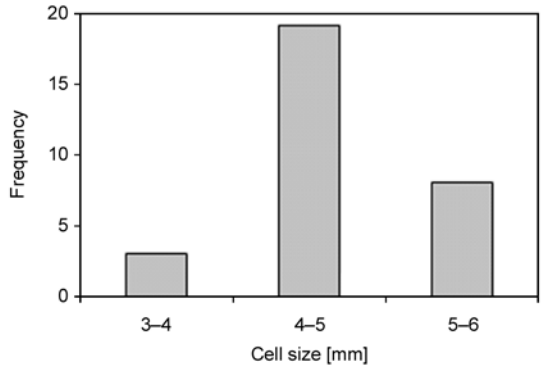

Figure 4. Distribution of EHoS size in the produced syntactic foam

The evidence of progressive collapse and the stress-strain curve for the ESF/EHoS are shown in Figure 5. The images in Figure 6a–d were taken from one sample with the lowest strength from the four samples that were subjected to compression test, in which complete crushing and collapse of the EHoS can be seen all over the side surface of the test specimen. The compressive behavior displayed by the syntactic foam was comparable to other syntactic foam systems, which utilized other thermoset matrix and glass microspheres as their constituents [2]. The initial drop in stress at 10% compressive strain can be related to the occurrence of crack initi-

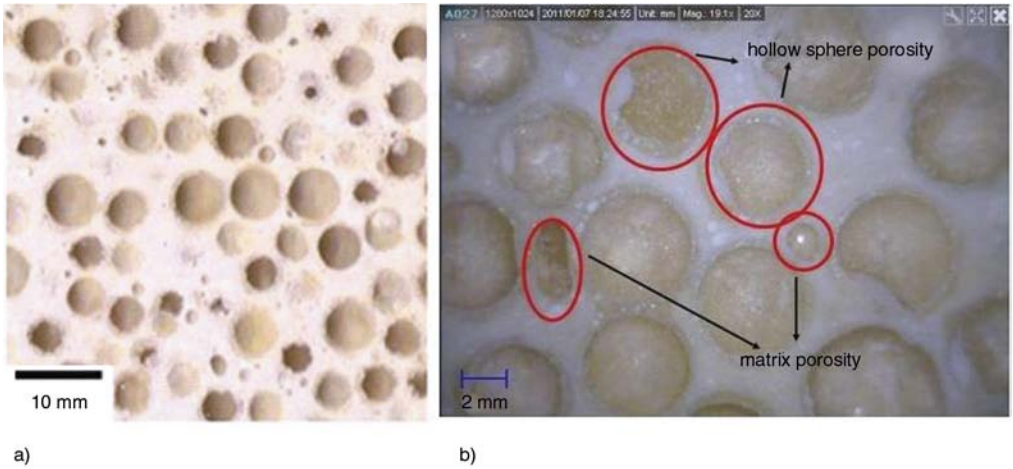

Figure 3. (a) Low magnification image of the ESF/EHoS (b) High magnification image of the ESF/EHoS showing hollow spheres porosity and matrix porosity

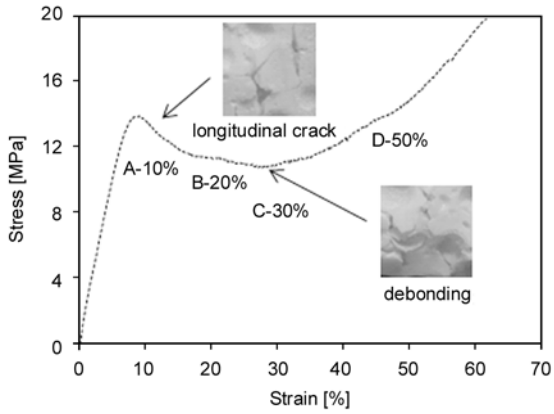

Figure 5. Representative compressive stress-strain curve for the ESF/EHoS

ation in the matrix as can be seen from the progressive cell collapse image included in Figure 6 [35]. At this stage, compression of the material resulted in a filling up of the matrix porosity due to the rupture of the porous feature. Further compression caused the formation of a shear crack in the longitudinal direction (i.e. the direction of compression) [3]. The slope then leveled in the region of 20% strain (b). During this stage, the longitudinal crack grew and the crushing of the EHoS was initiated. At this stage, further compression of the material resulted in more filling up of the matrix porosity due to the rupture of the porous feature. The extent of plateau region continued up till 30% strain (c) and the fracture mechanism in this region involved crushing of the EHoS, and similar observations were also reported by Kim and Plubrai [29].

Besides sphere crushing, the failure of EHoS can also be attributed to debonding (i.e. interfacial fracture between the matrix and EHoS) at the surfaces of the EHoS. However, the presence of voids in the EHoS limits the occurrence of debonding and promoted a higher failure mechanism through the rupture of the sphere wall because such fracture is faster than debonding. When a significant portion of the EHoS had been crushed, further loading caused densification of the foam [38], which was observed exceeding 35% strain as depicted in Figure 6. Above 50% (D) strain, the syntactic foam system failed completely.

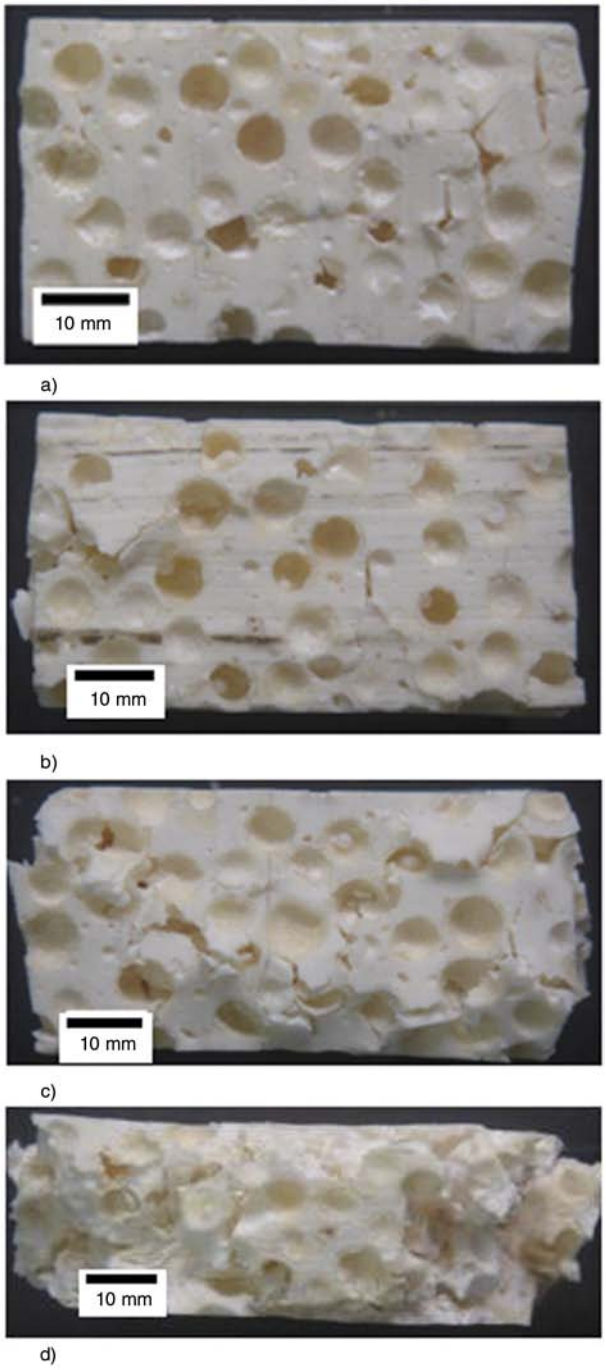

Figure 6. Deformation development of ESF/EHoS at (a) 10%; (b) 20%; (c) 30%; (d) 50% of compression

4. Conclusions

The development of EFS/EHoS syntactic foams and their compressive properties were investigated in the present study. The most crucial advantages of this syntactic foam are due to its simple production method and low cost production strategy because it does not utilize any expensive specialized equipment during its processing procedure which can be implemented at room temperature. The prepared EHoS showed great potential in replacing glass microspheres, which have been extensively used in many previous works. We found that the produced

syntactic foam had relatively high compressive modulus and compressive strength, and thus has the potential to be used in various engineering applications. Moreover, further studies regarding the wall thickness differences could be considered in the future to enhance utilization of these epoxy hollow spheres in their desired applications.

Acknowledgements

The authors would like to acknowledge the financial support from the Malaysian Ministry of Higher Education through the Fundamental Research Grant Scheme (Grant reference no. 203/PBAHAN/6071172).

References

[1] Tagliavia G., Porfiri M., Gupta N.: Vinyl ester–glass hollow particle composites: Dynamic mechanical properties at high inclusion volume fraction. Journal of Composite Materials, **43**, 561–582 (2009). DOI: 10.1177/0021998308097683

[2] Gupta N., Ye R., Porfiri M.: Comparison of tensile and compressive characteristics of vinyl ester/glass microballoon syntactic foams. Composites Part B: Engineering, **41**, 236–245 (2009). DOI: 10.1016/j.compositesb.2009.07.004

[3] Gupta N., Ye R., Porfiri M.: Characterization of vinyl ester-glass microballon syntactic foams for marine applications. in: 'Proceeding of 22nd Annual Technical Conference of American Society for Composites. Seattle, USA' paper 072 (2008).

[4] Sauvant-Moynot V., Gimenez N., Sautereau H.: Hydrolytic ageing of syntactic foams for thermal insulation in deep water: Degradation mechanisms and water uptake model. Journal of Materials Science, **41**, 4047–4054 (2006). DOI: 10.1007/s10853-006-7618-0

[5] Gupta N., Woldesenbet E.: Hygrothermal studies on syntactic foams and compressive strength determination. Composite Structures, **61**, 311–320 (2003). DOI: 10.1016/S0263-8223(03)00060-6

[6] Gupta N., Priya S., Islam R., Ricci W.: Characterization of mechanical and electrical properties of epoxy-glass microballoon syntactic composites. Ferroelectrics, **345**, 1–12 (2006). DOI: 10.1080/00150190601018002

[7] Woldesenbet E., Peter S.: Volume fraction effect on high strain rate properties of syntactic foam composites. Journal of Materials Science, **10**, 3065–3074 (2007). DOI: 10.1007/s10853-008-3065-4

[8] Malloy R. A., Hudson J. A.: Handbooks of composites reinforcement. VCH Publishers, New York (1993).

[9] Gupta N., Woldesenbet E.: Microballoon wall thickness effects on properties of syntactic foams. Journal of Cellular Plastics, **40**, 461–482 (2004). DOI: 10.1177/0021955X04048421

[10] Gupta N., Woldesenbet E., Kishore: Compressive fracture features of syntactic foams-Microscopic examination. Journal of Materials Science, **37**, 3199-3209 (2002). DOI: 10.1023/A:1016166529841

[11] Gladysz G. M., Chawla K. K.: Syntactic and composite foams: Proceedings of an engineering conferences international (ECI) conference. Journal of Materials Science, **41**, 3959–3960 (2006). DOI: 10.1007/s10853-006-7570-z

[12] Choqueuse D., Davies P.: Ageing of composites in underwater applications. in 'Ageing of composites' (eds.: Martin R.) Woodhead Publishing, Cambridge, 467–498 (2008).

[13] Devi K. A., John B., Nair R. C. P., Ninan K. N.: Syntactic foam composites of epoxy-allyl phenol-bismaleimide ternary blend – Processing and properties. Journal of Applied Polymer Science, **105**, 3715–3722 (2007). DOI: 10.1002/app.26316

[14] Banhart J.: Manufacture, characterisation and application of cellular metals and metal foams. Progress in Materials Science, **46**, 559–632 (2001). DOI: 10.1016/S0079-6425(00)00002-5

[15] Puterman M., Narkis M., Kenig S.: Syntactic foams I. Preparation, structure and properties. Journal of Cellular Plastics, **16**, 223–229 (1980). DOI: 10.1177/0021955X8001600403

[16] Narkis M., Puterman M., Kenig S.: Syntactic foams II. Preparation and characterization of three-phase systems. Journal of Cellular Plastics, **16**, 326–330 (1980). DOI: 10.1177/0021955X8001600603

[17] Narkis M., Gerchcovich M., Puterman M., Kenig S.: Syntactic foams III. Three-phase materials produced from resin coated microballoons. Journal of Cellular Plastics, **18**, 230–232 (1982). DOI: 10.1177/0021955X8201800402

[18] Landrock A. H.: Handbooks of plastics foams. Noyes Publications, New Jersey, (1976).

[19] Belle B. V.: Advances in high-temperature syntactic foam technology for offshore systems. in '2002 Offshore Technology Conference. Houston, USA' Paper 14120-MS (2002). DOI: 10.4043/14120-MS

[20] Capela C., Costa J. D., Ferreira J. A. M.: Test conditions effect on the fracture toughness of hollow glass micro-sphere filled composites. Strain, **44**, 141–146 (2008). DOI: 10.1111/j.1475-1305.2007.00357.x

[21] Wouterson E. M., Freddy Y., Boey C., Hu X., Wong S-C.: Specific properties and fracture toughness of syntactic foam: Effect of foam microstructures. Composites Science and Technology, **65**, 1840–1850 (2005). DOI: 10.1016/j.compscitech.2005.03.012

[22] Lin T. C., Gupta N., Talalayev A.: Thermoanalytical characterization of epoxy matrix-glass microballoon syntactic foams. Journal of Materials Science, **44**, 1520–1527 (2009). DOI: 10.1007/s10853-008-3074-3

[23] Yung K. C., Zhu B. L., Yue T. M., Xie C. S.: Preparation and properties of hollow glass microsphere-filled epoxy-matrix composites. Composites Science and Technology, **69**, 260–264 (2009). DOI: 10.1016/j.compscitech.2008.10.014

[24] Daoud A.: Synthesis and characterization of novel ZnAl22 syntactic foam composites via casting. Materials Science and Engineering A, **488**, 281–295 (2008). DOI: 10.1016/j.msea.2007.11.020

[25] Rohatgi P. K., Guo R. Q., Iksan H., Borchelt E. J., Asthana R.: Pressure infiltration technique for synthesis of aluminum–fly ash particulate composite. Materials Science and Engineering A, **244**, 22–30 (1998). DOI: 10.1016/S0921-5093(97)00822-8

[26] Orbulov I. N., Dobranszky J., Nemeth A.: Microstructural characterisation of syntactic foams. Journal of Materials Science, **44**, 4013–4019 (2009). DOI: 10.1007/s10853-009-3552-2

[27] Andersen O., Waag U., Schneider L., Stephani G., Kieback B.: Novel metallic hollow sphere structures. Advanced Engineering Materials, **2**, 192–195 (2000). DOI: 10.1002/(SICI)1527-2648(200004)2:4<192::AID-ADEM192>3.0.CO;2-#

[28] Verweij H., With G., Veeneman D.: Hollow glass microsphere composites: Preparation and properties. Journal of Materials Science, **20**, 1069–1078 (1985). DOI: 10.1007/BF00585751

[29] Kim H. S., Plubrai P.: Manufacturing and failure mechanisms of syntactic foam under compression. Composites Part A: Applied Science and Manufacturing, **35**, 1009–1015 (2004). DOI: 10.1016/j.compositesa.2004.03.013

[30] Nijenhuis K., Addink R., Vegt A. K.: A study on composites of nylon-6 with hollow glass microspheres. Polymer Bulletin, **21**, 467–474 (1989). DOI: 10.1007/BF00271969

[31] Ramachandara M., Radhakrishna K.: Synthesis-microstructure-mechanical properties-wear and corrosion behavior of an Al-Si (12%)- flyash metal matrix composite. Journal of Materials Science, **40**, 5989–5997 (2005). DOI: 10.1007/s10853-005-1303-6

[32] Ramachandra M., Radhakrishna K.: Effect of reinforcement of flyash on sliding wear, slurry erosive wear and corrosive behavior of aluminium matrix composite. Wear, **262**, 1450–1462 (2007). DOI: 10.1016/j.wear.2007.01.026

[33] Kim H. S.: Method for forming syntactic foams. U.S. Patent 2008/0233384 A1, USA (2008).

[34] Meteer C. L., Philipps T. E.: Syntactic foam core material for composite structures. U.S. Patent 5888642, USA (1999).

[35] Caeti R., Gupta N., Porfiri M.: Processing and compressive response of functionally graded composites. Materials Letters, **63**, 1964–1967 (2009). DOI: 10.1016/j.matlet.2009.06.024

[36] Gupta N., Nagorny R.: Tensile properties of glass microballoon-epoxy resin syntactic foams. Journal of Applied Polymer Science, **102**, 1254–1261 (2006). DOI: 10.1002/app.23548

[37] Karthikeyan C. S., Sankaran S., Kishore: Elastic behaviour of plain and fibre-reinforced syntactic foams under compression. Materials Letters, **58**, 995–999 (2004). DOI: 10.1016/j.matlet.2003.08.012

[38] Li P., Petrinic N., Siviour C. R., Froud R., Reed J. M.: Strain rate dependent compressive properties of glass microballoon epoxy syntactic foams. Materials Science and Engineering: A, **515**, 19–25 (2009). DOI: 10.1016/j.msea.2009.02.015